POLITECNICO DI TORINO

Master's Degree in Electronic Engineering

Master's Degree Thesis

Free-space chaos-based private communication with quantum cascade lasers emitting in the thermal atmospheric window

Supervisors

Prof. M. GIOANNINI

Prof. F. GRILLOT

Candidate

Sara ZAMINGA

October 2022

Acknowledgements

The past six months have been a great challenge for me, an experience I have longed for, to fill that feeling of incompleteness I felt inside. That is why I would like to thank first of all my professor Mariangela Gioannini, for serving me the springboard that now sees me stable in Paris. I thank her for the support given to me during these months, for the availability shown to me despite the distance, and to have always been ready to listen to my needs.
I would also like to thank Professor Frédéric Grillot, my current and future supervisor at Télécom Paris. Thank you for accepting my every request with patience, for the opportunity granted to me, but above all for having believed in me and my potential from the very beginning. Thank you for stimulating me, aware more than me of my strengths. It has been inspiring to work with you, and I look forward to starting the new doctoral journey together.
I would now like to thank Pierre, the best *senpai* one could look for. Thank you for passing on all your experience and knowledge to me. Thank you for being sensitive and accomodating with me and my stubbornness, for understanding my mood swings, and always encouraging me when I thought I couldn't make it. Thank you for never underestimating me, for making me feel a colleague and friend. We form a great team!
I would like to thank Olivier, for the advice time dedicated to our project, despite the non-negligible distance.
Thank you Hyunah, for the enthusiasm you show in every aspect of life, and for bringing joy simply with a smile.
Finally, I would like to thank all my colleagues, met in the corridor of Télécom, constituting a source of academic comparison and growth, but also an opportunity for detachment and laughter.

Siete soliti descrivermi come una persona di poche parole, ma genuinamente schietta e sincera; a volte un po' pungente. Per quanto sia complicato, oggi cerchero' di dare voce al lato sensibile, ma anche fragile, che tendo sempre a seppellire. Ma ovviamente lo faro' a modo mio, con quella nota di sarcasmo, che non mi abbandona mai. Con questo lavoro si conclude una stagione importante della sitcom che mi vede come protagonista; e tutti voi, che avete aspettato pazientemente il finale di stagione, sicuramente avrete contribuito a scrivere il copione e renderlo unico. Alcuni di voi sono stati con me i personaggi principali; altri, solo delle comparse. Chiaramente ci sarà un sequel, non vi allarmate; una serie cosi' di successo non puo' terminare con lacrime e commozione (ops, piccolo spoiler), ma con una fragorosa risata. Quindi sedetevi comodi; non mi resta che augurarvi buona "visione"!

Le scene iniziali di quest'ultima puntata non possono che essere dedicate ai miei supereroi, mia sorella e i miei genitori.
Simona, il mio sole, splendente punto fermo. Instancabile forza della natura, sei essenza e modello di vita. Sei cio' che mi completa, la parte migliore di me. Ancora gattonavo quando ho incominciato a seguire le tue orme. Mi hai preso per mano, e mi hai insegnato a camminare, poi a correre, saltare e ballare. Sono caduta tante volte, ma eri (e sei) sempre li' a rialzarmi e curare le mie cicatrici. Grazie per essere la fan numero uno dei miei traguardi.
Mamma, simbolo puro di amore, forza e presenza. Sei la colonna portante della nostra famiglia; moglie e madre devota, hai dedicato ogni istante della tua vita a noi e alla nostra felicità. Papà, sinonimo di bontà, fermezza e pazienza. Con la tua calma e i tuoi silenzi (che valgono più di mille parole), conferisci equilibrio alla nostra famiglia, mettendo ordine al nostro caos. Insieme, immagine di unità e indivisibilità, l'uno la roccia dell'altra. Avete reso ogni mio sogno realtà, anche se questo vi ha comportato non pochi sacrifici. Avete sempre cercato di rendere la mia vita migliore; avete investito tutto il vostro tempo e le vostre attenzioni per offrirmi cio' che di migliore avevate da darmi. Molto spesso da piccola sono stata ingrata e irriconoscente. Non sazia, ho varcato l'uscio di casa e mi sono messa alla ricerca di nuovi stimoli, credendo ingenuamente che il mondo avesse ancora il meglio da farmi scoprire. Ma essere lontana da casa mi ha permesso di maturare e apprezzare la quotidianità e la semplicità dei piccoli gesti. E con il senno di poi, posso ammettere senza alcun dubbio di aver avuto sin dai primi istanti della mia vita il meglio davanti ai miei occhi, perché il meglio siete voi. Grazie.
Il mio pensiero ora va a chi non c'è più, a chi mi guarda e mi protegge dall'alto, a chi mi porta ancora, speranzosa, a rivolgere il naso all'insù. La vostra perdita mi ha insegnato che la vita é imprevedibile, e che molto spesso abbiamo la presunzione di sottovalutare quanto di più prezioso questa ci regala: la saggezza e i consigli di una nonna, che ora tanto ricerco, ma che purtroppo non potro' avere più.

Il mio ringraziamento ora va a mio nonno Leonardo, instancabile tuttofare, dispensatore di interminabili lezioni di vita, icona di laboriosità e impegno.
Grazie a mio zio Tommaso, che non si è inginocchiato di fronte alle difficoltà della vita, ma al contrario si è saputo reinventare, mantenendo fede alla promessa del "per sempre". Grazie a mia zia Assunta, ai giri in bici l'estate, ai Tronky, al Settebello e alle partite a Scopa. Minuta e inarrestabile, ti ricordero' sempre cosi'. Grazie ai miei cugini Andrea e Antonio, protettivi verso la piccola di casa, sempre capaci con una parola di rallegrare i pranzi infiniti in famiglia.
Grazie alle mie zie Debora e Sabina, donne ambiziose, capaci di coniugare il desiderio di affermazione con l'impegno verso la propria famiglia. Mi avete sempre ricordato che essere donne assetate non è un difetto; al contrario, avete alimentato quella sete, consapevoli più di tutti che sarei potuta arrivare molto lontano. Grazie ai loro mariti, ai miei zii Luigi e Mauro, per aver saputo dare spazio ai sogni delle loro mogli, con affetto e sostegno. Grazie ai miei cugini Nicolle, Salvatore, Grace e Lorenzo, a tutti i giochi condivisi e ai discorsi senza senso sul divano di nonna. Siete la mia infanzia.
Grazie ai miei zii Immacolata e Antonio, custodi di saldi principi, esempio raro di generosità, integrità e premurosità. Mi avete insegnato che la distanza non è sempre sinonimo di assenza. Grazie a Sergio e Daniela, alla leggerezza e ai sorrisi che portate alla nostra famiglia, alla vicinanza che ci avete sempre dimostrato, ai caffè e al miele che addolcisce tutte le mie mattine.
Se mi ci è voluta letteralmente una giornata per ringraziare i miei familiari, dubito che una settimana basti per dedicare qualche riga a tutti voi, amici miei.
Indubbiamente le prime parole vanno ad Agnese, quella di sempre, presente in ogni fase della mia vita, certezza indiscussa e amica fedele. Io Bloom e tu Stella, sei protagonista di ogni ricordo che conservo gelosamente nel mio cuore. Sempre mano nella mano, compagne di banco, ma prima di tutto compagne di vita, insieme siamo maturate e diventate adulte. Fragile, ma tenace idealista, smussi i miei lati spigolosi e razionali; grazie per tenere viva la bambina che è in me, e ricordarmi che sognare è gratis. Grazie ai suoi genitori: grazie a Patrizia, ad aver lasciato sempre aperta la porta di casa per me, ad avermi sempre accolta con amore. Sei la mia seconda mamma. Grazie a Tonio, alle tue battute che tanto mi facevano ridere da bambina e ad averci insegnato che leggerezza non è sinonimo di superficialità. Grazie a nonna Assunta, al calore e all'attenzione che mi hai sempre dedicato.
Grazie a Matteo, alle ricreazioni insieme, alle canzoni inventate, agli scherzi di cui ero vittima, alla tua vivacità e alla tua irrequietezza. Silvia, immagine di eleganza, autenticità e femminilità, grazie per la protezione e il conforto che teneramente doni a mia sorella.

Grazie alla mia Torino, alle opportunità che mi hai donato, al mondo che ho incominciato a scoprire, e alle persone, più o meno passeggere, che ho avuto modo

di incontrare e conoscere. Grazie ad Annalisa, la mia fata Barantina, sempre pronta ad agitare la sua bacchetta magica per trovare soluzione ai miei problemi. Prima persona imbattuta nei corridoi del Collegio Einaudi, hai trasformato la mia ingenuità in consapevolezza e guidizio. Rifugio per le mie insicurezze e le mie paure, mi hai sempre donato serenità e tranquillità. Grazie per essere il mio porto sicuro, per aver reso felice mamma per avermi insegnato a mangiare le verdure, ma anche i negozi bio d'Italia, che mensilmente continuiamo a finanziare. Grazie a Cristiano, la sua metà solida e pacata. Grazie a Francesca, alla sua straordinaria risata, alla sua contagiosità ed esuberanza. Modello di gentilezza e cortesia, la tua positività ha illuminato i miei momenti più bui.
Grazie a Cocco, che con la sua spontaneità mi ha insegnato che la sincerità di un'amica è un tesoro raro. Grazie a Jacopo, per avermi fatto sentire sempre speciale, ma un po' meno per le partite a taboo e il posto rubato al gioco della sedia. Grazie ad entrambi perché rimanete tra i pochi veramente orgogliosi dei miei successi. Grazie a Chiara, per avermi mostrato come trasformare gli ostacoli in successi, e avermi fatto comprendere che le soddisfazioni più grandi sono accompagnate dai sacrifici più duri. Grazie a Carmen, per avermi spiegato che casa non è un posto, ma è una sensazione, per avermi rivelato la sua parte più fragile e avermi insegnato l'importanza dell'esprimere se stessi. Grazie ad Alfredo, a non essere rimasto mai in superficie, ad aver scavato nel mio profondo, ad avermi capita, mai giudicata, ad aver allontanato le mie paure, ad aver accolto soprattutto i lati peggiori di me. Grazie a Valeria, la mia erede del primo piano, per avermi ricordato da dove sono partita, per aver ridato colore a quelle mura sempre più sbiadite nei miei ultimi mesi in collegio. Grazie a Gioele, Enzo, Martina, Pierpi, Serena, Ari Vale, Ari Puli, Greg, Elisa, Marco e Vincenzo per la vostra forte personalità e per aver contribuito a rendere unico il primo piano con il vostro modo di essere. Grazie a tutti i ragazzi del collegio Einaudi, per tutti i brindisi, gli aperitivi, le feste, ma anche le sessioni affrontate uniti e forti.

Non è stato solo il collegio Einaudi ad avermi regalato una famiglia, ma anche il Poli mi ha permesso di scovare tante perle rare. Gaia, sin dal primo anno, compagna di disagi e di disavventure. Grazie per la tua semplicità e tenerezza, per essere una costante, per concedermi sempre la priorità, per assecondare ogni mia pazzia, per pronunciare sempre la parola giusta al momento giusto, e per rendere ancora Torino una calda dimora. Grazie ad Ale, la mia versione bionda, alta e ligure. Inseparabili sin dal primo istante, abbiamo superato insieme ogni intoppo incontrato nel nostro cammino. Mi hai dato forza nei momenti di debolezza, luce quando la vista era offuscata, un'ancora quando pensavo di annegare. Collega e complice, non avrei desiderato altro che poter celebrare questa vittoria insieme, perché in fondo nel successo dell'una c'è anche un po' dell'altra. Grazie a Fede, perché sei solare, infondi il buonumore e mi hai insegnato come le piccole cose a

volte siano le più speciali. Grazie per avermi reso parte del tuo mondo, segreto a molti, e per avermi compreso, anche e soprattutto nel silenzio. Grazie ad Elisea, uragano vigoroso che rende sempre uniche le nostre serate. Grazie ad AleSanna, perché nonostante la distanza è sempre stato un amico presente, con poche parole, ma gesti eloquenti. Grazie a Carlo, fondatore e pilastro del nostro gruppo di ingegneri nerd; grazie per la tua loquacità ed energia, per la cioccolata, le feste in casa, i pranzi-confessionali e le attenzioni che sempre mi riservavi. Grazie ad Ema, per avermi insegnato cosa sia davvero il coraggio, soprattutto nell'inseguire i propri sogni. Grazie a Matteo, Stefano, Paola, Pollo e Galla, per gli spritz alle Panche e per i momenti di spensieratezza. Grazie a Davide, miglior compagno di laboratorio, per i futuri pranzi a cui mi autoinviterò. Grazie a Pier e Francesco, colleghi eccezionali e amici pazienti, mai esitanti a compiacere le richieste un po' stravaganti di due persone ancora più eccentriche. Grazie a Michelangelo, ad esserti rivelato un amico attento, presente e premuroso. Grazie per il sostegno che mi hai dimostrato in questi mesi, per i discorsi motivazionali, per le conversazioni trash ma mentalmente impegnate, per quella sobria saggezza che ti porta a dire la cosa giusta nel momento opportuno.

Infine, grazie alla mia nuova casa, a Parigi, che mi continua ad insegnare ogni giorno cosa significa essere diverso, sinonimo di unico e speciale. Grazie a Valentina, delicata e formidabile, mi hai mostrato cosa significa essere autentici in una società grigia e uniforme. Grazie a Matteo, per dimostrarmi ogni giorno la tua presenza, anche se lo fai con quel sarcasmo cinico, che ormai ho imparato ad apprezzare. Grazie a Cesco, dolce e disponibile, per la limpidezza che dimostri in ogni tua piccola azione. Grazie a Riccardo, per avermi fatto sentire sin da subito parte della nostra famiglia. Grazie a Fra e Laura, per le cene e le notti d'estate trascorse sempre insieme, tra un pettegolezzo ed un altro. Grazie a Lorenzo, Frank e FraFortino per avermi accolto a braccia aperte, e aver reso ogni giorno a Parigi Ecla-tante. Thanks to my international friends who taught me what inclusion, welcome, friendliness, acceptance and fairness really means. Thank you for never leaving me alone, for the evenings together after a long and tiring day at work, for always offering me insights and growth.

Grazie a chi non ho avuto modo di menzionare per ovvie ragioni, ma che mi ha aiutato a sistemare i tasselli di un puzzle ancora incompleto. Grazie non solo a chi mi ha incoraggiato, ma anche a chi, più o meno inconsapevolmente, ha colpito la parte più sensibile di me, dandomi delle potenti lezioni di vita, che mi hanno fatto diventare la donna consapevole e ostinata che sono ora.
Grazie a tutti i bivi che la vita mi ha posto davanti, alle scelte che ho preso e agli errori che ho commesso, perché hanno rappresentato un trampolino di lancio, ciò che mi porta a scrivere queste righe a duemila chilometri di distanza. Sono grata

ad ogni lacrima versata, all'impegno e alla dedizione che ho riposto, alla passione sempre ardente in me, alla curiosità che mi ha sempre spinto a cercare di più.
Concludo in maniera forse scontata ringraziando me stessa, la mia critica più severa, la mia più acerrima nemica. Sara, fermati un attimo, guarda indietro, e concediti un applauso, prima di calare il sipario.

Table of Contents

List of Tables

List of Figures

Acronyms

AWG Arbitrary Waveform Generator

BER Bit Error Rate

CC Coherence Collapse

CMOS Complementary Metal-Oxide-Semiconductor

DFB Distributed Feedback

DIRCM Directed Infrared Countermeasures

EM Electromagnetic

FEC Forward Error Correction

FFE Feed-Forward Equalization

FM Frequency Modulation

FWM Four-wave Mixing

FIR Far-Infrared

FP Fabry-Perot

FSO Free-space Optics

FTIR Fourier Transform Infrared Spectrometer

ICL Interband Cascade Laser

IR Infrared

ISI Intersymbol Interference

KSE Kolmogorov-Sinaï Entropy

KYD Kaplan-Yorke Dimension

LADAR Laser Detection And Ranging

LE Lyapunov Exponent

LEF Linewidth Enhancement Factor

LLE Largest Lyapunov Exponent

LFF Low Frequency Fluctuations

MOCVD Metalorganic Chemical Vapor Deposition

MBE Molecular Beam Epitaxy

MIR Mid-Infrared

ML Master Laser

NIR Near-Infrared

OFC Optical Fiber Communication

PAM Pulse Amplitude Modulation

PIC Photonic Integrated Circuit

PQC Post-Quantum Cryptography

QCL Quantum Cascade Laser

QKD Quantum-Key Distribution

QW Quantum Well

RADAR Radar Detection And Ranging

SEM Scanning Electron Microscope

SLs Semiconductor Lasers

SL Slave Laser

SNR Signal-to-noise Ratio

SONOI Silicon-on-Nitride-on-Insulator

TE Transverse Electric

TEM Transmission Electron Microscope

TM Transverse Magnetic

UV Ultraviolet

VIS Visible

WPE Wall-plug efficiency

"One must still have chaos in oneself to be able to give birth to a dancing star"
- Friedrich Nietzsche, *Thus Spoke Zarathustra*

"Bisogna avere il caos dentro di sè, per generare una stella danzante"
- Friedrich Nietzsche, *Così parlò Zarathustra*

Chapter 1

Introduction

1.1 The infrared window

1.1.1 The electromagnetic spectrum

The electromagnetic (EM) spectrum is the range of frequencies of all different forms of electromagnetic radiation in the universe. It is a type of energy that pervades the cosmos in the form of electric and magnetic waves, allowing for the transfer of energy and information.
The electromagnetic spectrum covers electromagnetic waves with frequencies ranging from below 1 Hz to above 10^{25} Hz, corresponding to wavelengths from thousands of kilometers down to a fraction of the size of an atomic nucleus.

Physical properties

Electromagnetic waves are typically described by three physical properties: the frequency f, the wavelength λ, and the photon energy E. Three equations describe how they are related one with the other:

$$f = \frac{c}{\lambda} \qquad f = \frac{E}{h} \qquad E = \frac{hc}{\lambda} \tag{1.1}$$

where:

- $c = 299792458\ \mathrm{m\,s^{-1}}$ is the speed of light in a vacuum
- $h = 6.63 \times 10^{-34}\ \mathrm{J\,s} = 4.14 \times 10^{-15}\ \mathrm{eV\,s}$ is Planck's constant

Regions

The types of EM radiation are broadly classified into bands:

1. Gamma radiation
2. X-ray radiation
3. Ultraviolet radiation
4. Visible light
5. Infrared radiation
6. Microwave radiation
7. Radio waves

This classification goes in the increasing order of wavelength, which is characteristic of the type of radiation.
EM radiation interacts with matter in different ways across the spectrum, since each type of EM radiation is created by particles being accelerated by an electric field and producing oscillating waves of electric and magnetic fields. The distance between the peaks of those waves is the wavelength of the radiation, while the number of waves is the frequency. Ultraviolet (UV), Visible (VIS) and Infrared (IR) radiations constitute together the optical radiation.

The infrared radiation

A particular attention is given to the infrared (IR) radiation, more specifically to the mid-infrared (MIR) region, exploiting light sources emitting at 9.33 µm in this work. The International Organization for Standardization (ISO) has proposed the division of optical radiation into spectral bands for optics and photonics, for the first time in 2007, through the 20473 standard [1]. It does not apply to lighting or telecommunication applications or to protection against hazards from optical radiation in occupational areas.
The spectral bands are specified by the given wavelength limits, as reported in Table 1.1, for the infrared domain only.

<table>
<tr><th>Designation</th><th colspan="2">Abbreviation</th><th>Wavelength [µm]</th><th>Frequency [THz]</th></tr>
<tr><td rowspan="2">Near-Infrared</td><td rowspan="2">NIR</td><td>IR-A</td><td>0.78-1.4</td><td>215-385</td></tr>
<tr><td>IR-B</td><td>1.4-3</td><td>100-215</td></tr>
<tr><td>Mid-Infrared</td><td colspan="2">MIR</td><td>3-50</td><td>6-100</td></tr>
<tr><td>Far-Infrared</td><td colspan="2">FIR</td><td>50-1000</td><td>0.3-6</td></tr>
</table>

Table 1.1: ISO 20473 standard

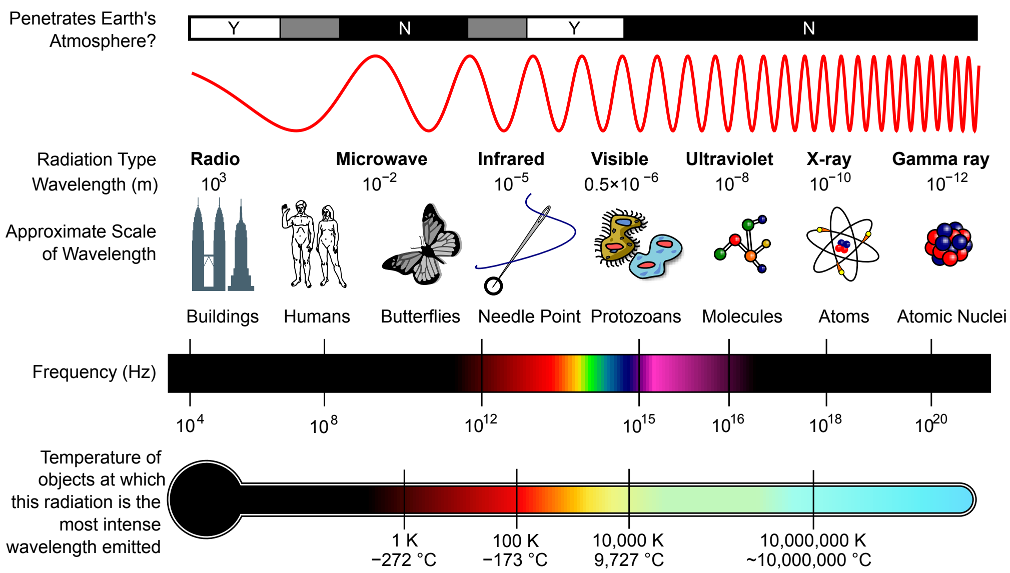

Figure 1.1: Diagram of the EM spectrum, showing: bands subdivision, wavelength, frequency, black body emission temperature. The first bar describes the penetration capability of each EM band to penetrate the earth's atmosphere. Y is for yes and N is for no. Although some radiations are marked as N for no in the diagram, some waves do in fact penetrate the atmosphere, although extremely minimally compared to the other radiations.

1.1.2 The atmospheric window

The atmospheric window is the range of wavelengths of the EM spectrum that can pass through the Earth's atmosphere. We can recognize three main atmospheric sub-windows:

- the optical window: it runs from around 300 nm (ultraviolet-B) up into the range the human eye can detect, roughly 400–700 nm and continues up to approximately 2 µm.
- the infrared window: it is roughly the region between 8 and 14 µm
- the radio window: its lower limit has a value of about 15 MHz ($\lambda \approx 20$ m), whereas the best upper limit achievable from optimal terrestrial observation sites is equal to approximately 1 THz ($\lambda \approx 0.3$ mm).

In this chapter, the focus is on the infrared window, being the main interest for this study.

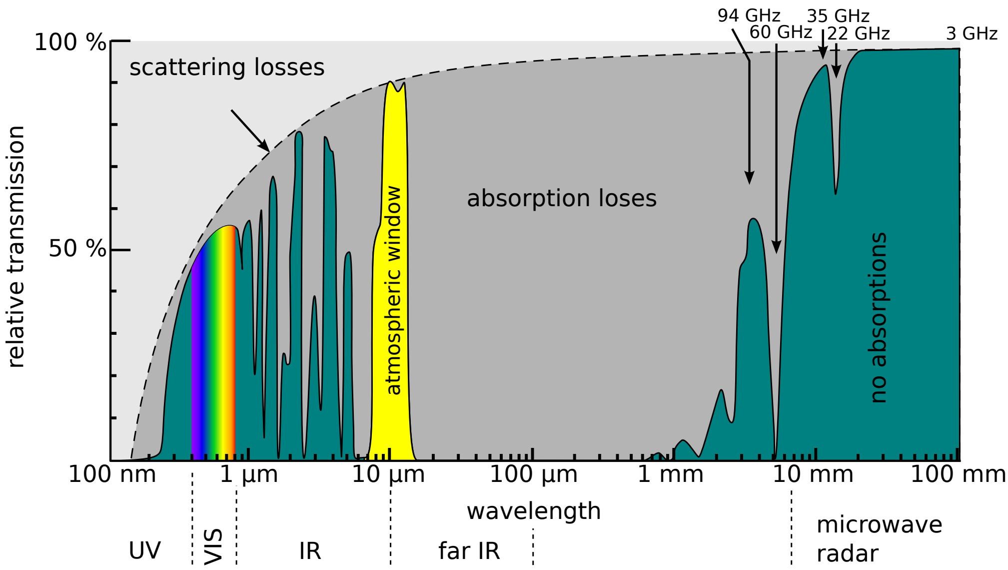

Figure 1.2: Absorption spectrum during atmospheric transition of electromagnetic radiation. An atmospheric transmission 'window' can be seen between 8-14 µm (700-1250 cm^{-1}).

1.1.3 The atmospheric channel

The atmosphere is principally classified into homosphere (0-90 km) and heterosphere (above 90 km).
The homosphere is composed of various gases, water vapors, pollutants and other chemicals. Maximum concentration of these particles are near the Earth surface in the troposhere that extends up to 20 km. Then, the density of the particles decreases with the altitude up through the ionosphere (90-600 km). The ionosphere contains ionized electrons due to solar radiations, forming a radiation belt around the Earth.
The atmospheric particles interact with all signals that propagate through the radiation belt and lead to the deterioration of the received signal due to absorption and scattering. Both absorption and scattering are wavelength-dependent, therefore the choice of wavelength has to be very wisely done, according to the application. In particular, it can be demonstrated that these detrimental effects are more pronounced when the operating wavelength is comparable with the cross-sectional dimensions of the atmospheric particles.
A theoretical model accounting for these atmospheric losses will be provided hereafter.

1.1.4 Atmospheric losses

The atmospheric condition in free-space optical (FSO) channel can be broadly classified into three categories:

1. clear weather: characterized by long visibility and relatively low attenuation.

2. cloudy weather: from mist or fog to heavy clouds conditions, it is characterized by low visibility, high humidity and large attenuation.

3. rainy weather: rain is characterized by the presence of droplets of variable sizes, and it can produce severe effects depending upon rainfall rate.

The different atmospheric constituents contribute to create the various types of losses encountered by the optical beam when propagating. A brief overview is here proposed.

Absorption losses

Absorption is the phenomenon where the signal energy is absorbed by the particles present in the atmosphere resulting in the loss of signal energy and gain of internal energy of the absorbing particle.
At VIS and IR wavelengths, the principal atmospheric absorbers are the molecules of water, carbon dioxide and ozone. The attenuation experienced by the optical signal when it passes through the atmosphere can be quantified in terms of optical depth τ, which correlates with power at the receiver P_R and the transmitted power P_T as

$$P_R = P_T \exp(-\tau)$$

The ratio of power received to the power transmitted in the optical link is the atmospheric transmittance: $T_a = P_R/P_T$. The loss in dB that the beam experiences during propagation through the atmosphere is calculated using the equation:

$$Loss_{prop} = -10 \log_{10} T_a$$

Scattering losses

In scattering, there is no loss of signal energy like in absorption, but the signal energy is redistributed in arbitrary directions, with or without wavelength change. It depends upon the radius r of the particles encountered during the propagation process:

1. if $r < \lambda$, we observe Rayleigh scattering;

2. if $r \approx \lambda$, we observe Mie scattering;

3. if $r > \lambda$, we observe geometric scattering.

The major role is observed for particles whose size is comparable to the wavelength.

Free-space loss

In an FSO communication system, the largest loss is usually due to the loss in the signal strength while propagating through the free space. The space loss factor is given by:

$$L_s = \left(\frac{\lambda}{4\pi R}\right)^2 \tag{1.2}$$

where R is the link range.

Beam divergence loss

As the optical beam propagates through the atmosphere, it spreads out due to diffraction, as illustrated in Figure 1.3. This kind of loss is also defined geometric loss. In dB, it is expressed as:

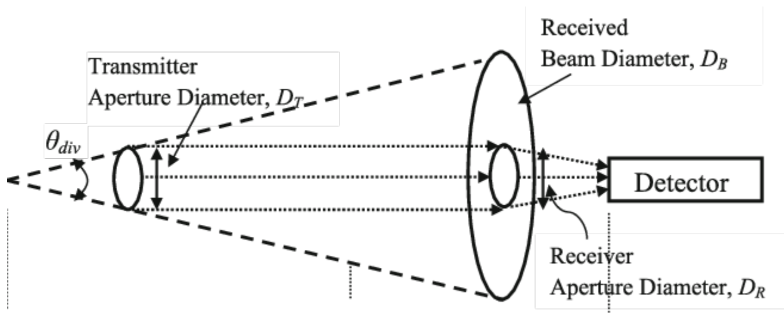

Figure 1.3: Loss due to beam divergence.

$$L_G = -10\left[2\log_{10}\left(\frac{4}{\pi}\right) + \log_{10}\left(\frac{A_T A_R}{\lambda^2 R^2}\right)\right] \tag{1.3}$$

Optical source with narrow beam divergence is preferable, even if more care should be taken during the alignment procedure, which can more easily fail.

Loss due to weather conditions

To predict the atmospheric environmental conditions, the definition of atmospheric visibility is exploited: it is the distance that a parallel luminous beam travels through in the atmosphere until its intensity drops 2% of its original value. In order to predict the optical attenuation statistics from the visibility statistics for estimating the availability of FSO system, the relationship between visibility and attenuation must be known. In particular, the attenuation of an optical signal propagating through a medium is named specific attenuation (attenuation per unit length expressed in dB/km):

$$\beta(\lambda) = \frac{1}{R} 10 \log_{10} \left(\frac{P_0}{P_R} \right) = \frac{1}{R} 10 \log_{10} \left(\exp(\gamma(\lambda) R) \right) \tag{1.4}$$

where R is the link length, P_0 is the optical power emitted from the transmitter, P_R the optical power at distance R, γ the atmospheric attenuation coefficient. The specific attenuation due to fog, snow and rain is described as follows:

1. Effect of fog: predicted by applying Mie scattering theory, or the empirical Kim model for Mie scattering:

   $$\beta_{log}(\lambda) = \frac{3.91}{V} \left(\frac{\lambda}{\lambda_0} \right)^{-p} \tag{1.5}$$

   where:

   - V(km) is the visibility range;
   - λ_0 is the operating wavelength;
   - λ(nm) is the visibility range reference wavelength; generally, it is 550 nm.
   - p is the size distribution coefficient of scattering.

2. Effect of snow: attenuation due to snow can vary depending upon the snowflake size and snowfall rate. It can be approximated by the empirical model:

   $$\alpha_{snow} = \frac{58}{V} \tag{1.6}$$

3. Effect of rain: the sizeable rain droplets can cause wavelength-independent scattering, and the attenuation produced by rainfall increases linearly with rainfall rate. The empirical formula approximating the rain impact is:

   $$\alpha_{rain} = \frac{2.8}{V} \tag{1.7}$$

Pointing Loss

This is the loss occurring due to imperfect alignment between transmitter and receiver. When large, the signal intolerably fades and the performance significantly degrades.

Atmospheric turbulence

The atmosphere can be thought as a viscous fluid that has two distinct states of motion: the laminar and the turbulent. In the first case, the velocity flow characteristics are uniform; in the second instance, the velocity loses its uniformity due to dynamic mixing and acquire random sub-flows called turbulent eddies. Depending on the size of turbulent eddies and transmitter beam size, three types of atmospheric turbulence effects are observed: beam wander (beam steering), causing a pointing error displacement; beam scintillation, leading to irradiance fluctuations at the receiver; beam spreading, causing independent diffraction and scattering.

Specifications	**FSO**	**Fiber Optics**
Transmitting medium	Air	Fiber cable
Permission	No permission required for transmission of laser beams	Requires permission for digging to lay fiber optic cables
Installation	Easy and fast	Difficult and time-consuming
Maintenance time	Short	Long
Cost	Moderate	High
Mobility	Possible, including reconfigurability	Not possible
Security	Moderate	High
Transmission speed	Variable, depending on the usage	100 Mbps to 100 Gbps
Applications	Between buildings, last-mile solution (short-distance)	Point-to-point (long-distance)
Advantages	Price and performance	Not susceptible to EMI Difficult to intercept, so more secure
Disadvantages	Can be intercepted so it is less secure	Difficult to terminate

Table 1.2: Differences between FSO and Fiber Optics communication systems.

1.1.5 Free-space optical communication

FSO is a line-of-sight technology propagating the light in free-space through air, outer space, vacuum, or something similar to wirelessly transmit data for telecommunication and computer networking. FSO for telecommunication is a reliable non-conventional transmission apparatus, proposed as an innovative alternative to fiber optics and radio-frequency systems.

FSO vs Fiber Optics

FSO communication system has many differences with respect to Optical Fiber Communication (OFC) system [2]. Table 1.2 provides a list.

FSO vs Radio-Frequency communication

FSO communication system offers several advantages over the radio-frequency (RF) system [3]:

- Wavelength: the NIR and MIR regions include wavelengths ranging from 0.78 µm up to 50 µm. The radio-frequency region comprises indeed wavelength higher than 1 mm.

- Huge modulation bandwidth: the usable bandwidth at an optical frequency is in the order of THz, which is almost 10^5 times that of a typical RF carrier. In fact, in RF and microwave communication systems, the allowable bandwidth can be up to 20% of the carrier frequency. In optical communication, even if the bandwidth is taken to be 1% of carrier frequency, the allowable bandwidth can be of the order of hundreds of THz.

- Narrow beam divergence: the beam divergence is $\sim \frac{\lambda}{D_R}$, with λ being the carrier wavelength, and D_R the aperture diameter. Consequently, the beam spread offered by the optical carrier is narrower than that of RF carrier. A much smaller beam divergence is translated into an increase in the intensity of the signal at the receiver for a given transmitted power.

- Less power and mass requirement: because of the smaller beam divergence, the FSO system's antennas are smaller to achieve the same gain (antenna gain is inversely proportional to the square of operating wavelength).
  Moreover, FSO system is easily expandable and reduces the size of network segments, leading also to a higher compactness.

- High directivity: small-sized antennas guarantee very high directivity.

- Security: thanks to the narrow beam divergence, it is difficult to detect the transmitted optical beam as compared to RF signal. In order to detect the transmitted signal, one has to be physically very close to the beam spot diameter in the optical and mid-infrared domain. On the contrary, RF signals have much wider region of listening.

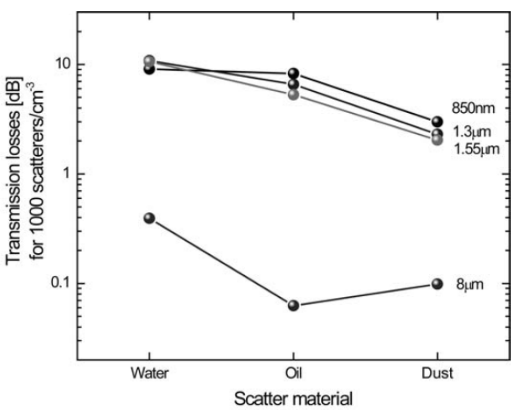

Figure 1.4: Summary analysis of the study reported in [4]. The presence of water fog, oil fog and dust results to be particularly detrimental for the NIR wavelengths. As concerns the 8 µm wavelength, instead, the stronger transmission losses are measured for water, having at least one order of magnitude of difference with respect to dust and oil.

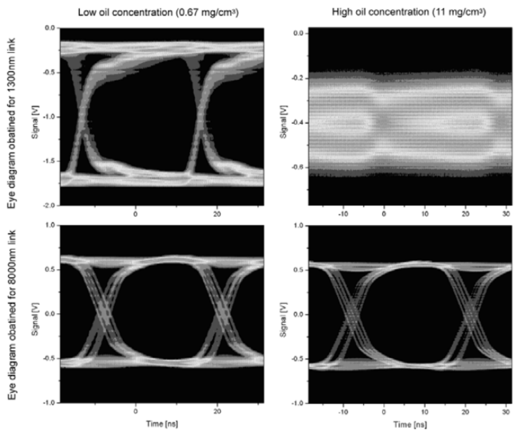

Figure 1.5: Eye diagrams resulting from the digital communication performed at 1.33 µm (first row) and at 8 µm (second row), at a data rate of 34 Mbit/s, under corresponding conditions of low concentration (left) and high concentration (right). The NIR link proves unable to sustain error-free transmission at the highest attenuation levels; the MIR link remains error-free under the same particle density conditions. Courtesy of [4].

However, there are also some drawbacks too:

- Tight alignment and pointing, due to the narrow beam divergence.

- Clear line-of-sight is required from the transmitter to the receiver, since light cannot penetrate walls, hills, buildings, etc.

- Atmospheric conditions dependency: system performances drastically degrade because of the atmospheric impact.

NIR FSO vs MIR FSO

The advent of the quantum cascade lasers (QCL) with emission wavelengths available in the infrared range from 3 µm up to more than 100 µm opens up the possibility of exploiting the infrared atmospheric transparency window for FSO. The choice of source wavelength is a critical parameter in the design of FSO systems, because of the effective impact of molecular absorption, light scattering and atmospheric particles' presence, all contributing to create a more complex and less controlled transmission medium.

The behavior and the performance of NIR and MIR wavelengths have been studied under adverse conditions with reduced visibility [4] [5], proving enhanced link stability (2x, 3x) and power in MIR systems with respect to conventional NIR systems. This is mainly attributed to reduced scattering in MIR light in haze and fog. The following list summarizes the main advantages of MIR wavelengths over NIR wavelengths:

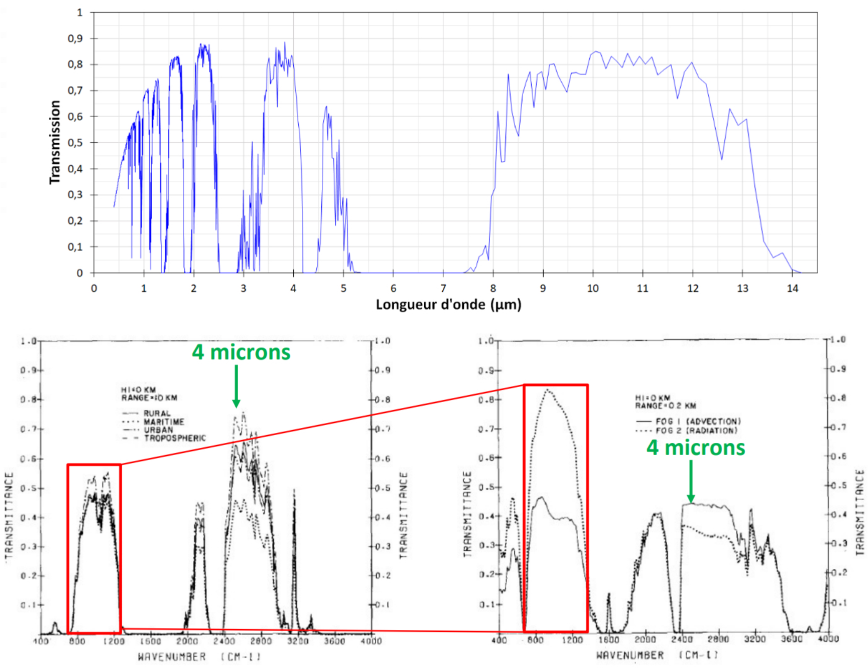

Figure 1.6: Transmission spectrum of the atmosphere: (top panel) clear weather condition (courtesy of [6]); (bottom panel) fog weather condition (courtesy of [7]).

- Low absorption [6]: the top panel of Figure 1.6 represents the transmission spectrum in the [0-15] µm window. In the MIR range, we can recognize several wavelengths that guarantees higher transmission coefficients compared to conventional NIR wavelengths: band 1 (1.5-2.5 µm), band 2 (3-5 µm), band

3 (8-14 µm). These wavelengths benefit from very low attenuation in the atmosphere, guaranteeing very long propagation distances.
Moreover, it is true that in clear weather conditions band 1 and band 2 display a higher transmittance; however, the bottom panel of Figure 1.6 shows that fog particles compromise the performance in band 1 and band 2; on the contrary, band 3 performance appears almost unaltered. Hence the demand for utilizing wavelengths belonging to the thermal atmospheric window [7].

- Low scattering [5]: a longer wavelength source propagates more effectively through micron-sized suspended particles such as haze and fog. Reduced effective scattering is thought to be the principle mechanism for this effect.

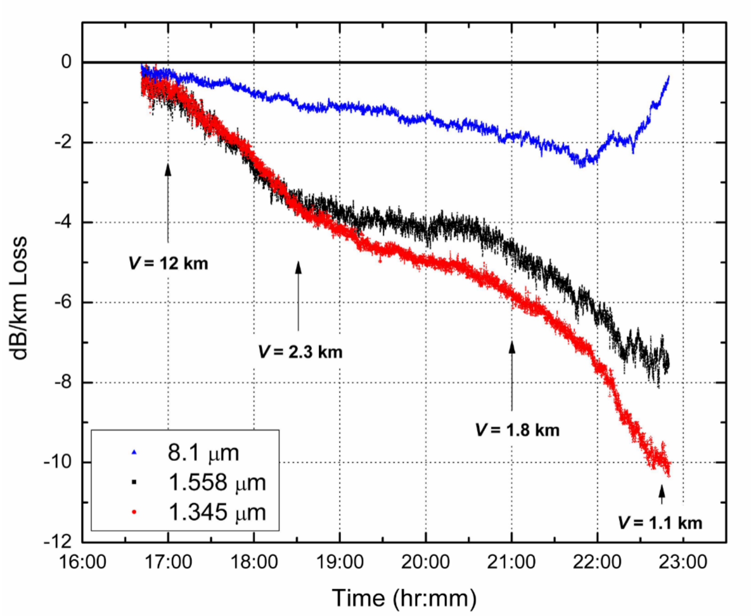

Figure 1.7: Evolution of the transmission losses when varying the humidity of the atmosphere and thus, the visibility, for three wavelengths (8.1, 1.558, 1.345 µm): stronger attenuation is seen at shorter wavelengths.

- Resistance to turbulence [8]: turbulence on the propagation path significantly deteriorates the optical signal, causing beam spreading, beam wandering, scintillation or loss of spacial coherence [9]. Scintillation is the predominant phenomenon, evolving as a function of $\lambda^{-7/6}$: the higher the wavelength, the less significant its impact on the beam.

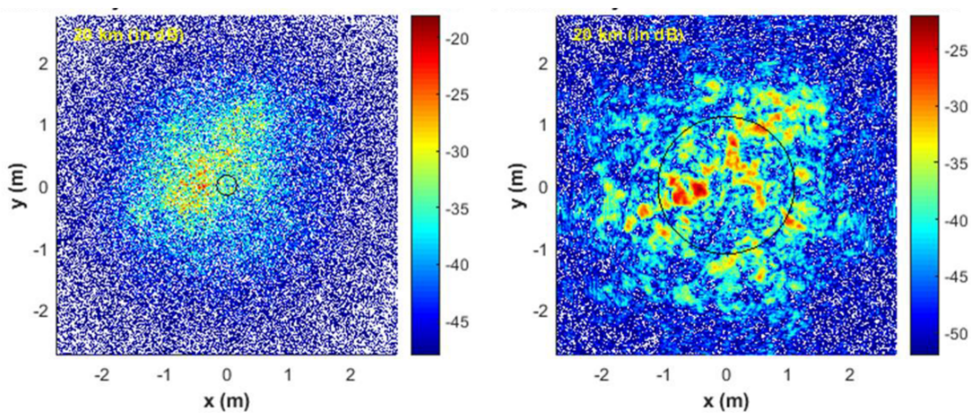

Figure 1.8: Simulated beam intensity profile in decibel units after a 20 km propagation through atmosphere for 1.55 µm (left chart) and 10.6 µm (right chart). Solid lines show beam size due to diffraction only. Courtesy of [8].

- Stealth of the transmitted signal: the thermal black-body radiation shows a strong background in the 8-15 µm range [10]. So, it becomes more difficult to detect a secure transmission in the MIR window.
- Eye safety: visible and NIR regions have the highest potential to damage the retina of the eye, leading to permanent loss of vision or eye hazards, together with skin damage. This is due to the fact that the cornea is transparent to these wavelengths. On the contrary, it acts as a band-pass filter for wavelengths below 400 nm and above 1400 nm, highly reducing the risk of laser injuries.

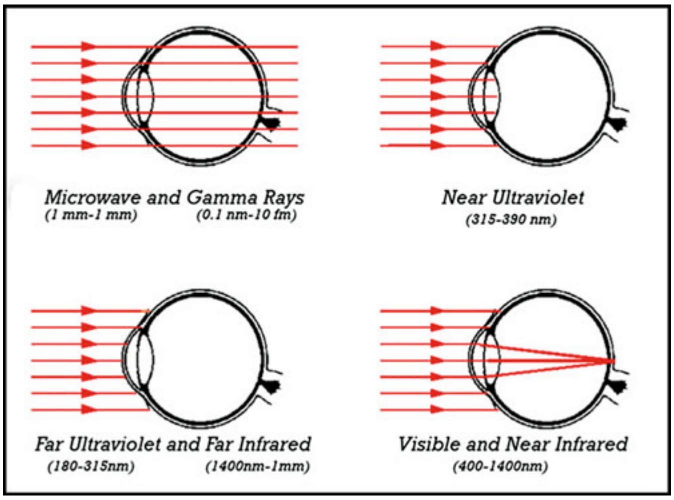

Figure 1.9: Pictorial representation of light absorption in the eye for different wavelengths [3].

1.2 Mid-Infrared wavelengths: applications

Several are the possible applications of mid-infrared optical sources. In the following, some of them are illustrated.

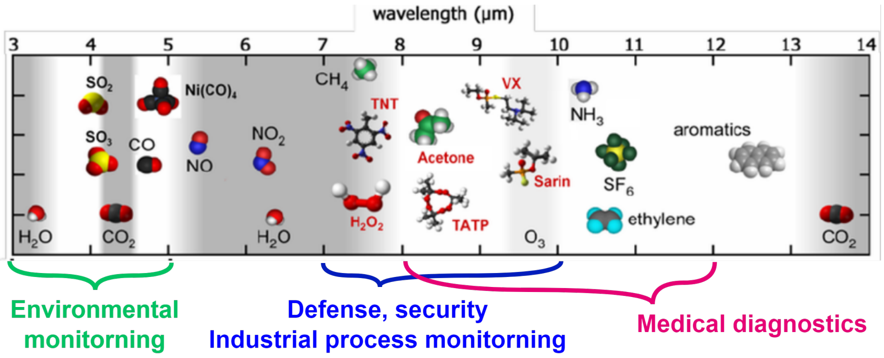

Figure 1.10: Molecules of interest accessible in the MIR.

1.2.1 Laser absorption spectroscopy

Laser absorption spectroscopy of trace gases is a technique that identifies chemicals based on the interaction of molecules with EM radiation in the MIR. Chemical species are identified based on the absorption of specific wavelengths of MIR light by a molecule, serving as a molecular fingerprint. Molecular absorbances cause molecular rotations and vibrations and are classified by chemical functional groups. The resulting MIR spectrum produced is characteristic for a given molecule, and shows absorption peaks at the molecule vibrational frequencies.
While one can also address some of the molecules via overtone absorption lines in the NIR, where laser sources are easier to make, it is advantageous to use the strong fundamental absorption lines in the MIR for maximum sensitivity. Moreover, many molecules and chemicals strongly absorb at MIR. Consequently, MIR lasers reveal to be more efficient than their NIR counterparts. The applications of laser absorption spectroscopy can be several: from the medical diagnostics to the remote sensing in environmental monitoring. In the former instance, QCLs proved to be efficient for the diagnosis of breast cancer [11]; furthermore, QCLs are very promising for non-invasive determination of glucose, lactate and triglycerides in blood serum.
In the latter instance, instead, mid-infrared sources have demonstrated fundamental in the monitoring of toxic or polluting gases for industrial control, as well as in the detection of explosives, drugs or weapons for safety applications [12]. Figure 1.10 depicts the wavelengths of interest for the aforementioned applications.

1.2.2 Optical countermeasure systems

High-power mid-IR sources can find a military application for directional infrared countermeasures (DIRCM) [12] to protect aircraft from heat-seeking missiles, for example those launched from manportable air defense systems.
Depending on the technology, these missiles will operate: in the 0.5-2.5 µm range to follow very hot sources such as airplane nozzles; in the 3-5 µm range, in order to follow targets emitting between 300 and 1000 K; in the 8-14 µm range, to follow could sources such as naval ships (infrared tracking). If they are jammed by a modulated high-power mid-infrared beam, these missiles can be deflected so that they miss their target.
Besides rather high output powers, which are suitable for blinding infrared cameras, broad spectral coverage within the atmospheric transmission bands (around 3–4 µm and 8–13 µm) is required, preventing the protection of infrared detectors with simple notch filters [13]. For this reason, optical countermeasure systems is one of the most promising fields of applications for high-power QCLs.

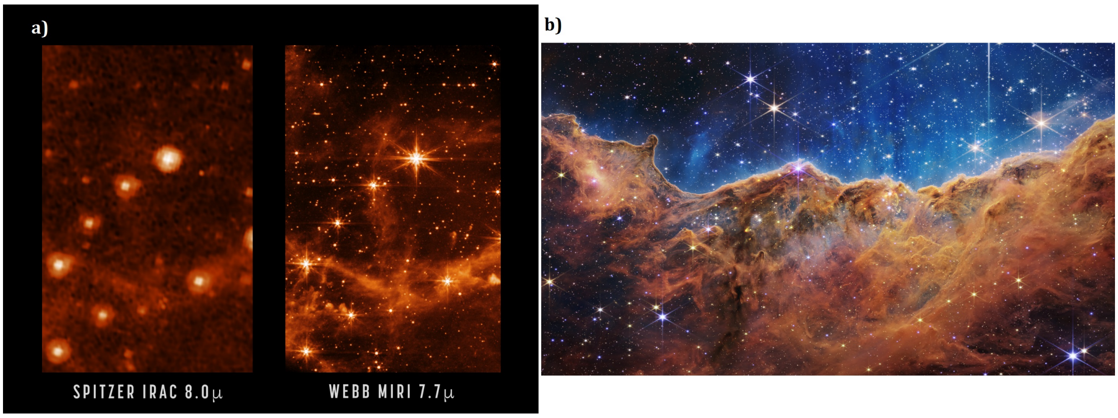

Figure 1.11: (a) This combination of images provided by NASA shows part of the Large Magellanic Cloud, a small satellite galaxy of the Milky Way, seen by the retired Spitzer Space Telescope (left), and the new James Webb Space Telescope (right). The high-resolution is thanks to the ongoing development of mid-infrared technology. (b) Captured in infrared light by NASA's new James Webb Space Telescope, this image reveals for the first time previously invisible areas of star birth. Courtesy of [14].

1.2.3 Free-space optical communication

The mentioned atmospheric transmission windows can also be utilized for free-space optical communications with directed beams, like with QCLs. More information will be provided in the following chapters, being one of the main concern of this study.

1.2.4 Infrared astronomy

Infrared astronomy is a field of astronomy that studies astronomical objects that are visible in infrared radiation. By using telescopes and solid-state detectors, astronomers are able to observe objects in the universe which are impossible to detect using light in the visible range of the electromagnetic spectrum.
A considerable success in this field is MIRI, the mid-infrared instrument, part of NASA's Webb telescope. It has both a camera and a spectrograph that sees light in the mid-infrared region of the electromagnetic spectrum, with wavelengths in the range 5-28 μm. It allows to see the redshifted light of distant galaxies, newly forming stars, and faintly visible comets as well as objects in the Kuiper Belt. The incredible advances in the mid-infrared technology lead to the recently high-resolution images from the Milky Way spread by the NASA laboratory.

1.3 Mid-Infrared coherent sources

The dramatic increase in availability of mid-infrared light sources in the last decades can be mainly accounted to the development of novel materials and the improving quality of traditional MIR materials [15].

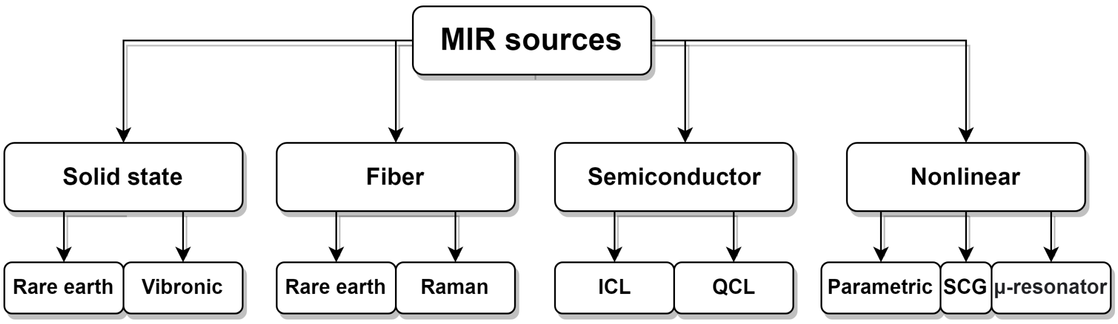

Figure 1.12: Different types of MIR coherent sources.

1.3.1 Nonlinear sources

Nonlinear sources output MIR radiation through nonlinear frequency conversion of commonly available light sources. The nonlinear generation takes the form of:

1. parametric processes: starting with a single NIR laser, and pumping an optical parametric oscillator (OPO), amplifier (OPA) or generator (OPG), it is possible to generate an idler wave in the mid-infrared spectral region.

2. supercontinuum generation (SCG): high-intensity pulses propagates through a nonlinear material (like mid-infrared fibers), and spectrally broadens due to four-wave mixing (FWM) and Raman scattering (energy transfer to longer wavelength through scattering with optical photons).

3. microresonators: they can either broaden a pump source through FWM, or create a broadband frequency comb with pulsed output.

1.3.2 Semiconductor lasers

Semiconductor lasers can exploit either intersubband transitions or interband transitions; in the former case, we speak about quantum-cascade lasers; in the latter case, we speak about interband cascade lasers (ICL). Both are compact and electrically driven, but the QCL is the most commercially developed one. A deep insight on QCLs is provided in the following chapters. As regards the ICL, it is characterized by a cascade scheme very similar to that of QCLs, but the radiative transition occurs between the conduction and the valence bands. The first ICL was proposed in 1995 [16] and fabricated in 1997 [17]. The implementation of ICLs on Silicon has been already proved successful [18]; silicon-based QCLs require more issues to be faced, but some solutions have been proposed too [19].

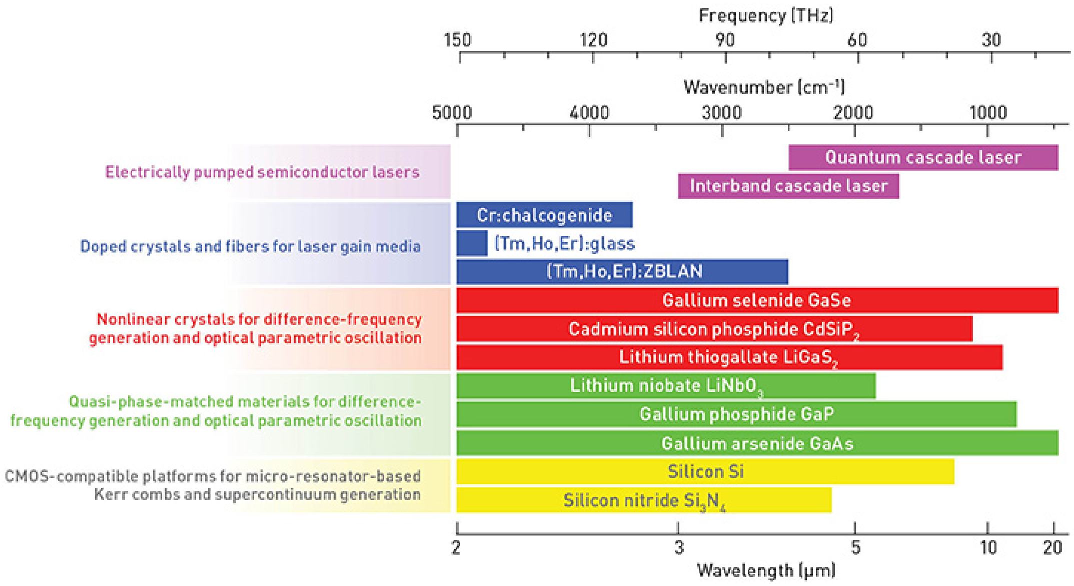

Figure 1.13: Operating wavelengths of different MIR coherent sources. Courtesy of [20].

1.3.3 Fiber lasers

Fiber lasers have become ubiquitous over the last decade, largely due to a few key characteristics: high efficiency, compact packaging, superior reliability, excellent beam quality and broad gain bandwidth. This has enabled fiber lasers to be used in many applications, from industrial machining to medicine and telecommunications. According to the dopant used, different emission wavelengths can be achieved, spanning from 2.8 to 4 µm: erbium-doped fluoride fibers, holmium-doped [21] [22] [23] [24] fibers and dysprosium-doped fluoride fibers [25]. In some cases, it is necessary to use additional rare-earth dopants which serve to depopulate the lower laser level via energy transfers, because the used laser transition would otherwise be self-terminating.
The common silica fibers cannot be used in the mid-infrared. First of all, they exhibit strong absorption at such long wavelengths. Second, the high phonon energy would allow strong multi-phonon transitions to bypass the laser transitions. Both problems can be solved by using suitable other glasses (usually, fluoride glasses or chalcogenide glasses).

1.3.4 Solid-state lasers

Nowadays, most solid-state lasers are developed from electronic transitions in rare-earth ions and vibronic transitions (coupling between phonon and electronics states) in transition metals.
Vibronic sources in the MIR region are perhaps more useful for several applications because they can provide much wider gain bandwidths than the rare-earth ions due to broadening caused by coupling between phonon and electronic states.
Moreover, modifying the host material of a vibronic source causes a much larger change in the emission spectrum than in the case of rare-earth ions due to the coupling between phonon and electronic states.

Chapter 2

Quantum cascade lasers

2.1 Introduction

This chapter is dedicated to the introduction and description of the quantum cascade laser, a unipolar semiconductor device that has become the laser of choice for long-wavelength operation. In fact, double heterostructure devices have been commercialized for wavelength from the visible blue up to the near-infrared (around 1.6 µm); however, these lasers are not suitable for emitting light in the mid-infrared range (2-20 µm), which requires very narrow bandgaps. The invention of QCLs [26] largely satisfies the increasing need for compact, high-performance, room-temperature, and reliable mid-infrared laser sources.

2.2 QCL: fundamental operating principle and mathematical model

Quantum cascade lasers are compact semiconductor devices, based on intersubband transitions in a multiple quantum-well (QW) heterostructure. They are unipolar sources, involving therefore only one type of carrier: the stimulated emission is based no more on the electron-hole recombination between the conduction band and the valence band, as in standard semiconductor lasers. The QCL approach is totally different, being based on two fundamental phenomena of quantum mechanics: tunneling and quantum confinement. As a result, QCL's fundamental principles are independent of the specific semiconductor system: while diode lasers emit with photon energy similar to the bandgap energy, QCLs can emit with any photon energy that can be designed within the heterostructure. Hence, QCLs' emission wavelength ranges from 2 to 250 µm under standard operating conditions, enabling the possibility to emit light also in the so-called THz window. In fact, the shorter achievable wavelengths are limited by the conduction band discontinuity; the long-infrared wavelengths, instead, do not present any fundamental limit. Nevertheless, the most commercially available QCLs tend to be in the 4-11 µm range, using combinations of commonly used III-V semiconductors as InGaAs/AlInAs/InP, GaAs/AlGaAs and InAs/AlSb. Figure 2.1 provides a figurative comparison between the SLs' photon emission principle and the QCLs' one.

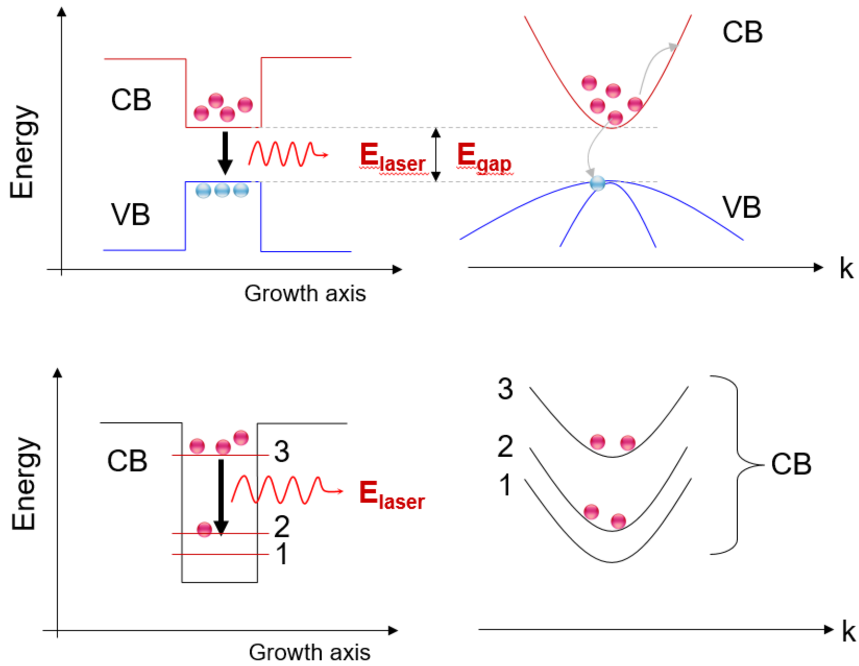

Figure 2.1: (Left) Comparison of interband (top) and intersubband (bottom) transitions in a quantum well laser. (Right) Corresponding energy band diagram. In the reciprocal space, the initial and the final states have the same curvature in the case of intersubband transitions.

At the simplest level, the QCL consists of a series of quantum wells, creating a superlattice structure: it is indeed an artificial semiconductor material made up of a large number of periods; each period holds two layers of dissimilar materials presenting different gap energies but similar lattice constants. This allows for the creation of ultrathin layers, called quantum wells. Since their size is comparable to the electrons' De Broglie wavelength, they quantize the electrons energy levels in the direction perpendicular to the plane of the layers. Consequently, the emission process derives from the quantum confinement of the electron within the QW: an electron can relax from one subband (higher energy) to the other (lower energy) of the same conduction band by discrete steps, sometimes emitting photons. The spacing between the energy levels depends on the thickness of the quantum well, as Figure 2.2 well illustrates: the wider the QW, the closer the energy levels are one with respect to the other. Hence, the longer the emission wavelength would be, being it inversely proportional to the emitted photon's energy:

$$E_n = n^2 \frac{\hbar^2 \pi^2}{8ma}$$

where a is the thickness of the well, and n is the quantum state number.
If the QW is too narrow, the upper subband risks to be close to the continuum; therefore, no electron confinement and subsequent photon emission are possible. By contrast, if the well size is too big, the subbands will be very close, leading the thermal relaxation to compete with the radiative transitions.
Finally, also the choice of the barrier's materials is of primary importance in the engineering process of the optical transitions.

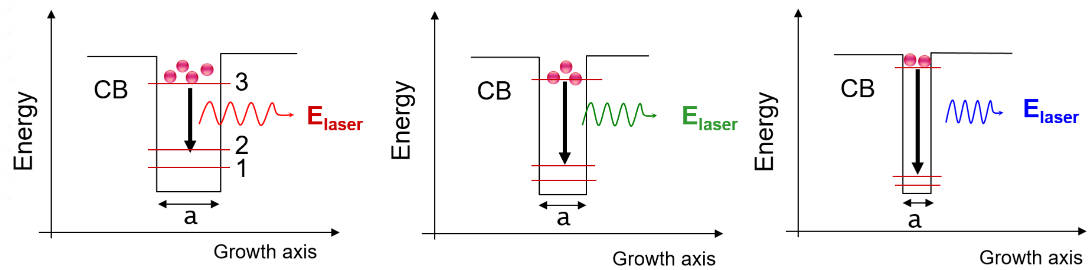

Figure 2.2: Intersubband transition's dependence on the QW thickness: from right to left, the thickness decreases, causing an increase in the spacing between the energy levels, and a decrease of the emission wavelength.

Apart from unipolarity, another feature which distinguishes QCLs from standard SLs is the cascading heterostructure: they consist of a sequence of Z cascaded periods, each comprising an intrinsic QW active region, and an n-type electron injector/relaxation region (Figure 2.3). Typically, Z is ∼25-35 [27][28].
The injector region is made up of a series of wells of varying widths and thin barriers, forming a superlattice. Thus, it can be seen overall as a miniband, terminating with a final injector barrier: the latter avoids the back scattering of electrons from level 3 into the preceding miniband. Hence, the miniband together with the injector serves as an electron reservoir separating the individual gain stages of the active region.
The active region can be indeed described as a three-level system, where each level is a confined state.

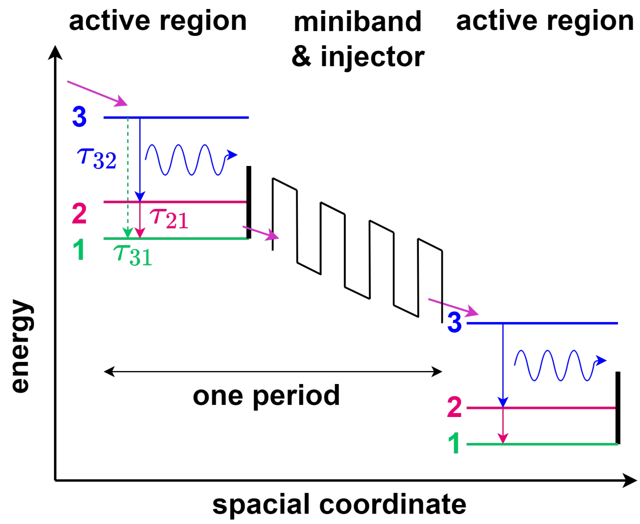

Figure 2.3: Schematic energy level diagram of the conduction band of QCL showing two gain stages, connected by a miniband and an injector. The laser transition occurs between level 3 and level 2 (in blue). The electron transport is indicated in purple. The spacial coordinate represents the direction of the current flow within the laser.

When a bias is present, electrons are injected via resonant tunneling in the upper state of the active region (level 3). They relax through a radiative transition from level 3 to level 2; then, the carriers relax into level 1 by the emission of a longitudinal-optical phonon. At this point, the electron will be transported through the relaxation region and injected into the upper state of the following period's active region.
As a result, if Z is the number of the periods of the structure, each electron involved in the process can generate at most Z photons, when cascading across the structure itself.
The lifetime of the transition from level 3 to level 2 must be longer compared to the electron's lifetime in level 2 in order to achieve the population inversion condition, which is a fundamental requirement to have gain.
If the population inversion is ensured, by increasing the current, it is possible to reach the threshold: the condition for which the gain equals the losses is met, therefore the injected electrons are converted into photons emitted by stimulated emission. The emitted power depends linearly on the injected current.
Considering Figure 2.3, let us define τ_c as the carrier lifetime, that is the lifetime of level 3; similarly, τ_{31} is the lifetime of the transition from level 3 to level 1, τ_{32} is the lifetime of the transition from level 3 to level 2 and τ_{21} is the lifetime of the

transition from level 2 to level 1. It is possible to approximately state that [29]:

$$\frac{1}{\tau_c} \approx \frac{1}{\tau_{31}} + \frac{1}{\tau_{32}} \tag{2.1}$$

Instead, the effective gain g_c for all the gain stages is defined as:

$$g_c = g(n_3 - n_2) \tag{2.2}$$

where n_3, n_2 denote the carrier populations of the third and second energy levels (unit: cm^{-2}) of the gain stages. g, indeed, is the effective differential gain coefficient:

$$g = \frac{q}{ZI_{in,th}} \cdot \frac{1}{\tau_p} \cdot \frac{\tau_{32} + \tau_{31}}{\tau_{32}\tau_{31} - \tau_{21}\tau_{31}} \tag{2.3}$$

where q is the electron charge (C), τ_p (s) is the photon lifetime and $I_{in,th}$ (A) is the injected current into the upper laser level at laser threshold.
Finally, it is possible to introduce the so-called rate equations, a set of nonlinear differential equations expressing the temporal evolution of the carrier numbers in the three energy levels, as well as the photon number [30]:

$$\frac{dn_3}{dt} = \eta\frac{J}{q} - \frac{n_3}{\tau_c} - Sg_c(n_3 - n_2) \tag{2.4}$$

$$\frac{dn_2}{dt} = (1-\eta)\frac{J}{q}\frac{n_3}{\tau_{32}} + Sg_c(n_3 - n_2) - \frac{n_3 - n_{th}}{\tau_2} \tag{2.5}$$

$$\frac{dS}{dt} = \frac{c}{n_{eff}}\left[[Sg_c(n_3 - n_2) - S\alpha_{tot}] + \frac{\beta n_3}{\tau_{sp}}\right] \tag{2.6}$$

where:

- η: injection efficiency describing the percentage of the electrons that are injected from level 1 in a given active region into level 3 in the following active region;
- J: injection current density (Acm^{-2});
- S: photon flux within the cavity (s^{-1}cm^{-2});
- g_c: peak gain cross-section (cm^2);
- $n_{th} = n_g \exp\left(\frac{-\Delta_{inj}}{k_B T}\right)$: equilibrium population level (or thermal population level), with n_g, the sheet doping density of the injector and Δ_{inj}, the energy difference between the Fermi level of the injector and level 2. This quantity is related to the thermal backfilling effect, but more explanations are provided hereafter.

- $\frac{c}{n_{eff}}$ the speed of the photons in the material (cm/s);
- α_{tot}: sum of waveguide and mirror losses (cm^{-1});
- β: fraction of spontaneous emission coupled in the laser mode;
- τ_{sp}: spontaneous emission lifetime.

These equations represent only one period of the active region; however, the QCL has many periods, sharing the same optical waveguide.
In particular, we can define $\frac{(n_3-n_2)}{L_p} = \Delta N$ as the population inversion density:

$$\Delta N = \frac{J}{qL_p}\left(\eta\tau_{eff} - (1-\eta)\tau_2\right) \tag{2.7}$$

where L_p is the length of one period of the active region (cm) and $\tau_{eff} = \tau_c\left(1 - \frac{\tau_2}{\tau_{32}}\right)$ expresses the relationship between the population inversion and the electrical pumping. From this formula, it is possible to confirm what stated before: the population inversion does exist only if $\tau_2 < \tau_{32}$.
However, we can also take into consideration the so-called thermal backfilling effect:

$$\Delta N = \frac{J\tau_{eff}}{qL_p} - n_{th} \tag{2.8}$$

This population originates from carriers thermally excited to the lower state from the injection region. This is an undesired effect, therefore it should be minimized by properly choosing the design parameters. In order to achieve transparency, n_{th} must be compensated by the same upper-state population.

2.2.1 Threshold current

If the population inversion is ensured, the stimulated emission begins when the threshold condition is satisfied: the modal gain $\Gamma\Delta N g_c$ (effective gain experienced by the lasing optical mode which has an overlapping with the gain medium) compensates for the total losses $\alpha_{tot} = \alpha_m + \alpha_w$:

$$\Gamma\Delta N g_c = \alpha_{tot} \tag{2.9}$$

where Γ is the optical confinement factor. Hence, the threshold current density is expressed as:

$$J_{th} = q\frac{\alpha_{tot}}{g_c\Gamma L_p}\frac{1}{\eta\tau_{eff} - (1-\eta)\tau_2} \tag{2.10}$$

However, the threshold current density is a weakly temperature-dependent parameter, conveniently fitted by the expression:

$$J_{th} \; = \; J_0 \exp\left(\frac{T_a}{T_0}\right) \tag{2.11}$$

where J_0 and T_0 are the characteristic current and temperature of the QCL. The latter is a relevant indicator of the performances of the QCL and evaluates the stability of the threshold current when varying the temperature. The higher its value, the smaller the sensitivity to temperature changes.
In the case the backfilling effect is considered, the threshold current density's expression becomes more complex:

$$J_{th} \; = \; q\left[\frac{\alpha_{tot}}{g_c \Gamma L_p} + n_{th}\right]\frac{1}{\eta\tau_{eff} - (1-\eta)\tau_2} \tag{2.12}$$

2.2.2 Slope efficiency

The slope efficiency measures how much optical power is generated with an additional unit of current injected into a QCL above the threshold current [31]:

$$\frac{dP}{dI} \; = \; \frac{h\omega}{2\pi q} Z \frac{\alpha_m}{\alpha_m + \alpha_w}\left[\frac{\eta\tau_{eff} - (1-\eta)\tau_2}{\tau_2 = \tau_{eff}}\right] \tag{2.13}$$

In particular, $\eta_i \;:=\; \left[\frac{\eta\tau_{eff} - (1-\eta)\tau_2}{\tau_2 = \tau_{eff}}\right]$ is the internal efficiency. Its value is smaller than 1; nevertheless, the multiplication by Z takes into account the presence of the cascaded periods, which allows for the differential quantum efficiency to be greater than unity. This is physically possible since a single injected electron can emit several photons, because of the sequenced stages.

2.2.3 Wall-plug efficiency

The wall-plug efficiency (WPE) defines the ratio between the optical power generated by a QCL and the total electrical power consumed by it [32]:

$$\eta_{wp} \; = \; \frac{I - I_{th}}{I}\frac{\hbar\omega}{\hbar\omega + \Delta_{inj}} Z \frac{\alpha_m}{\alpha_m + \alpha_w}\left[\frac{\eta\tau_{eff} - (1-\eta)\tau_2}{\tau_2 = \tau_{eff}}\right] \tag{2.14}$$

This parameter is as complicated to measure as crucial, since it impacts on the QCL applications: the lower η_{wp}, the higher the demand on the power supply and heat dissipation system. Moreover, it depends on many factors, such as the operation temperature, the quantum structure design, the waveguide length and losses. Hence, in order to improve it, a trade-off between the various design parameters is needed.

2.2.4 Losses measurements

To correctly model the QCL's functioning, we need to properly describe the device losses. As already mentioned, we have the mirror loss (α_m) and the waveguide loss (α_w).

Mirror loss

A typical QCL is constructed based on Fabry-Perot cavity formed by two parallel, cleaved semiconductor facets with a reflectivity R. Being n_{eff} the effective refractive index of the lasing mode, R is defined as:

$$R = \left(\frac{n_{eff}-1}{n_{eff}+1}\right)^2 \tag{2.15}$$

Hence, being L the cavity length, the mirror loss is expressed as:

$$\alpha_m = \frac{1}{2L}\ln R_1 R_2 \tag{2.16}$$

Waveguide loss

Waveguide loss has several contributions, sketched in Figure 2.4:

$$\alpha_{tot} = (1-\Gamma)\alpha_{fc} + \alpha_{scatt} + \Gamma\alpha_{nr} \tag{2.17}$$

where:

- $(1-\Gamma)\alpha_{fc}$: cladding loss, mostly originated from free carrier absorption α_{fc}.
- α_{scatt}: scattering loss, originating from the waveguide sidewall roughness, whose scale is much smaller than the wavelength.
  It has been experimentally observed that scattering loss affects more the slope efficiency rather than the threshold current, especially for shorter wavelengths (3-5 µm range) [33]. More specifically, the sidewall roughness acts as a distributed reflector, reducing the mirror loss rather than increasing the waveguide loss, since the scattering makes the mode to couple with counter-propagating mode.
- $\Gamma\alpha_{nr}$: non-resonant loss. It derives from all the non-resonant transitions in the active region.

There is a further contribution depicted in Figure 2.4: $\Gamma\alpha_{res}$, namely the resonance loss. It is linked to the thermal backfilling effect, impacting on the threshold current density only. It does not appear in Equation 2.17 since it is already taken into account in the rate equation model.

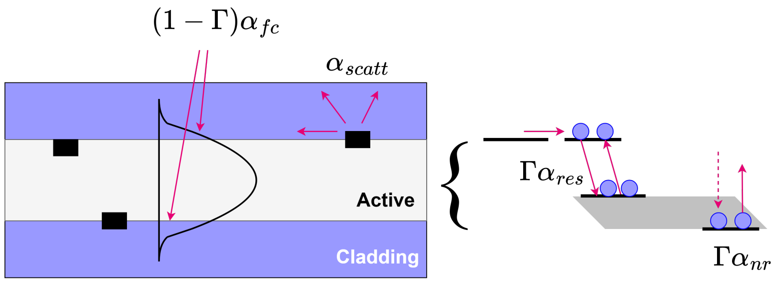

Figure 2.4: Schematic description of the various contributions to the waveguide losses

Waveguide loss is essential to characterize and improve the active regions design since it limits both the threshold current density and the slope efficiency.

2.3 QCL dynamics

2.3.1 Linewidth Enhancement Factor

The linewidth enhancement factor, also known either as chirp parameter, or Henry's α parameter [34] is a fundamental dynamical property attributing a parasitic change in the carrier frequency and effective refractive index of the lasing mode(s) to a variation of the current injection under direct modulation:

$$\alpha = \left[-\frac{4\pi}{\lambda_0} \frac{d\delta n/dN}{dg/dN} \right]_{\lambda=\lambda_0} \tag{2.18}$$

where λ_0 is the free-space emission wavelength, δn is the carrier contribution to the refractive index, g is the gain coefficient, and N is the carrier density in the active region.
In interband SLs, the α factor takes most typically large values, in the range of 4 to 6. This brings several undesirable effects, such as a broadening of the laser linewidth by a factor of $1+\alpha^2$ [34]. In interband lasers, this is caused by asymmetric gain spectra associated with the opposite curvature of the conduction and valence bands, as shown in Figure 2.5.
On the other hand, the QCL transitions occur between subbands of nearly the same curvature; thus, the gain spectrum is approximately symmetric, with a consequent chirp parameter which is negligible (in the range 0.1 to 0.5). However, this is true only in theory: indeed, different studies [35] [36] have demonstrated an α-factor between 0.8 and 2.9, depending on the injection current. This value is also more compatible with the destabilization of QCLs, and consequent exhibition of chaotic

behaviors [37]. This strong increase of the LEF with the pump current originates from gain nonlinearities and especially from gain compression, caused by spatial hole burning, due to an extremely fast gain grating lifetime linked to the upper state lifetime of few picoseconds.

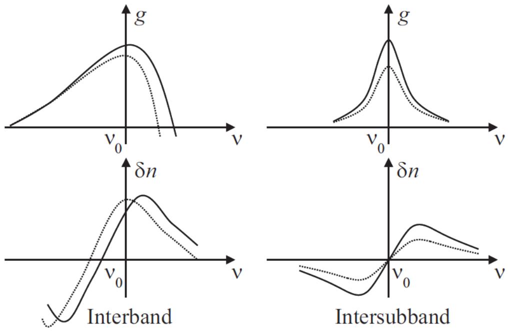

Figure 2.5: Schematic gain coefficient g and carrier-induced refractive index δn versus optical frequency ν for the case of interband (left) and intersubband transitions (right). The dotted and solid lines correspond to two different values of the injected carrier density N. Courtesy of [38].

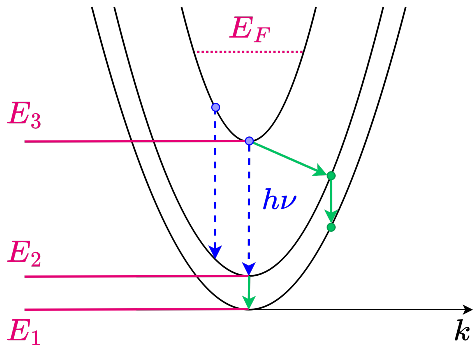

Figure 2.6: In-plane energy dispersion of the three-level system model of the QCL's active region [38]. The radiative stimulated transitions are denoted by the blue arrows. The green arrows illustrate non-radiative decay processes mediated by the emission of LO phonons.

2.3.2 Population Inversion Relaxation lifetime

The relaxation lifetime of the laser population inversion is of primary importance in the determination of the dynamics of QCLs, especially in terms of laser modulation bandwidth. In fact, as concerns conventional semiconductor lasers, this quantity

does not exceed a few tens of GHz, since the carrier lifetime is of the order of a nanosecond. In fact, the interband recombination takes mainly the form of Auger recombination and spontaneous radiative recombination [39].
By contrast, in QCLs the population inversion results from a non-equilibrium electronic distribution in the conduction subbands of the superlattice [38]. As Figure 2.6 represents, the non-radiative electronic decay from a higher-energy state to a lower-energy state is mediated by the emission of longitudinal optical (LO) phonons. Since this relaxation mechanism is extremely fast, the time scale of these processes ranges from a few picoseconds to a few hundred femtoseconds. Therefore, the relaxation mechanism in QCLs results at least three orders of magnitude higher than in other semiconductor lasers.
As a consequence, QCLs are particularly suited for high-speed operations, even if lots of efforts are necessary for the active region optimization. This is essential since intersubband active materials have intrinsically low radiative efficiencies.

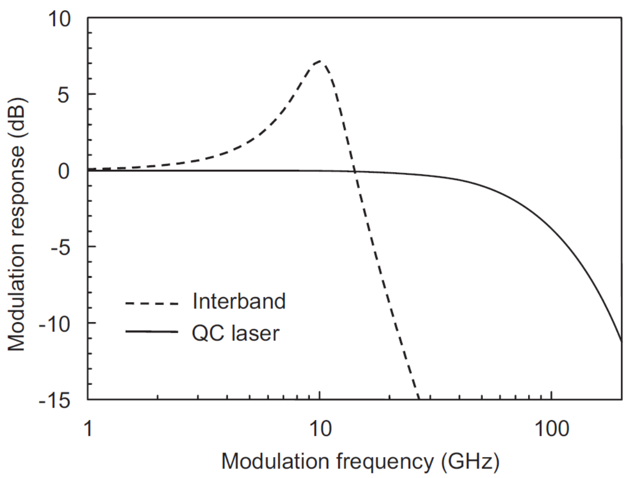

Figure 2.7: Schematic modulation response of a typical interband diode laser (dashed line) and QCL (solid line). The latter is characterized by the absence of the relaxation oscillation resonance and by a cutoff frequency that can exceed 100 GHz. Courtesy of [38].

2.3.3 Relaxation oscillations and modulation bandwidth

The modulation response (laser modulation efficiency as a function of the modulation frequency) manifests the principal dynamic properties of a laser. The main differences between conventional SLs and QCLs are particularly evident in Figure 2.7. A typical high-speed interband diode laser has a pronounced resonance peak associated with relaxation oscillations. They follow every change in the laser pumping level, causing coupled damped oscillations of both the population inversion

and the laser field. More specifically, they are provided by stimulated emission and gain saturation [40].
By contrast, QCLs do not present relaxation oscillations because of the ultrafast carrier relaxation dynamics, causing overdamped oscillations of both the laser field and the population inversion. As a consequence, QCLs' modulation bandwidth can exceed hundreds of GHz. Early work [41] even predicted the possibility of terahertz cutoff frequencies, although this conclusion has been subsequently disputed [42].
In effect, a study [43] has demonstrated that the QCL's modulation bandwidth is limited by the intrinsic cascading heterostructure of the device itself. In fact, there is a characteristic time delay for the whole QCL structure to respond to the drive current change, because a propagation through the all Z periods is needed.
Figure 2.8 compares the modulation transfer function including (blue line) and excluding (red line) the transport delay in the QCL modeling.

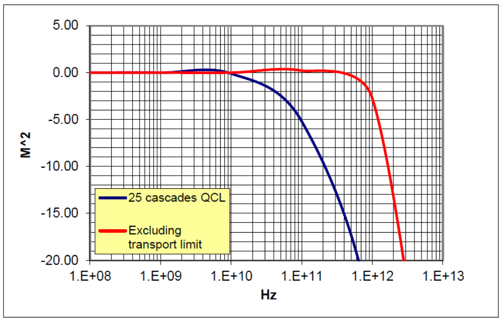

Figure 2.8: Modulation transfer functions of a 25-stages QCL: (blue line) including the transport delay, (red line) excluding the transport delay. Courtesy of [43].

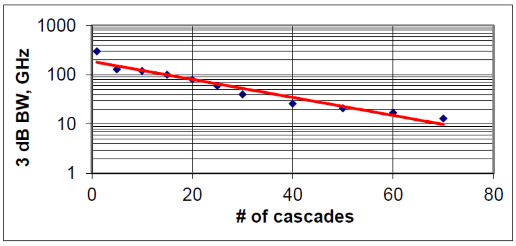

Figure 2.9: QCL bandwidth dependence on the number of cascaded active regions: there is an evident strong linear dependence of the modulation bandwidth on the number of stages of the device. Courtesy of [43].

As a consequence, there is a direct dependence of the QCL 3-dB bandwidth on the number of QCL cascades (Figure 2.9): the higher the number of cascaded periods, the smaller the modulation bandwidth. On the other hand, the higher the number of stages, the higher the output power. Hence, there is a trade-off between the QCL power and the modulation bandwidth. For the typical number of active regions (around 40), the 3-dB bandwidth is limited around 30 GHz. Other studies in literature confirm the limit of the QCL modulation bandwidth to tens of GHz because of either the inverse photon lifetime [44] or the electron extraction time, related to the cascaded structure itself [45].

Method	**Information**	**Global**	**Local**
Laboratory X-ray Diffraction (XRD)	Crystallinity, strain, periodicity average alloy concentration	++	-
Transmission Electron Microscopy (TEM)	Nanostructure morphology, layer thickness, crystallinity, interface quality	-	++
Atom Probe Tomography (APT)	Nanostructure morphology, 3D alloy concentration	-	++
Scanning Electron Microscopy (SEM)	Microstructure morphology, size, roughness	+	+
Secondary Ion Mass Spectroscopy (SIMS)	1D alloy composition	++	-

Table 2.1: Summary of methods used for material characterization of the active region. Legend: ++: highly capable, +: capable with limitations, -: incapable. Courtesy of [46].

2.4 Device properties and characterization

In order to shorten the optimization cycle, it is always suggested to characterize each step of the device's fabrication process separately from the others. However, this proves difficult for QCLs. Hence, the need for very careful and precise measurements in terms of the various spectral and electrical characteristics of the final laser device.

We can perform a pulse mode characterization, as well as continuous wave measurements. The former employs relatively short (50-100 ns) electrical pulses with a low (1-2%) duty cycle to remove the effects of self-heating from the characteristics. The latter allows to achieve much better accuracies, especially in terms of current and voltage measurements; nevertheless, in most cases the temperature is not well defined, because self-heating effects are non-negligible. Table 2.1 summarizes the main characterization techniques covering both global and local resolution.

2.5 Technology

This section is intended to provide some information on the fabrication process of QCLs, as well as the choice in terms of semiconductor materials for their practical realization.

2.5.1 Fabrication steps

The fabrication process includes all the necessary operations from the commercially available supply materials (like semiconductor substrate) and a ready-to-use device.

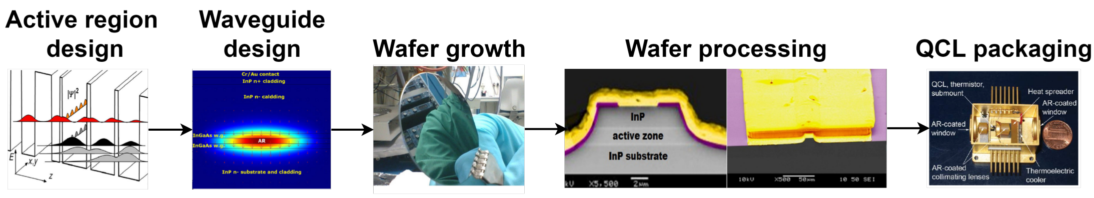

Figure 2.10: QCL device production cycle: active region design, waveguide design, QCL wafer growth, laser chip mounting [47]. Courtesy of [48].

Figure 2.10 represents the main fabrication steps:

1. Active region design: it consists in tuning the intersubband transition energy to the target application wavelength and in optimizing the overall laser efficiency.

2. Waveguide design: the layers surrounding the active region are designed in the way to maximize the overlap of the optical mode with the active region layers and to avoid the overlap of the optical mode with the metallic contact at the surface of the laser ridge.

3. Wafer growth: it involves the growth of the active region in the form of an epitaxial heterostructure, since it is made up of thousands of layers with a high crystalline and chemical purity, along with a very high control of the layer thickness. Two key techniques are used to grow QCLs:

   (a) molecular beam epitaxy (MBE): it is a thin-film deposition technique allowing the fabrication of films of exceptional crystalline quality in a ultra-high vacuum (UHV) environment.

   (b) metalorganic vapor phase epitaxy (MOCVD): the epitaxial growth is achieved through thermal decomposition of precursors of III and V elements, as well as of the dopant species, on the single crystalline substrate.

4. Wafer processing: it includes all the processes made to the sample wafer before it is cleaved into individual functional chips:

   (a) litography: it defines stripes of a photoresist (or a dielectric) on the wafer surface;

   (b) etching of the semiconductor material aside the mask stripes to define the laser waveguide ridge;

(c) electrical insulation of the sidewall of the etched ridges and the are between them;

(d) evaporation of extended metal contacts on the top of the ridges and the back contact on the back of the substrate.

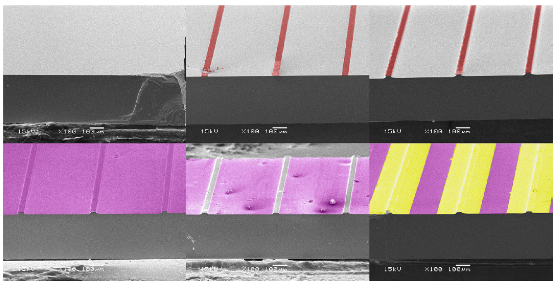

Figure 2.11: SEM image of a cleaved edge of a QCL wafer on different stages of processing. Top panel: (left) Wafer cleave before the processing start; (middle) photoresist mask is fabricated; (right) semiconductor is etched away aside of the mask all the way through the epilayers down to the substrate. Bottom panel: (left) the wafer is over-coated with SiO_2 insulating layer; (middle) windows in SiO_2 layer are made on the top of the etched ridges; (right) extended Cr/Au contacts are evaporated on each laer ridge. Courtesy of [48].

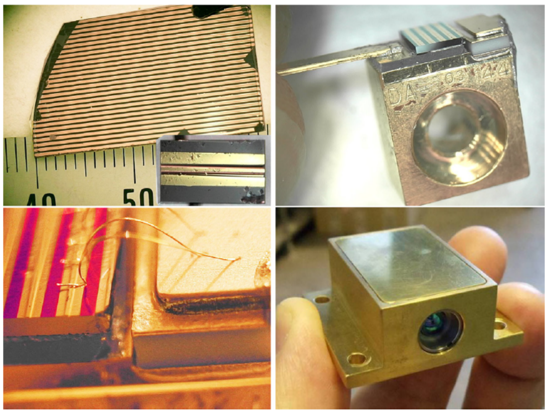

Figure 2.12: SEM image of a QCL chip containing a single laser resonator stripe. The chip is soldered with laser-resonator-side down to a highly thermally conductive AlN ceramic for a better heat extraction. Gold contact metalization of the chip (yellow), SiO2 electrical insulation layer (purple), and the AuSn solder (gyan) on AlN ceramic are colored for clarity. Arrows illustrate the electrical current flow when connected to a current source. Courtesy of [48].

5. QCL packaging: it implies all the processes made with individual laser chips and provide a mechanical hold, heat sinking, electrical contacting, and environmental protection.

The fabrication steps are further differentiated according to the application. As an instance, the chip has a different length depending on its application. For example, DFB QCLs are usually cleaved into 1-2 mm long stripes, while high-power FP QCLs are usually 4 mm or longer. In fact, many applications, especially in the field of sensing, require narrow-linewidth, tunable semiconductor lasers in the MIR range to achieve high sensitivity and selectivity for the detection operation. In order to provide the required narrow-band emission, however, a simple FP type resonator is not sufficient, since the FP modes are too close. This is the cause for the lasers operating in multiple modes under ordinary conditions. The typical 1-3 mm long cavity leads to a FP mode spacing on the order of cm^{-1}.

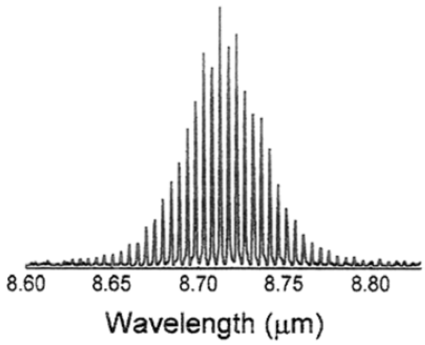

Figure 2.13: Characteristic FP type emission spectrum of a QCL operated in pulsed mode. Courtesy of [49].

By incorporating a grating in a QCL structure, a secondary feedback within the laser cavity is created. This feedback, due to the repeated scattering from the Bragg grating, favors one wavelength, referred as the Bragg wavelength, since it is defined by the grating period rather than the waveguide length. These lasers are known as distributed feedback lasers (DFB). DFB QCLs were first demonstrated in 1997 [50], [51].
There are two ways to introduce gratings into the QCL waveguides [52]: a surface grating in the highly-doped cap layer [50]; a buried grating close to the active region, sandwiched between the waveguide core and the top cladding layers [51]. The surface grating is easier and cheaper, whereas the buried grating leads to more compact devices. The first room-temperature CW DFB QCL was demonstrated in 2005 [53] using the buried grating structure, regarded as the only possibility to produce room-temperature CW QCLs, because of their reduced losses. However, a revision in the design principle of the surface grating geometry [54] allowed

the demonstration of room-temperature CW QCLs based on the surface grating structure.

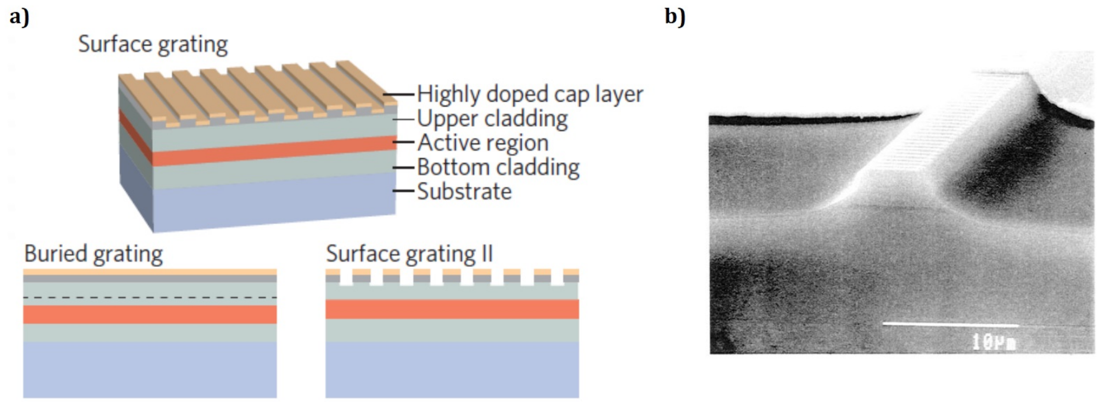

Figure 2.14: (a) Schematics of DFB QCL structures: (top) surface grating; (bottom left) buried grating; (bottom right) revisited surface grating. Courtesy of [52]. (b) SEM image of a portion of a DFB QCL featuring a surface grating. The cleaved mirror section of the deep-etched laser stripe is shown. In the background, the top metallization pad is visible. The grating period of this $\lambda \sim 5.3\mu m$ wavelength DFB QCL is 850 nm. Courtesy of [49].

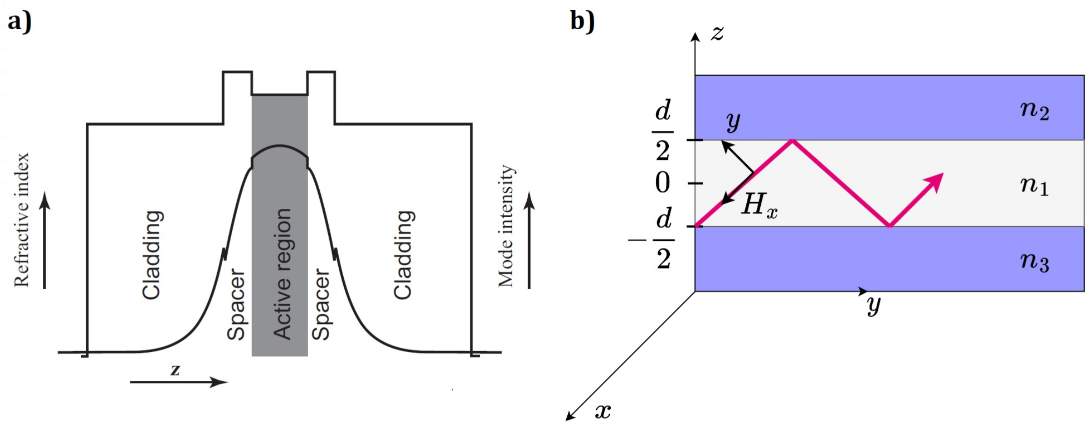

Figure 2.15: (a) Refractive index profile of a typical QCL waveguide, in the growth direction z. The electric field intensity of the fundamental TM mode is also shown. Courtesy of [38]. (b) Schematic drawing of a slab dielectric waveguide, showing the axis, as well as the E and H fields for a TM polarized wave.

2.5.2 The waveguide design

An overlook on the waveguide design is interesting since it is a crucial step to obtain high-performance QCLs.
In a QCL, the light is confined both vertically, by the sequence of the epitaxial layers, as well as horizontally, by the ridge structure that also confines laterally the current. However, the confinement is stronger along the vertical direction, since the epitaxial growth allows for a tigher control, thanks to the layers' thicknesses. In effect, the QCL is an edge-emitting structure: it consists of a core waveguide made of the active region and spacers layers, surrounded by optical cladding layers made of low-refractive index material. As represented in Figure 2.15b, the simplest waveguide for a QCL implementation is a slab of dielectric material (core), sandwiched between two semi-infinite lower-index cladding layers (cladding), satisfying the condition $n_1 > (n_2, n_3)$. Typically, the guiding medium is homogeneous, and its thickness is of the order of a wavelength.
If we consider the propagation of a monochromatic radiation of frequency ω following Maxwell's equation for a dielectric, and if we assume the refractive index is constant in each layer, the solution can be constructed using plane-waves propagating in the z-y plane. The phase factor is also assumed to be common to all layers. Hence, we have:

$$E = E_m \exp\left(-ik_z z\right) \exp\left(\omega t - \beta_m y\right) \qquad H = H_m \exp\left(-ik_z z\right) \exp\left(\omega t - \beta_m y\right) \tag{2.19}$$

where β_m is the propagation constant of the mode with index m. The wavevector in the z direction is then given by solving the equation:

$$\beta^2 + k_z^2 = \frac{\omega^2 n_i^2}{c^2} \tag{2.20}$$

In particular, the following condition must be met for β values:

$$(k_0 n_2, k_0 n_3) < \beta < k_0 n_1$$

since k_z is real in the guiding layer and imaginary in the claddings.
Theoretically, two polarization directions are possible: either transverse electric (TE) or transverse magnetic (TM), in which the electric field or magnetic field respectively is oriented along the y-direction. However, the polarization selection rule of intersubband transitions allows gain for TM mode only. In fact, from the transition rate equation, it is easy to derive that intersubband transitions are coupled to TM mode only, since it is essential to have an electric field that is perpendicular to the direction growth (z). This is due to the fact that only the z-component of the electric field appears in the just-mentioned transition rate equation. Consequently, the only dipole matrix element which is non-null is along

the direction growth.
The TM mode ensures not only the continuity of H_x and E_y fields at the interfaces; in addition, the boundary conditions for the $\mathbf{H}$ field of the TM wave corresponds to the continuity of $n_i^2 E_z, \frac{\partial E_z}{\partial z}$. This translates also with the continuity of the displacement field $D = \epsilon E$.
Yet, the TM mode is less confined than the TE mode, since $n_1 > (n_2, n_3)$, and the boundary conditions force a lower value for $|\mathbf{E}|$ in the active medium. Figure 2.15a depicts the electric field intensity of the fundamental TM mode of the waveguide. Under the light of these considerations, the overlap factor Γ becomes an essential parameter to define and optimize: In other words, Γ is the percentage of the mode interacting with the active region. From the threshold condition, Γ increases by incresing the number of periods in the active zone. In the meantime, the threshold reduces. However, this implies an increase of the total dissipated power injected into the device, because of the increase of the applied voltage. Consequently, in order to minimize the power consumption, proper choices in terms of semiconductor materials used for the QCL realization must be carefully made. Specially, waveguides minimizing the optical losses and maximizing the overlap factor must be implemented.

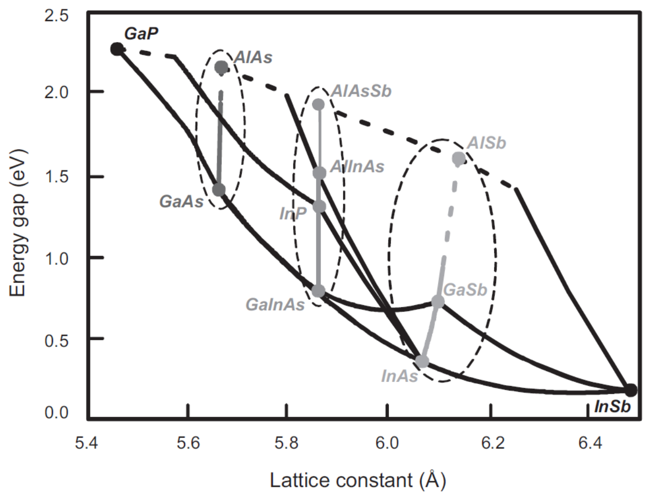

Figure 2.16: The different III-V material systems, as defined by their lattice constants. Their heterostructures that have been already used to realize QCLs are indicated by dashed ovals. Courtesy of [38].

2.5.3 Semiconductor materials

A broad investigation on the most suitable semiconductor materials for QCLs fabrication has revealed significant for the implementation of high-performance devices.

In fact, the device characteristics are profoundly determined by material-dependent properties. The III-V materials have been intensely exploited from the first QCL implementation in 1994 [26]; nevertheless, recent studies [19] [55] have confirmed the possibility of Si-based QCLs.
The first QCL in 1994 [26] used InAlAs as the cladding layers due to its low refractive index of around 3.20. The core region, which includes active and injector regions, usually has 500 stacking layers consisting of alternative InGaAs and InAlAs layers with total thickness of about 1.5–2.5 μm and refractive index of about 3.35 [49]. This lattice matched structure was grown on InP.
In later designs, the InAlAs cladding layers were replaced by InP because it has a lower refractive index of around 3.10 and a higher thermal conductivity for better heat treatment, which is a critical step for the device performance [49].

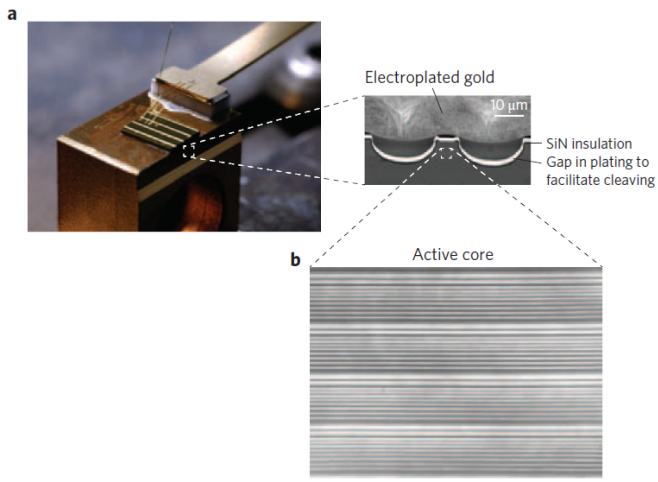

Figure 2.17: a. (left) Photograph of a laser bar with four QCLs (courtesy of Frank Wojciechowski). (right) SEM image of the front facet of a QCL. b. High-resolution TEM image of a QCL, showing four periods of active regions and injectors. Electron transport is top to bottom. InGaAs layers are shown in light grey, AlInAs layers in dark grey. Courtesy of [52].

At the moment, InP-based systems provide the best waveguide properties for MIR QCLs, since InP can be used as cladding material because of its several advantages:

- low refractive index and good electrical properties make InP provide excellent optical confinement without the need of high doping concentration, with subsequent low free-carrier optical losses.
- It is the only binary material that can be used as cladding, possessing a

thermal conductivity (0.7 W/cm/K) almost twice that of GaAs and at least 10 times higher than the ternary or quaternary alloys.

- InP-based systems cover the spectrum from 3.6 to 24 µm. Yet, standard InP systems fail to produce high-performance QCL below 6 µm. However, its spectral range can be extended toward short wavelengths by using strained compensated materials, with increased concentration of both In in InGaAs wells and Al in InAlAs barriers.

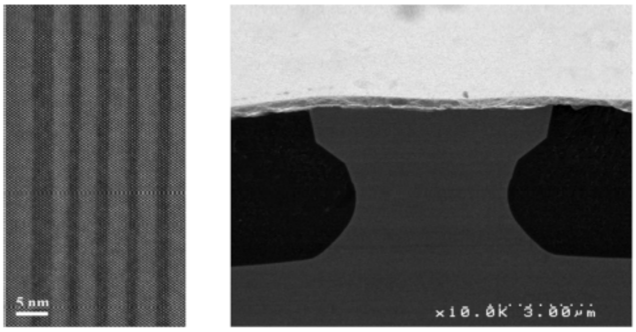

Figure 2.18: (left) TEM image of an InAs/AlSb based QCL structure. Dark zones correspond to AlSb. (right) Optical microscope photograph of a cleaved facet of an InAs/AlSb QCL planarized with hard baked photoresist. Courtesy of [56].

Valid options to InP-based devices are GaAs-based QCLs [57], ranging now from 8 µm to 160 µm. GaAs cannot be used as a cladding, though, since the substrate index is higher than that of the active regions. Alternative materials have been proposed, simply transposing to the MIR range the choices made for the NIR diode lasers: AlGaAs or GaInP as cladding layers.
Besides, GaAs presents a relatively high threshold at room temperature with respect to InP ($J_{th}^{GaAs} \sim 5J_{th}^{InP}$), which makes CW operation almost impossible for these devices above 200 K.
On the other hand, GaAs becomes better performing than InP for the long-wavelength range, especially for reasons of material purity; in effect, it dramatically increases the mobility and the conductivity of the semiconductor at low temperature and guarantee low waveguide losses, enabling the development of the Terahertz QCL [58].
So far, the emission wavelength of QCLs has been extended from the near infrared (around 100 THz) to terahertz regimes. While the longest demonstrated wavelength is 1.6–1.8 THz with GaAs/$Al_{0.1}Ga_{0.9}As$ system at 80 K under continuous-wave (CW) operation [59], the shortest wavelength has been extended to 2.6 µm with InAs-based QCLs [60]. In fact, GaAs-based QCLs cannot operate below 8 µm [61]

[56]. Though, this material family is well suited for THz QCLs.
InAs and AlSb present the most recent material system used for QCL fabrication. InAs/AlSb QCLs are often referred to as InAs-based or antimonide lasers. They have brought significant progress in short wavelength QCLs due to the high-conduction band offset.
A possible alternative to the most spread dielectric waveguides is the plasmon-enhanced waveguide, introduced for the first time by Sirtori and co-workers in 1995 [62]. This kind of waveguides differs from dielectric waveguides since the cladding layers are highly doped. In order to achieve a low refractive index, the strong dispersion of the doped material is exploited; indeed, the dispersion occurs when the laser frequency approaches the plasma frequency. Efficient implementations have been then completed with GaAs-based structures [63], but not without any drawback. In fact, highly-doped materials imply high optical losses; thick, low-doped spacers are needed to separate the active region from the highly doped layers, thus reducing the overlap factor.

2.5.4 Silicon Integration

Along the years, Silicon photonics' research mainly focused on the fabrication of devices in the telecommunication bands around 1310 nm and 1550 nm. This direction was driven chiefly by the market request and the low costs due to the manipulation of complementary metal-oxide-semiconductor (CMOS) infrastructures. One of the main advantage of Si is indeed the cost reduction deriving from the reusability of already-existing infrastructures, as well as the compatibility with integrated Si electronics systems. Moreover, it also provides for further physical advantages with respect to other materials, such as InP, GaAs and chalcogenide glasses [64].
As concerns the realization of adequate light sources, Si can be adopted as the active region medium; deposition-compatible dielectric materials like silicon dioxide (SiO_2) or silicon nitride (Si_3N_4) can act as a cladding. This allows for the realization of an optimal waveguide, where the light is efficiently confined thanks to the high-refractive index contrast.
Yet, the Si is an indirect gap material: in order to use Si to generate light, enhancing the efficiency of emission, heterogeneously integrated III-V/Si devices can be manufactured [65]. Photonics integrated circuits (PICs) have been demonstrated in the NIR [66].
Though, the MIR range is sparking more interest, especially for sensing, military and medical applications. Up to now, few PICs have been constructed for operation in the MIR [67], [68]; furthermore, heterogeneous integration has enabled detectors up to 3.8 µm [67], [69] and lasers up to 4.8 µm [19]. In effect, there are many issues to face to enable efficient heterogeneous integration for wavelengths in the 2-20 µm

range. While in the NIR Si, SiO_2 and Si_3N_4 have low optical material losses, in the MIR the material absorption of Si and SiO_2 limits the wavelength range of Silicon-on-Insulator waveguides.
Despite these obstacles, recent studies succeeded in integrating on Si lasers operating at 2 µm [70] and 4.8 µm [19].

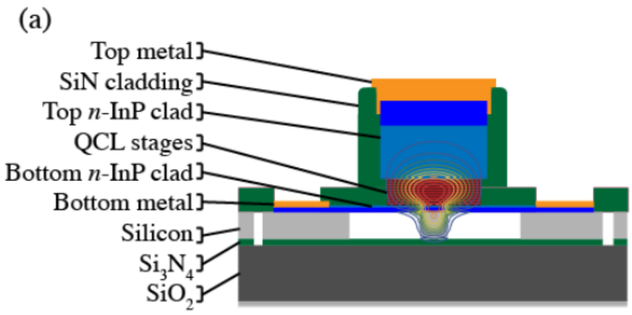

Figure 2.19: A cross-sectional schematic of the active region of a heterogeneously integrated 30 stage, $\lambda \approx 4.8$µm QCL above a fully etched Si waveguide. A contour plot of the electric field component $|E_y|$ of the fundamental TM mode is overlaid. Courtesy of [55].

This last achievement was possible thanks to the integration of a Fabry-Perot (FP) QCL heterostructure on a broadband Silicon-on-Nitride-on-Insulator (SONOI) waveguide platform (Figure 2.19). This 30-stage FP laser emits 31 mW into Si waveguides, and operates in pulsed mode up to 60°C.
Distributed-feedback (DFB) lasers have also been demonstrated [55]. Wavelength-selective feedback elements have been already integrated in the NIR [71]. The same photolitographic technique can be applied to Bragg-reflectors in the MIR with less troubles, as the grating pitch scales with wavelength. Therefore, a DFB QCL operating in pulsed mode up to 100°C and emitting > 200 mW has been fabricated. Although design and fabrication modifications are necessary to improve the III-V taper transmission and to achieve continuous-wave (CW) operation, these lasers are suitable for integration in PICs.
A major challenge consists in the integration of lasers with wavelengths higher than 7 µm: SOI and SONOI platforms are unlikely to provide hybrid waveguides with sufficiently low loss to support lasing. Nevertheless, integration can be still practically possible using an alternative platform based on Ge or $GeSi_x$ waveguides. Ge-on-Si (GOS) or Ge-on-SOI (GOSOI) waveguides can guide light from 1.9 µm to above 10 µm (Figure 2.20a). Finally, heterogeneous integration allows multiple lasers operating at different wavelengths (from 3 to 6.7 µm) to be integrated on one chip, enabling the so-called spectral beam combining (Figure 2.20b).

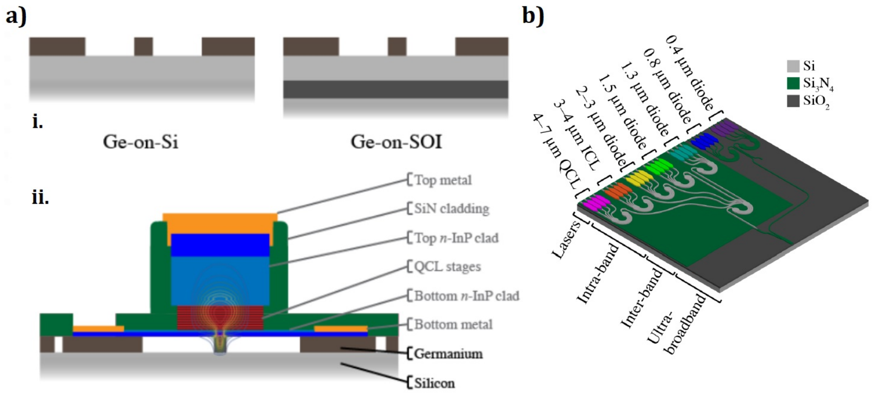

Figure 2.20: (a) i. Cross-sectional schematic of GOS and GOSOI waveguide platforms. ii. Cross-sectional schematic and fundamental TM optical mode simulation of a QCL bonded on GOS waveguide (confinement with the active region of $\Gamma \approx 0.77$). (b) Multi-spectral laser architecture with multiple gain materials bonded onto a Si substrate. Each laser is spectrally combined in multiple stages to a single output waveguide. Courtesy of [55].

2.6 QCL applications

QCLs operate in a very large frequency range, in high temperature conditions and can be modulated with very high frequency. These features drove the QCLs' application's fields; the latter, in turn, is conditioning the research in the development of either high-power and high-wallplug-efficiency devices for countermeasure systems and high-frequency modulation for telecommunication devices.

2.6.1 Telecommunications

Free-space optics is a promising approach for the development of rapidly deployable, cost-effective and secure communication links. In contrast to fiber-optics, this technique does not require an apposite cables installation, leading to cost efficiency. In addition, in urban areas where large amounts of fiber connections exist, fast FSO datalinks could be convenient to momentarily increase the bandwidth between two points. Finally, FSO can be employed to create high-bandwidth access in countries where very little ground infrastructure exists or to connect mobile phone antennae to the fiber backbone.
Several approaches exist for imprinting the data onto the laser beam: it is possible to modulate the amplitude, the frequency, the phase and the polarization. Initial experiments have demonstrated modulation frequencies in the MHz range using first cryogenically cooled [72] [73] and then Peltier-cooled lasers and detectors

[74]. Nowadays, QCLs can be directly modulated at speeds of several tens of GHz, with no spectral distortion caused by the relaxation oscillation resonance and with negligible chirp [75].

2.6.2 Gas sensing

Laser remote sensing techniques have proved to be capable of providing powerful instruments for atmospheric research and environmental monitoring [76]. Many important trace gases, from byproducts of fossil fuel burning to constituents of human breath, have absorption features in the MIR range (4 µm - 12 µm [77]) as a result of molecular rotational-vibrational transitions [49]. Different laser sources have been demonstrated for spectroscopic measurements, but QCLs can operate in a very large wavelength range (2.9 µm - 250 µm Figure 2.21), with the advantage of the exploitation of a compact and high-power device.

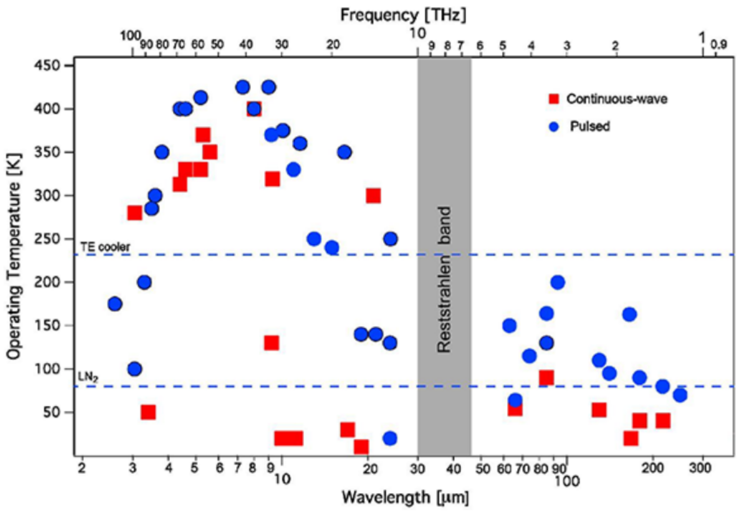

Figure 2.21: Operating temperature plot as a function of the emission wavelength/frequency for QCLs. Courtesy of [78].

2.6.3 Target illuminators and infrared countermeasures

Directional infrared countermeasure (DIRCM) is a self-protection airborne system used to safeguard aircraft from the impact of heat-seeking missiles, particularly from Man Portable Air Defence Systems (MANPADS) missile attacks. The system helps detect incoming threats during the missile launch and countermeasure missile guidance using a directed laser beam that deviates its trajectory. Being quick and automatic, the DIRCM system can react against attacks of any imaging infrared seeker with a jamming sequence that facilitates successful countermeasure.

2.6.4 Mid-Ifrared Laser Detection And Ranging (LADAR)

Radio Detection And Ranging (RADAR) is the process of transmitting, receiving, detecting and processing an electromagnetic wave that reflects from a target. Laser-based RADAR (or LADAR) uses laser frequencies rather than radio frequencies to transmit and detect signals Figure 2.22. One of the LADAR implementation utilizes QCL frequency modulation to conduct FM ranging: the time lag between transmission and reception is converted to a frequency difference (Figure 2.23). By measuring the frequency difference, the time lag and the range can be determined.

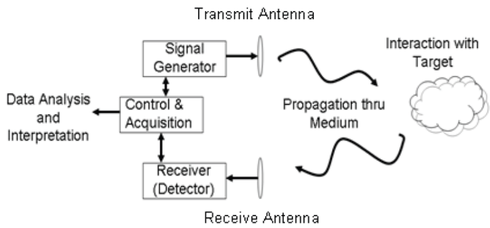

Figure 2.22: Typical LADAR system. Courtesy of [79].

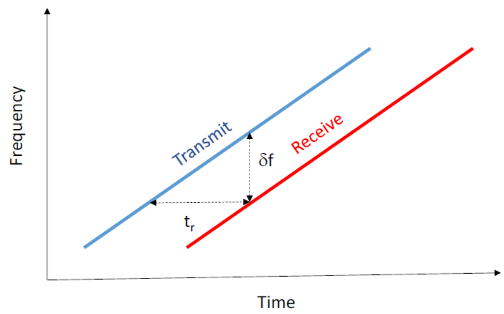

Figure 2.23: Linear frequency modulation ranging. Courtesy of [43].

Chapter 3

Chaos theory

3.1 Introduction

Chaos theory came up in the latter half of the 20th century as a new approach to science: many have heard of it; few truly understand it, though.
"Does the flap of a butterfly's wings in Brazil set off a tornado in Texas?": Ed Lorenz, the father of chaos theory [80], inquired in the 1960s. This provocative question has now become very familiar to our ears; nevertheless, it broke forth during a period full of great hopes in science and its potentialities. This optimism was also reinforced by the advent of computers, executing operations impossible for the human being.
And it was the finite computational precision of a machine's simulation to endorse Lorenz skepticism: as a long-range weather forecaster, he discovered that even small differences in the initial conditions can lead to vastly different outcomes. This is the counter-intuitive concept at the base of the Butterfly Effect.
Even if chaos theory was firstly revealed in climate change, chaotic patterns were immediately and concurrently recognized in a variety of more or less complex dynamic systems: from economy to biology, to astronomy, chaos theory revealed that an apparent random behavior is essentially impossible to predict.
Imagine a water faucet being gradually turned on: from a fairly smoothly flow, turbulence is created, appearing as random fluctuations. This turbulence must be controlled by a variety of simple factors: the speed of flow, the shape of the tap, the volume of water, and the pressure of the water system. Despite looking like a simple system, it rapidly becomes unpredictable. However, in rare instances, when all the system variables assume specific values, a temporary order is produced: there is order within the chaos [81].

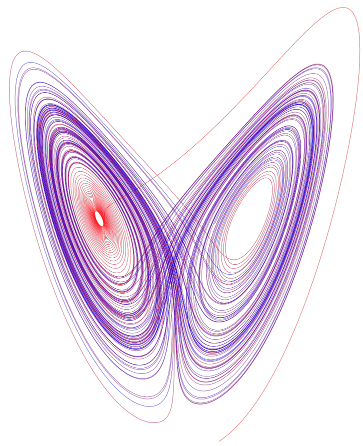

Figure 3.1: Lorenz attractor: trace starts in red and fades to blue as time progresses. Courtesy of [82].

It is possible to represent chaos in an infinite-variable space, namely the phase space. Here, self-completing spiral patterns, called strange attractors, emerge. Figure 3.1 represents the most iconic one: the Lorenz attractor.

3.2 The Lorenz model

The faith in the possibility that early room-sized supercomputers could yield accurate weather forecast held sway over Lorenz mind: in his clumsy machine, he entered a streamlined computational model consisting of 12 meteorological calculations. The equations analyzed basic variables, like temperature, pressure, wind speed, and spit out a simulated weather forecast.
However, in 1963 [83], the MIT researcher oversimplified the complex behavior of Earth's atmosphere to a single atmospheric condition known as rolling fluid convection (Figure 3.2). It can occur either on large scales or smaller scales, like in a cup of hot coffee.

This atmospheric flow was modeled by a set of three nonlinear differential equations:

$$\frac{dx(t)}{dt} = \sigma(x(t) - y(t)) \tag{3.1}$$

$$\frac{dy(t)}{dt} = \rho x(t) - y(t) - x(t)z(t) \tag{3.2}$$

$$\frac{dz(t)}{dt} = -\beta z(t) + x(t)y(t) \tag{3.3}$$

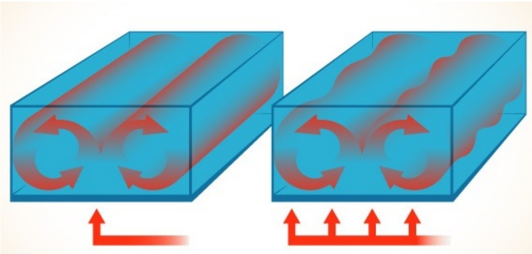

Figure 3.2: The convection process: (left) when a liquid or gas is heated from below, the fluid tends to organize itself into cylindrical rolls. Hot fluid rises on one side, loses heat, and descends on the other side. (right) When the heat is turned up further, an instability sets in, and the rolls develop a wobble that moves back and forth along the length of the cylinders. At even higher temperatures the flow becomes wild and turbulent. Courtesy of [81].

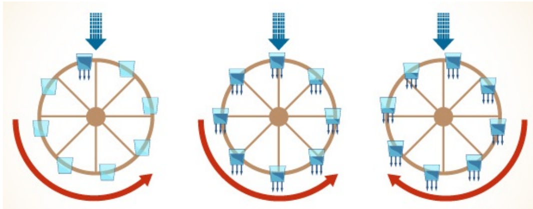

Figure 3.3: The waterwheel is the first, famous chaotic system discovered by Lorenz. Water pours in from the top at a steady state. If the flow of water is slow, the wheel never starts turning because friction is not overcome, since the top bucket never fills up enough. If the flow is faster, the weight of the top bucket sets the wheel in motion (left). The waterwheel can settle into a rotation that continues at a steady state (center). If the flow is faster still (right), the spin can become chaotic. Courtesy of [81].

where x(t), y(t) and z(t) are respectively the circulatory fluid flow velocity, the temperature difference between rising and falling fluid regions, and distortion of vertical temperature profile. σ, ρ, β represent instead the ratio of fluid viscosity to thermal conductivity, the difference in temperature between the top and bottom of the system and the ratio of box width to box height. Lorenz supercomputer could easily simulate this computational model, allowing also for the data visualization in a three-dimensional space, namely the phase space. The computer drew what was destined thereafter to be recognized as the Lorenz attractor: a curve with two overlapping spirals resembling butterfly wings. The line making up the curve never intersected itself and never retraced its own path. Instead, it looped around forever and ever, sometimes spending time on one wing before switching to the other side. It was a picture of chaos, and while it showed randomness and unpredictability, it also showed a strange kind of order. This new discovery laid the roots for the birth of a new physics, the deterministic chaos.

3.3 Deterministic chaos

The expression "deterministic chaos" may appear an oxymoron: actually, it points up the deterministic origin of chaotic phenomena. Clearly, chaotic outcomes cannot be exhibited by whatever system: only nonlinear systems described by three variables can display irregular variations of systems' outputs. In other words, the system evolves in a deterministic way, and the current state of the system depends on the previous state in a rigidly deterministic way; nevertheless, the systems' output shows random variations. In fact, it is not possible to foresee the future of the output, since chaos' strong dependence on initial conditions.
This is in contrast with random or stochastic processes, where a certain indeterminacy can be singled out because of the probabilistic evolution on the initial states. Notably, some form of nonlinearity is required for the realization of chaotic dynamics. Nonlinear systems can be observed in various fields, from engineering to economics. Though this diversity, similar chaotic dynamics can be manifested by such systems; hence, similar differential equations and same mathematical tools can be applied for their analysis.

3.4 Nonlinear chaotic systems: logistic maps and bifurcation diagrams

Lorenz had to struggle in the 1960s to make room for revolutionary new ideas in the world of science, which was little open to the possibility of a new approach to physics and life. A few years later, in the 1970s, however, scientist Robert May arrived at similar conclusions to Lorenz's in a totally different field: population biology. He used mathematical techniques to model how animal populations might change over time, given a certain set of starting conditions. Conclusively, the logistic difference equation he came up with enabled him to predict animal populations reasonably well [84]:

$$x_{n+1} \; = \; rx_n(1 - x_n) \tag{3.4}$$

where r is the driving parameter, factor causing the population to change. x_n is the population of the species, instead. By fixing an initial value for r and x, the equation is iterated, to see how the population evolves along time. However, unexpected and confounding results were obtained, according to the initial value assigned to r. As far as r stays less than 3, x_n converges to a fixed point. If r is exactly 3, the output oscillates between two values. On a map or diagram, this appears as a single line dividing into two branches: a bifurcation. Taking r value even higher, x experiences period-doubling oscillatory solutions, reaching finally irregular chaotic oscillations. This is the so-called period-doubling bifurcation, but it is not the only route to chaos: quasi-periodic-doubling bifurcations and intermittent chaotic bifurcations [85] have been demonstrated too.

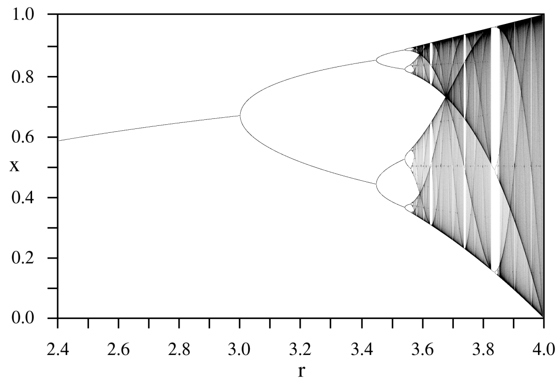

Figure 3.4: A bifurcation diagram for the logistic mapping.

Though, by examining Figure 3.4, there is a glimpse of order and patterns repetition: by zooming in on consecutive doubling points, the large-scale structure repeats itself multiple times. This is precisely the definition of self-similarity: it is a property of a class of geometric objects known as fractals, coined by mathematician Mandelbrot during the '70s [86]. Together with self-similarity, fractals are characterized by the fractal dimension, an indicator of their complexity. However, this number is not an integer, but a fraction.

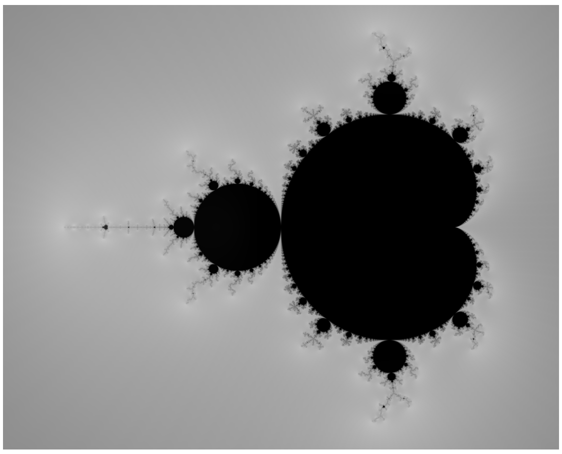

Figure 3.5: Mandelbrot set.

Today, fractals are infinitely complex objects self-similar across all scales, well representing nonlinear dynamical systems. In fact, Mandelbrot eventually proved that Lorenz's attractor was a fractal, as are most strange attractors.

3.5 Characterization of chaos

In order to distinguish chaotic timetraces from stochastic ones, tools for the chaos characterization must be proposed. Typically, chaos is measured by Lyapunov exponents (LEs) and a Lyapunov dimension.
The Lyapunov exponent measures the rate at which two originally nearby trajectories diverge in time; in fact, two close trajectories are supposed to exponentially diverge in the presence of chaos. The definition of the Lyapunov exponent of the logistic equation is the absolute value of the slope of the logistic map:

$$\lambda \;=\; \lim_{n\to\infty} \frac{1}{n} \sum_{0<k<n-1} \ln |f'(x_k)| \tag{3.5}$$

In other words, the slope of the map determines the degree of dependence on initial conditions. In particular, the largest Lyapunov exponent (LLE) measures chaoticity [87], that is how much a system is sensitive to the initial conditions. In order to exhibit chaos, at least one LE must be positive [88]. Adversely, zero or negative LEs indicate convergence of nearby points.
The calculation of LEs from experimental time series is complex and several techniques have been introduced [89]; generally, the number of LEs is related to the number of system variables. However, the computation can be simplified by evaluating the LLE only.
In order to measure the complexity (strangeness) [90] of an attractor, the attractor dimension or Lyapunov dimension must be estimated. This is performed through the Kaplan-Yorke dimension (KYD) [91], evaluating the amount of information required to locate the system in the phase space.
Alternatively, the Kolmogorov-Sinaï entropy (KSE) [92] estimates the average loss of information rate. An upper bound for the KSE is provided by the Persin inequality [93], which takes the sum of all the LEs above zero:

$$KSE \;\leq\; \sum_{k|\lambda_k>0} \lambda_k \tag{3.6}$$

The KSE takes an infinite value for perfectly random systems. In case of chaotic systems, instead, it assumes a positive value. The larger its value, the larger the entropy and the unpredictability of the system.
Finally, the negative sum of all the LEs represents damping

$$\alpha \;=\; -\sum \lambda_k$$

that is the dissipation of energy from oscillations [94].
The attractor dimension can be useful for chaos classification into dissipative or conservative. If a system is an n-th order one, chaos is defined to be conservative

if the attractor dimension is exactly equal to n. In this condition, α=0 [95]. By contrast, if the attractor dimension is smaller than n, then the system is said to be dissipative. Dissipative chaos appears to be the majority.

3.6 Nonlinear optical systems: lasers and their route to chaos

Nonlinear systems can be found in optics too, since many optical materials and devices prove nonlinear response to the optical field. Lasers are themselves nonlinear systems and are typically characterized by three variables: field, polarization of matter and population inversion. Indeed, in 1975 Haken [96] demonstrated the nonlinear nature of lasers, coming up with rate equations very similar to Lorenz's ones. Thereafter, the Lorenz-Haken equations (after their contributor, Haken) are the model used for the description of lasers' chaotic dynamics.

$$\frac{dx(t)}{dt} = \sigma(x(t) - y(t)) \tag{3.7}$$

$$\frac{dy(t)}{dt} = \rho x(t) - (1 - i\delta)y(t) - x(t)z(t) \tag{3.8}$$

$$\frac{dz(t)}{dt} = -\beta z(t) + Re[x^*(t)y(t)] \tag{3.9}$$

where $\sigma = T_2/2T_{ph}$, $\beta = T_2/T_1$ and $\rho = w_0 c T_{ph}/\eta$. In turns, T_{ph} is the photon lifetime, T_1 the population inversion (longitudinal relaxation) and T_2 the polarization (transverse relaxation). Moreover, η is the refractive index of the laser medium, w_0 the population inversion induced by the pump at the laser threshold and $\delta = (\omega_0 - \omega_A)T_2$ is the scaled atomic detuning, being ω_0 the angular oscillation frequency and $\omega_A = \omega_2 - \omega_1$ the angular frequency of light emitted or absorbed in the two-level system used in the laser model.
However, not all the lasers exhibit chaotic behavior. Chaotic oscillations of infrared gas lasers in experiments were reported for Xe lasers [97], He-Ne lasers [98] and NH_3 lasers [99]. On the contrary, semiconductor lasers are intrinsically stable lasers. However, they are described by the field and the carrier density (population inversion) rate equations; so, they can be easily destabilized by the introduction of an external optical feedback, optical injection, or modulation for accessible laser parameters. In fact, since the early '80s, feedback-induced instabilities and chaos in semiconductor lasers have been extensively examined [100], since the laser oscillation is affected considerably when the light reflected back from an external reflector couples with the original field in the laser cavity. A variety of dynamics, from stable state, to periodic, quasi-periodic and chaotic behaviors can be observed

for the variations of the system parameters, at weak to moderate external optical feedback reflectivity.
As an alternative, modulation for the injection current is a perturbation to the laser, and so a further extra degree of freedom to it. Indeed, chaotic oscillations have been displayed under high frequency modulation, with a large modulation index close to the relaxation frequency of the laser [101].

3.6.1 Classifications of lasers

Lorenz-Haken equations (Equation 3.7-Equation 3.9) model the laser as a ring resonator with two-level atoms. Practically, more appropriate models imply three or four level-atoms, as in the case of QCLs. Thus, some modifications are required, even if the two-level-atoms model's results can be extended to more complicated analysis, as concerns the discussion of instabilities.
The stability and instability of lasers intrinsically involved in laser rate equations are classified according to the scales of time constants for the relaxation oscillations T_{ph}, T_2 and T_1 [102]. Namely, one or two of the time constants among the three in the differential equations may be adiabatically eliminated and one or two of the laser rate equations are enough to describe actual laser operations.
Arecchi and his co-workers [102] provided for an extensive classification of lasers into three classes, specifically class A, class B and class C lasers.
When the time constants of the relaxations (field, population inversion and polarization of matter) are of the same order, all of the Lorenz-Haken differential equations must be considered. These are the class C lasers, and infrared gas lasers and far-infrared lasers [97] [98] [99] are almost classified into class C.
When the time constant T_2 of the polarization of matter is small compared with the other time constants ($T_{ph}, T_1 >> T_2$), the Lorenz-Haken equations for the field and for the population inversion are coupled, and that for the polarization is eliminated [103]. These are class B lasers, naturally stable, but easily destabilized by the addition of an extra degree of freedom, as an external perturbation. The latter allows for the coupling of the field amplitude with the field phase, obtaining again the rate equations coupled with three variables. A laser coupled with three variables becomes a chaotic system and shows instabilities. Examples or class B lasers are CO_2 lasers, where loss modulation provides the additional degree of freedom to achieve chaotic trajectories [104].
One typical feature of class B lasers is a relaxation oscillation of the laser output, observed for a step-time response when $T_1 > T_{ph}$, that means the population inversion does not follow the photon decay rate. This property explains why some semiconductor lasers are not classified into this family, among which QCLs [105].
Finally, class A lasers are those who need two degrees of freedom to be destabilized. In fact, the differential equations for the polarization and for the population

inversion can be eliminated since the photon lifetime is much larger than the other time constants ($T_{ph} >> T_1, T_2$). Therefore, class A lasers are the most stable ones, and present a high Q-factor. Visible He-Ne lasers, Ar-ion lasers and dye lasers are examples of class A lasers.
As regards QCLs, they are quasi-class A lasers because of the theoretical absence of relaxation oscillations [105]; thus, it is hard to say if they require one or two extra degrees of freedom. As an instance, generating chaos with only feedback is doable, but it is much easier with two different types of perturbation, like feedback and electrical modulation. Another option is that complex nonlinear dynamics can stem from multi-mode beating in the case of a FP laser with specific relationship between the optical modes.

3.7 Chaos in semiconductor lasers

Semiconductor lasers are stable lasers in nature, as largely discussed in the previous sections. In the following, the dynamics of semiconductor lasers with optical feedback will be analyzed, with a focus on the mathematical theory and related outcome in terms of possible lasers' dynamical regimes. Particular attention will be devoted to the QCL case.

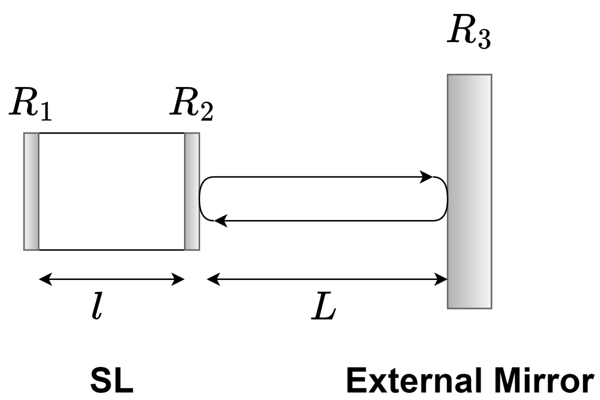

Figure 3.6: Model of semiconductor laser with external optical feedback.

3.7.1 Semiconductor lasers with optical feedback

Optical feedback in SLs gives rise to rich varieties of dynamics; for the past decades, theoretical and experimental results allowed for noticeable studies about the principles, the effects and the outcomes of such an external perturbation.
The main motivations behind the choice of focusing on optical feedback as a way to perturb the lasers is related to the numerous proofs offered along the years; moreover, this is the scheme studied in our experimental work about chaos and private communication in QCLs.
The formalism of a SL under optical feedback was originally proposed by Lang and Kobayashi [100]. In their model, they assumed for simplicity only one round-trip in the external cavity, meaning a small amount of feedback. Under these conditions, the laser's rate equations are:

$$\frac{dE(t)}{dt} = \frac{1}{2}(1-i\alpha)\,G_n\,(N(t)-N_{th})\,E(t)+\frac{k}{\tau_{in}}E\,(t-\tau_{ext})\exp\left(-i\omega_0\tau_{ext}\right) \quad (3.10)$$

$$\frac{dN(t)}{dt} = \frac{I}{q}-\frac{N}{\tau_c}-G(N)|E|^2 \quad (3.11)$$

E is supposed to be the slowly varying envelop of the complex electric field, whereas N is the carrier density of the upper laser state. Then, α is the linewidth enhancement factor (LEF), ω_0 the free-running laser angular frequency, I the bias current, q the electron charge, τ_c the carrier lifetime, τ_p the photon lifetime and N_{th} the carrier density at threshold. As concerns the gain terms, G_n is the differential gain and G(N) the gain per unit time. Above threshold, the gain per unit time is expressed as:

$$G(N) = \frac{1}{\tau_p}+G_n\,(N(t)-N_{th}) \quad (3.12)$$

Coming back to equations Equation 3.10-Equation 3.11, τ_{in} is the internal-cavity round-trip time, whereas τ_{ext} is the external-cavity round-trip time. This last parameter, together with k, takes into account the presence of the external feedback. In fact, k is namely the feedback coefficient. Defining the external coupling coefficient for a FP laser as $C_l = \frac{1-R_2}{2\sqrt{R_2}}$, with R_2 the reflection coefficient of the laser front facet subjected to the reinjection, k is defined as:

$$k = \frac{1}{\tau_{in}}2C_l\sqrt{f_{ext}} \quad (3.13)$$

For a DFB laser, the expression of C_l becomes more complex, depending on the complex reflectivity at both laser facets [106].
It is also possible to separate the field equation into two equations for the amplitude

$E_0(t)$ and the phase $\phi(t)$, writing the complex electric field as $E(t) \ = \ E_0(t)\exp\left(i(\omega_0 t + \phi(t))\right)$ [107]:

$$\begin{aligned} \frac{dE_0(t)}{dt} \ &= \ \frac{1}{2}G_n\left(N(t) - N_{th}\right)E_0(t) \ + 2\frac{k}{\tau_{in}}E_0\left(t - \tau_{ext}\right) \\ &\qquad \cdot \cos\left(\omega_0\tau_{ext} + \phi(t) - \phi(t - \tau_{ext})\right) \end{aligned} \tag{3.14}$$

$$\frac{d\phi(t)}{dt} \ = \ \frac{\alpha}{2}G_n\left(N(t) - N_{th}\right) - \frac{k}{\tau_{in}}\frac{E_0\left(t - \tau_{ext}\right)}{E_0(t)}\sin\left(\omega_0\tau_{ext} + \phi(t) - \phi(t - \tau_{ext})\right) \tag{3.15}$$

Stationary lasing conditions can be obtained from Equation 3.10, by setting E to be constant. Hence, the photon density S_s is constant as well: $S_s \ = \ S_s(t) \ = \ S_s(t - \tau_{ext})$. As a result, the cosine term is time insensitive, obtaining a steady-state phase $\phi_s \ = (\omega_s - \omega_0)t$.
The real and imaginary parts of Equation 3.10, when they are separated, can be written as:

$$G(N) - \frac{1}{\tau_p} + 2\frac{k}{\tau_{in}}\cos\omega_s\tau_{ext} \ = \ 0 \tag{3.16}$$

$$\omega_s - \omega_0 \ = \ -\frac{k}{\tau_{in}}\left[\alpha\cos\omega_s\tau_{ext} + \sin\omega_s\tau_{ext}\right] \tag{3.17}$$

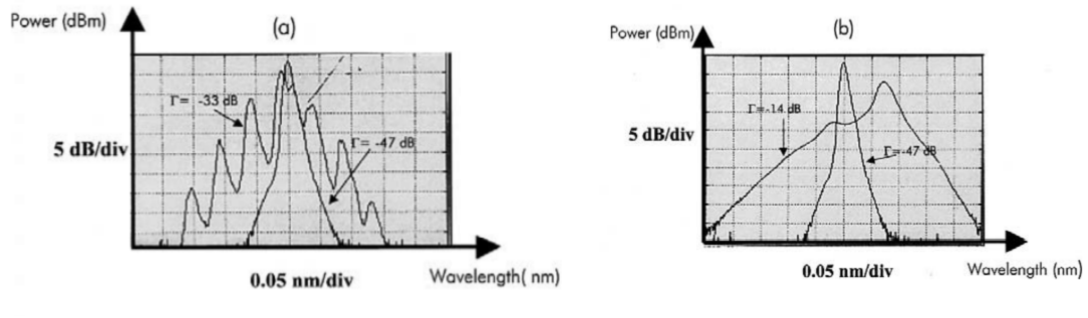

Figure 3.7: Experimental spectra of a 1.3-µm DFB lasers at 10 mW under feedback operation. (a) For Γ = -47 dB and Γ = -33 dB; λ_{peak} = 1303.6 nm. (b) For Γ = -47 dB and Γ = -14 dB (coherence collapse regime); λ_{peak} = 1303.6 nm. Courtesy of [108].

In particular, Equation 3.17 leads to several solutions for ω_s, being the angular frequencies of the external-cavity modes. Among these frequencies, the laser will tend to operate on the mode with minimum linewidth, corresponding to the best phase stability [109]. Therefore, ω_s in Equation 3.16 is the frequency with the

minimum linewidth.
In general, though, the gain is affected by the presence of the optical feedback, and depends on the feedback level: the higher the feedback strength, the lower the threshold current of the laser (Figure 3.8a) and consequently the gain [110].

Figure 3.7 reports the experimental spectra observed when a DFB semiconductor laser, emitting in the NIR window, is operated under external optical feedback. Figure 3.7a highlights a linewidth broadening, turning the laser from single-mode to multimode. As long as the feedback strength is increased, though, a further broadening is exhibited, corresponding to the coherence collapse regime. This is an evident proof of how destabilizing can be the presence of the external optical feedback for the optical properties of a laser. Additional definitions and explanations will be given in the following sections.

Regime	**Feedback strength**	**Features**
I	$<0.01\%$	Very small feedback and small effects. Depending on the feedback fraction, the linewidth becomes broad or narrow.
II	$<0.1\%$	Small, non-negligible effects. Mode-hopping among internal and external modes after the external modes' generation.
III	$\sim 0.1\%$	Narrow region with suppression of‘mode-hopping noise. The laser may oscillate with narrow linewidth.
IV	$\sim 1\%$	Moderate feedback regime. The relaxation oscillations become undamped. The laser's linewidth is highly broadened. The laser shows chaotic behavior, evolving sometimes into unstable oscillations in a coherence-collapse state. Noise is considerably enhanced.
V	$>10\%$	Strong feedback regime. Internal and external cavities behave like a single cavity and the laser oscillates in a single mode. The laser's linewidth is greatly narrowed.

Table 3.1: Summarizing table about the SLs' five regimes' features, based on the studies of [111] [112].

3.7.2 Dynamical regimes

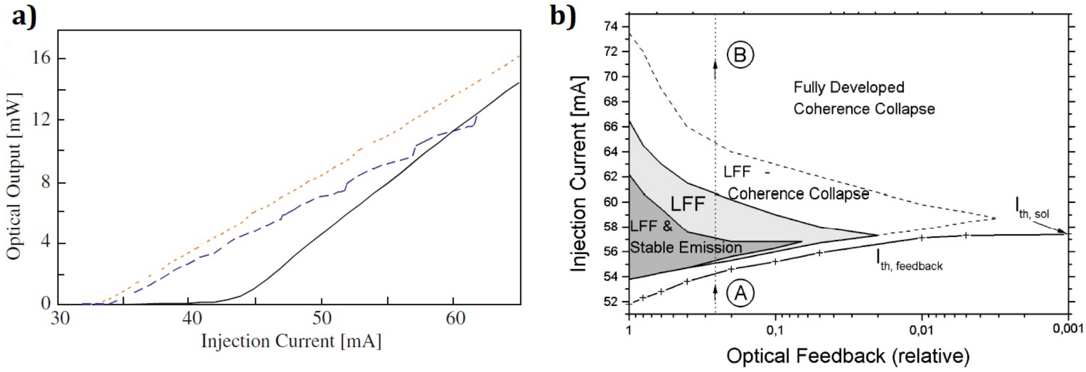

Figure 3.8: (a) Experimentally obtained light-injection current (L–I) characteristics of semiconductor lasers with optical feedback. Solid line: solitary oscillation, dotted line: external cavity length of L = 15 cm, broken line: external cavity length of L = 150 cm. The presence of external optical feedback reduces the threshold current value. Courtesy of [111]. (b) Dynamical behavior of a SL subject to EOF in feedback current space. Dark grey region: coexistence of LFF state and stable emission state. Light grey region: LFF regime. White region encompassed by dashed line: continuous transition between LFF regime and CC regime. Courtesy of [113].

Depending on the strength of the feedback light, many nonlinear dynamical phenomena are observed, such as bistability, instability, self-pulsation and coherence collapse (CC). Thus, it constitutes a parameter of primary importance to characterize the regimes of the dynamics of semiconductor lasers subject to external optical feedback [111] [112]. Depending on the feedback fraction, five regimes have been observed. Figure 3.9 and Table 3.1 report their main features.
However, it is useful to remark that external optical feedback is not only source of instabilities, but it can produce several beneficial effects that can strongly improve the laser performance, among which linewidth narrowing, noise suppression and large gain bandwidth. This results fruitful for many applications in spectroscopy, metrology and telecommunications [114]. Finally, several routes to chaos exist in nonlinear systems. One possibility is that leading to coherence collapse, just analyzed; nevertheless, an intermittent route to chaos can be also observed in SLs with EOF: the low-frequency fluctuations (LFF).
Coherence collapse consists in the complex and irregular dynamics occurring when the laser is operated above threshold in the fourth feedback regime. Its name derives from the drastic reduction of the coherence time, leading to an enhancement of the laser linewidth. The onset of coherence collapse strongly depends on the

DFB laser structure [115] [116], but not on the external cavity length, as long as the frequency of the external cavity remains much smaller than the laser relaxation frequency, in interband lasers.

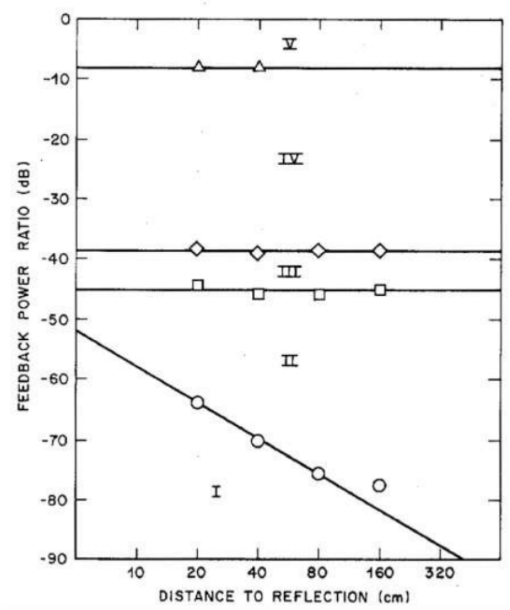

Figure 3.9: First cartography of regimes of optical feedback as a function of the external-cavity length and the feedback ratio in a 1.55-µm DFB QW-laser. Courtesy of [112].

LFFs occur irregularly in time, depending on the system parameters. However, LFFs name is derived from the value of their main frequency, being of the order of MHz to a few dozens of MHz. Hence, "low-frequency" must be intended as fluctuations with a frequency much lower than that of ordinary chaotic fluctuations, generally around several GHz [117], being the latter related to the laser's relaxation oscillations, if any.

As displayed in Figure 3.12, a typical feature of LFFs is a sudden power dropout with a following gradual power recovery. Apart from the main frequency component with a period around MHz, LFFs display two others components: the first is related to the external-cavity length, the second to a high frequency component with a subnanosecond period.

Ultimately, LFFs have been discovered near the solitary laser threshold for high feedback ratios; nevertheless, later it was proved that LFFs occur everywhere along the boundary between the optical feedback regimes IV and V, discussed above (Figure 3.8b) [113].

3.7.3 Chaos in QCLs

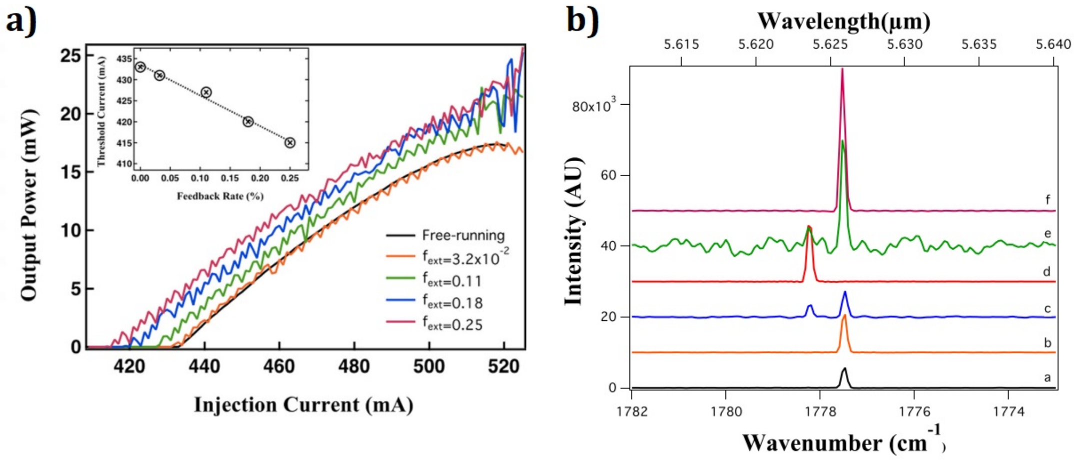

Figure 3.10: (a) LI curve for several feedback rates at constant external cavity length. The inset shows the corresponding threshold current as a function of the feedback rate. Courtesy of [118]. (b) Spectral signatures of the five optical feedback regimes of the 5.6-µm QCL under study. The FTIR spectra were measured at constant external cavity length of 13.5 cm and constant bias current of 435 mA. (a) Free-running case. (b) Regime 1, $f_{ext} = 9.1 \times 10^{-4}$. (c) Regime 2, $f_{ext} = 5.1 \times 10^{-3}$. (d) Regime 3, $f_{ext} = 3.2 \times 10^{-2}$. (e) Regime 4, $f_{ext} = 0.13$. (f) Regime 5, $f_{ext} = 0.25$. Courtesy of [118].

As mentioned many times, QCLs are semiconductor lasers based on intersubband optical transitions within the conduction band. This emission phenomenon profoundly impacts on the features of the QCL, behaving differently than conventional lasers.

First of all, QCLs are expected to present a zero α-factor, since the carrier transitions happen within subbands belonging to the same conduction band. Therefore, they have the same reciprocal space curvature, leading to a symmetric differential gain. However, real QCLs have small but non-zero LEF, causing the QCL behaving as a class A laser rather than a class B one. Hence, the QCL is intrinsically more stable than conventional SLs, even if subject to external perturbation [119].

Additionally, QCLs' carrier lifetime is very short, inducing the absence of relaxation oscillations.

Therefore, much effort has been done for chaos generation in QCLs. However, Jumpertz and co-workers in 2014 deeply analyzed the influence of optical feedback on a 5.6-µm AlInAs/GaInAs DFB QCL. Observing Figure 3.10a, a reduction of the laser threshold of 4% from 433 mA to 415 mA at the maximal achievable feedback ratio of 25% is noticed. Consequently, the optical output power significantly increases with the feedback rate. Furthermore, undulations appear for high feedback ratios. This phenomenon can be understood considering the interfaces between the modes of the two cavities [100] [120]: if the external cavity length is a multiple integer of the internal cavity length, destructive interference between the modes occurs, with subsequent maximum output power. Vice-versa, destructive interference is experienced when the external cavity length is half an integer of the internal cavity length, causing the output power to reach its minimum. In between these two extreme conditions, the power takes values in between the maximum and the minimum one, resulting in such undulations, noted for fixed bias current values.

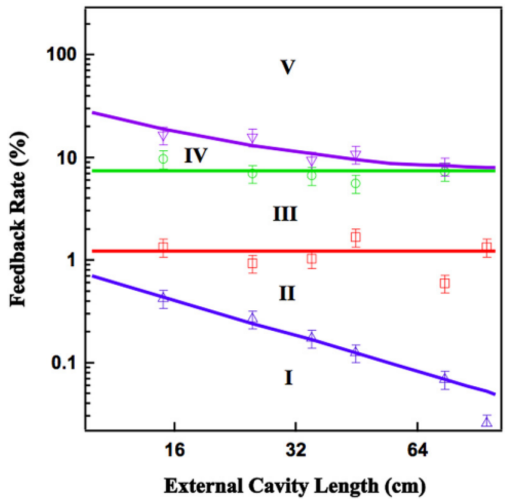

Figure 3.11: Cartography of optical feedback regimes as a function of the external cavity length and the feedback ratio. The transitions were deduced from the optical spectra at constant bias current of 435 mA of the 5.6-µm QCL under study. Courtesy of [118].

In this experiment, the external cavity length was fixed, though; still, they experienced undulations: the increase of bias current leads to an increase of temperature of the active area, and so to a modification of the refractive index of the effective laser cavity length, hence the undulations.
Figure 3.10b depicts different spectral characteristics, changing according to the feedback ratio, which increases when moving from the first regime to the fifth one. It is worth noting the fourth regime shows coherence collapse features, whereas the laser enters the extended cavity regime with the fifth one, showing single-mode operation and high output power. Finally, the cartography in Figure 3.11 is comparable with that in Figure 3.9 for a 1.55-µm DFB laser diode [112]. The

obtained results meet with theory: the transitions between two different feedback regimes occur for much higher feedback ratios in QCLs than in interband lasers; moreover, regime IV occurs for a range of feedback rates much narrower than that typically observed in interband lasers. Besides, the stable and single-mode regimes, namely regimes I, III and V are much broader.

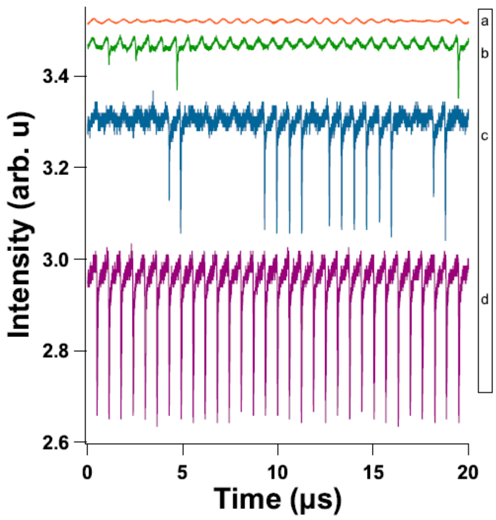

Figure 3.12: Experimental time traces in continuous mode with a temperature of 249 K and feedback strength of (a) 5.81%, (b) 6.27%, (c) 6.50%, (d) 6.72%. Traces (b) and (c) show the transitions between an oscillatory state and the LFF regime. Courtesy of [121].

These considerations are an evident proof of the increased QCL stability in presence of external optical feedback, to be accounted to the ultrafast carrier dynamics and reduced LEF, limiting the number of available external cavity modes [122].
Figure 3.14 [123] reports the experimental bifurcation diagram: the Hopf bifurcation destabilizing the QCL from its steady state is evidenced when increasing the optical feedback strength.
To gain insight into the observed bifurcation sequence and confirm the class A dynamical scenario observed experimentally, the behavior of a QCL under optical feedback is studied numerically, using the Lang-Kobayashi (LK) model [100], leading to a numerical bifurcation diagram (Figure 3.15). The simulated bifurcation scenario of the LK equations confirms a class A dynamical scenario in the studied QCL under external optical feedback.
Eventually, further investigation is demanded for understanding the impact of the external cavity length on the QCL's coherence collapse regime: for cavities

shorter than 60 cm, a factor-two enhanced upper limit is got for regime IV by reducing the length of 10 cm. On the contrary, for lengths between 60 cm and 95 cm, the operation region of coherence collapse is extremely narrow. A direct comparison with interband lasers is not conceivable, though, because of the absence of relaxation oscillations in QCLs.
In addition to this study, Spitz and co-workers [121] focused on the characterization of the nonlinear dynamics of a 5.6-µm DFB QCL in 2019. They demonstrated QCL under EOF is the best condition of operation for complex and sustained chaos at MIR wavelength (Figure 3.13).
In particular, the signal is primarily steady and then evolves to different nonlinear patterns by increasing the feedback strength, including LFFs (Figure 3.12). Moreover, chaos is generated close to the injection threshold, as well as far from threshold, with a strong dependence on temperature (Figure 3.16). Indeed, cryogenic temperatures make chaotic patterns easier to be generated. However, low-temperature conditions means bulky setup and incompatibility with real-field experiments.

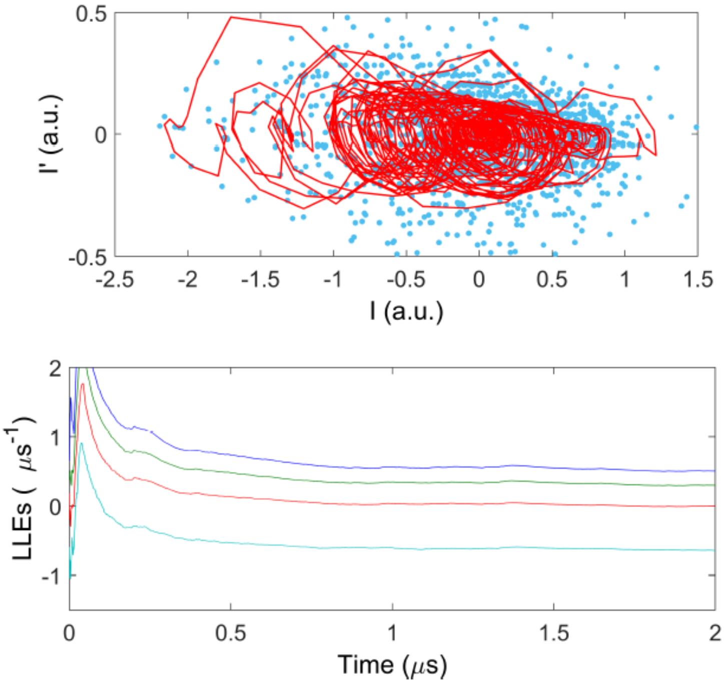

Figure 3.13: System dynamics analysis through LEs for the maximum feedback strength at 290 K. (Top figure) Phase portrait. The blue dots represent the retrieved values of the derivative of the laser's intensity I' as a function of the laser's intensity I. The red curve represents the phase diagram after noise filtering. (Bottom figure) Lyapunov spectrum for the four largest LEs calculated: $\lambda_1 = 0.485\ \mu s^{-1}$, $\lambda_2 = 0.284\ \mu s^{-1}$, $\lambda_3 = -0.021\ \mu s^{-1}$, $\lambda_4 = -0.656\ \mu s^{-1}$. Courtesy of [121].

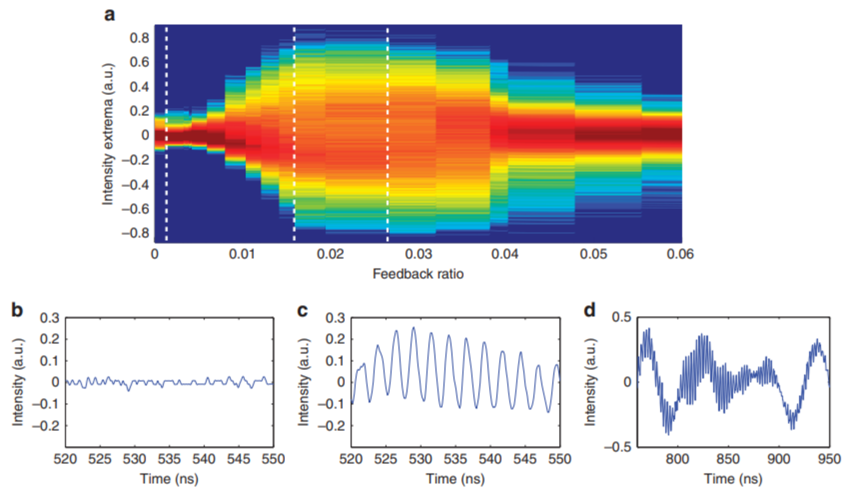

Figure 3.14: Experimental bifurcation diagram for P=0.02 and Lext=35 cm and associated time series. (a) Numerical bifurcation diagram. (b) Time trace for fext=0.11%, showing stable signal. (c) Time trace for fext=1.58%, showing oscillations at the external cavity frequency. (d) Time trace for fext=2.66%, showing both LFFs and oscillations at the external cavity frequency. Courtesy of [123].

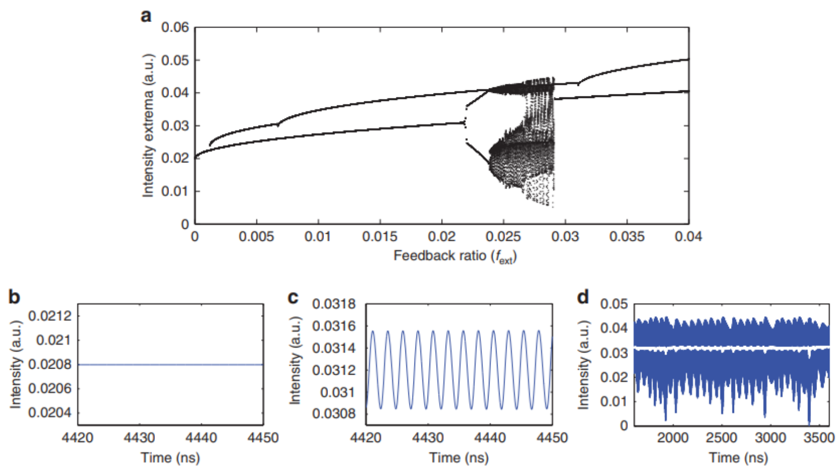

Figure 3.15: Numerical bifurcation diagram for P=0.02 and Lext=35 cm and associated time series. (a) Numerical bifurcation diagram. (b) Time trace for fext=0.11%, showing stable signal. (c) Time trace for fext=2.14%, showing oscillations at the external cavity frequency. (d) Time trace for fext=2.59%, showing both LFFs and oscillations at the external cavity frequency. The white curve corresponds to the filtered trace. Courtesy of [123].

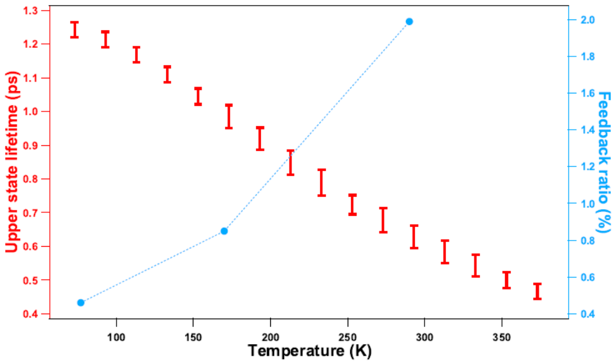

Figure 3.16: Simulation of the upper state lifetime evolution with temperature for the QCL under study (red) as well as required critical feedback (light blue) leading to LFF emergence for three temperatures: 290 K, 170 K, 77 K. Courtesy of [121].

Chapter 4

Secure communication

4.1 Introduction

Nowadays, a staggering amount of data is sent worldwide; this data contains sensitive information that needs to be encrypted. Secure communication [124] based on classical cryptography uses difficult mathematical algorithms to protect data from non-quantum threats. Meanwhile, the thriving attention devoted to the extensive field of quantum information [125] [126] [127] led to a dramatic development of large-scale quantum computers: they are capable to solve mathematical problems, intractable for conventional computers. As a consequence, quantum computers can easily break many of the public-key cryptosystems currently in use, seriously compromising the integrity and the confidentiality of secure communication. Hence, the need to overcome this fragility through suitable countermeasures: post-quantum cryptography (PQC) [128] and quantum cryptography [129], especially in the form of quantum-key distribution (QKD) [130]. Table 4.1 summarizes the main differences between PQC and QKD.

Post-quantum cryptography (also called quantum-resistant cryptography) is an evolution of classical cryptography and develops cryptographic systems that are secure against both quantum and classical computers, and can interoperate with existing communications protocols and networks. Nevertheless, this does not completely solve the problem. In fact, there may be undiscovered quantum algorithms that might easily break the security of the new cryptosystems. In other words, post-quantum cryptography may offer a partial or temporary solution.

By contrast, QKD may offer a safer solution, based on the unbreakable laws of quantum physics (hardware-based approach): by transferring data using photons of light in place of bits, it is possible to exploit photons' no-change and no-cloning [131] attributes: a confidential key transferred in this way between two parties cannot be copied or intercepted secretly. In this system, if an eavesdropper attempts to learn

about the key being established, the photon carrying the key changes state; thus, that key will automatically fail, alerting the two parties that their communication is not secure [132].
Despite the greater security provided by the physically uncrackable photon entanglement, QKD for large-scale communication systems is still hindered by the performances of low-speed, low-yield, expensive transmission apparatus. The current challenge is to realize QKD-based ground-to-satellite communication, overcoming the background noise that is detrimental during daytime. Propagation conditions are more favorable during nighttime, but this strongly restrains the availability of the transmission link. For instance, NIR light has drawn attention because it is immune to parasitic visible-light perturbation and because optical sources are widely available in this wavelength domain known for telecom applications. However, due to the lack of single-photon detectors, QKD technology is not yet available at MIR wavelength, that is one of the most relevant transmission domains.

Comparison metric	**PQC**	**QKD**
Security	Not 100% unbreakable	100% unbreakable
Implementation	Software-only	Specialized hardware
Communications media	Any type of digital communications media (RF, wired, optical)	Possible only with FSO and OFC
Cost	Low	High
Repeater compatibility	Current digital repeaters compatibility	Quantum repeaters necessity
Applications	High-volume consumer and standard commercial applications	Highly-sensitive applications (military, government, financial)

Table 4.1: Differences between post-quantum cryptography and quantum-key distribution.

4.2 The advent of chaos in secure communication

In this search for security, integrity and authenticity, chaos is starting to emerge as an alternative to the possible solutions presented so far. Chaotic regimes can be observed in nature: in weather and climate, biology and ecological processes, economy and societies [133]. The main characteristic of chaos is the generation of very complex patterns. The corresponding mathematical models can generate a large number of data, which are applicable as secret keys in the field of cryptography. This idea is in line with the discovery of common properties [134] between chaotic maps and cryptography, summarized in Table 4.2.

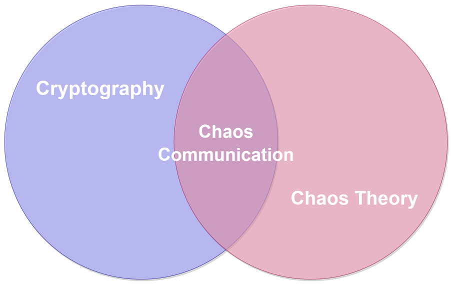

Figure 4.1: Relationship between chaos and cryptography.

Chaotic characteristics	Cryptographic Property
Ergodicity: topological mixing property	Confusion
Sensitivity to initial condition and control parameters	Diffusion
Deterministic	Deterministic pseudorandomness
Complexity	Algorithmic complexity

Table 4.2: Comparison of chaos theory and cryptographic properties.

In particular, "confusion" property obscures the relationship between the secret key and the ciphertext. So, as a result, each bit of the ciphertext is produced based on several parts of the secret key. By contrast, "diffusion" obscures the relationship between the plaintext and the ciphertext. In other words, changing one bit in the plaintext alters half of the bits in the ciphertext and vice versa. Additionally, chaotic systems have a deterministic yet unpredictable dynamics, which can be used as an effective tool in terms of a better cryptosystem. Hence, at the beginning of secure communication using chaos theory, the approach was to use the pseudorandom properties of the trajectories. Mainly basic models of discrete chaotic maps were used for crypto-schemes. Then, chaos synchronization [135] has changed the approach of communication, since it works as a whole cryptosystem: being the driving system the transmitter and the response the receiver, the basic idea consists in masking a message within a chaotic signal; then, at the receiver side, it is decrypted with the same synchronized signal. Since its introduction, chaos synchronization caught on in the field of cryptography, especially for its

characteristic of fast modes of communication. This property directly derives from the fact that it works in the physical layer of the transmission system, fully exploiting chaotic dynamics' features, such as randomness, determinism, mixing and sensitive dependence on initial conditions and system's parameters.
The main objective of this work is to focus on the synchronization of semiconductor lasers and its application in chaos-based optical communication, with the purpose of achieving an additional layer of security, together with very high transmission rates.

4.2.1 Research directions for engineering applications with chaotic lasers

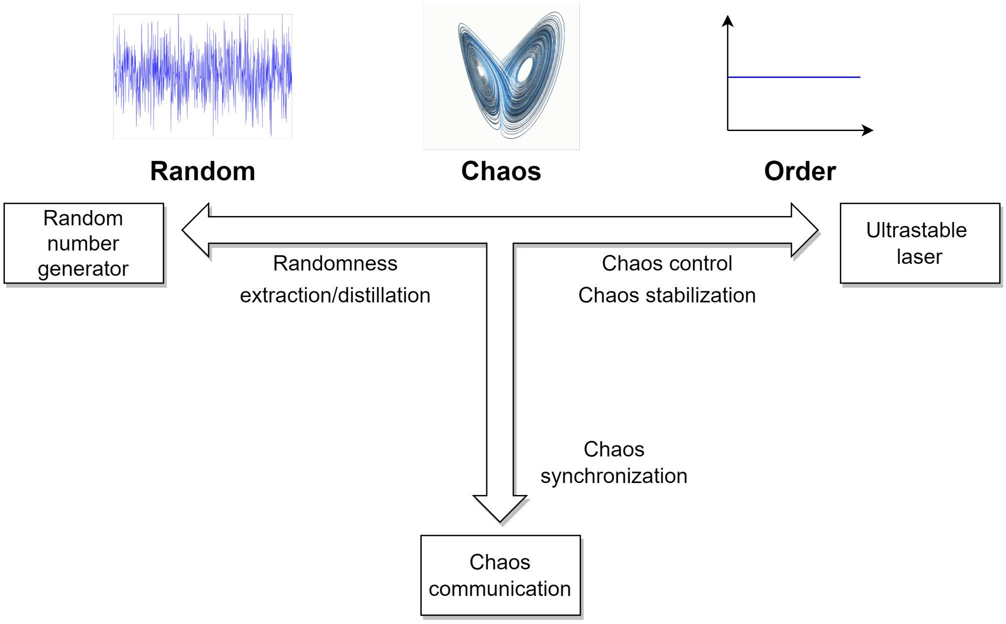

Figure 4.2: Three research directions for engineering applications with chaotic lasers [136].

Before going into the details of chaos communication, it is worth mentioning alternative applications of chaotic lasers in the engineering field. It is possible to recognize three main research directions, summarized in Figure 4.2:

- Chaos communication: the determinism of chaos results in chaos synchronization, whereas chaos complexity and its middle degrees are necessary for message hiding. For this application, chaos is used in a straightforward way.
- Random number generation: randomness must be extracted and distilled

from the deterministic chaos; hence, randomness must be maximized, whereas determinism must be canceled. This is possible by converting analog chaos signals into binary signals.

- Ultrastable laser: chaotic instabilities and complexity must be suppressed. Features of chaotic determinism (including unstable periodic orbits) are exploited to control chaos.

4.3 Chaos communication: basic concepts

The purpose of private communication based on chaos synchronization is to hide the existence of a message within a time-varying chaotic carrier waveform. Thus, it is considered a type of steganography, rather then cryptography. Table 4.3 reports the differences between the two techniques of secret communication. Figure 4.3

	Steganography	**Cryptography**
Definition	Concealing the existence of the message by using physical material	Hiding the "meaning" of the message by scrambling the message itself
Aim	Keep communication secure	Provide protection for data
Visibility	Never	Always
Failure	When discovering the presence of a hidden message	When able to decrypt and read the message
Concern	Embedding capacity Detectability of cover object	Robustness against deciphering
Key	Optional, but provide more security	Necessary
Advantage	Protection of both message and communicating parties	Robustness

Table 4.3: Difference between steganography and cryptography.

depicts the principle at the base of chaos-based private communication. A chaotic transmitter laser serves for message encryption: at a first glance, we say that the message is simply added (or multiplied) to the chaotic trace at the output of the transmitter itself. Once the information is properly concealed withing the chaotic fluctuations, the mixed signal (chaos + message) is sent to a receiver laser. In order to reproduce the original chaos carrier in the receiver, the chaos synchronization technique is utilized. In fact, transmitter's and receiver's chaos can synchronize to each other because of chaos determinism property. The message is decoded by subtracting (or dividing) the synchronized chaos carrier from the transmission signal. The recovery operation and the system performance are strongly affected by the quality of chaos synchronization. Some requirements need to be fulfilled for an effective synchronization. They will be investigated in the next sections.

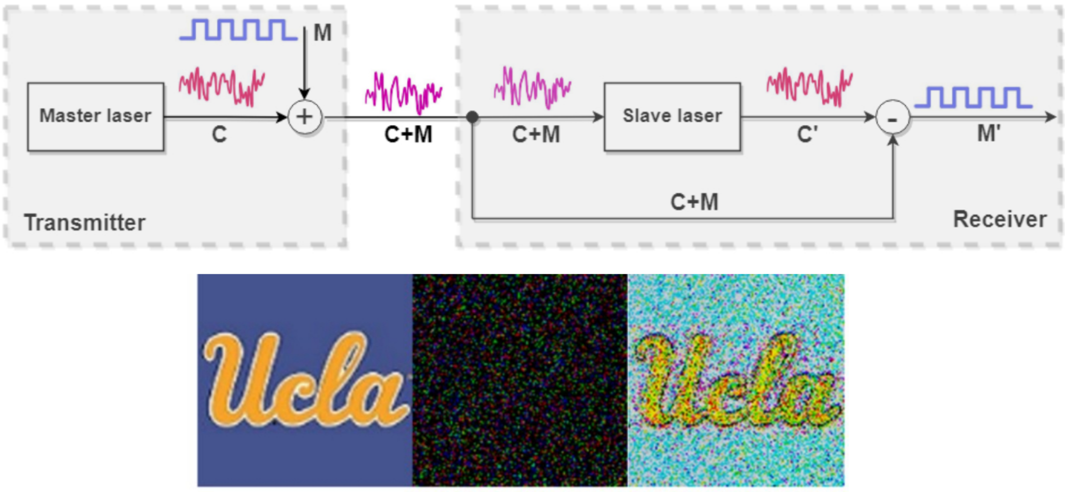

Figure 4.3: (Top panel) Schematics of private communication based on chaos synchronization. Courtesy of [136]. (Bottom panel) Physically secure image transfer using synchronized chaos between silicon optomechanical cavities: (left) message to encrypt, (center) chaos+message signal, (right) retrieved message. Courtesy of [137]

The experimental result deriving from a secure image transfer performed by [137] is more meaningful and straightforward (bottom panel of Figure 4.3). The initial message (left image) is concealed within the chaotic trace. If the message is well-hidden, an eavesdropper would get the image in the centre of Figure 4.3, with consequent impossibility to retrieve the enciphered information. Only a receiver sharing the "static keys" with the transmitter will be able to recover the message (right image), even if not without some errors, mainly due to channel impairments.

4.4 Chaos synchronization

The surprising discovery of temporal synchronization between two chaotic systems initiated the field of chaos communication, starting from the 1990s. The synchronization of periodic systems had been investigated and exploited with great care all over the years, since its first demonstration by Christian Huygens in the seventeenth century: two pendulum clocks sharing the same support oscillate in a perfectly identical way [138]. The concept of chaos synchronization is indeed self-contradictory and counter-intuitive, for the definition itself of chaos, and for its intrinsic properties, as it will be further deepened in the next sections.

4.4.1 Synchronization: basic concepts

Synchronization exists between two coupled dynamical systems, namely a transmitter and a receiver. When they are coupled to each other in a suitable way, they exert a form of control on each other, and it is possible for both systems to synchronize in their dynamics, either periodic or chaotic.
Chaos synchronization has represented a startling revelation, especially for its strong dependence on initial conditions, causing two temporal waveforms to exponentially diverge in time, even if they are subjected to very small perturbations.
The first experimental demonstration of chaotic systems dates back to 1990, when Pecora and Carroll showed that it was possible to have a temporal reproducible behavior between two electronic circuits, despite a small mismatch existed between the circuits. [139].

4.4.2 Synchronization in lasers

Synchronization in chaotic lasers is less straightforward with respect to other chaotic systems. In order to achieve the synchronization condition, two similar laser systems are used as drive (also called master laser) and response (also called slave laser), and a small portion of the driver output is injected into the response. The adjective "similar" must be interpreted in the sense that all the laser systems must consist of almost identical devices with almost identical parameters settings. The first numerical study of synchronization of chaotic lasers was presented in 1990 [140], paving the way for the first experimental proofs of chaos synchronization in an optical system in 1994 [141] [142].
In particular, Liu and co-workers [143] observed the chaos synchronization between two gas lasers with an intracavity saturable absorber and proved the synchronization dependency on the optical frequency detuning between the master laser and the slave laser.
In fact, there are two oscillation components in the electric field of the laser output; one is related to the emission wavelength of the laser, and therefore it is indicated as fast optical-carrier frequency. The other is the slow chaotic envelope component of the electric field, and it is related to the oscillation frequency of the laser. In laser diodes it is of the order of $10^3 - 10^9$ Hz, but rarely exceeds 10 GHz, according to the photon-carrier interaction in the laser medium.
Chaos can be experimentally observed with real-time detectors (MCT detectors or QWIPs in the case of QCLs) for the slower frequency range only, because of the

limitation in bandwidth (up to tens of GHz) of the photoreceiver. Nevertheless, both the fast and slow frequencies must be synchronized: the synchronization phenomenon of the carrier frequencies is known as injection locking and occurs thanks to the frequency-pulling effect [144]; this reveals to be fundamental to achieve the slow-envelope oscillations' synchronization. Additionally, whereas the first one is evaluated through a FTIR, the synchronization between the slow-envelope frequencies is easily assessed with a correlation diagram representing the output power of the slave laser as a function of the master laser output.

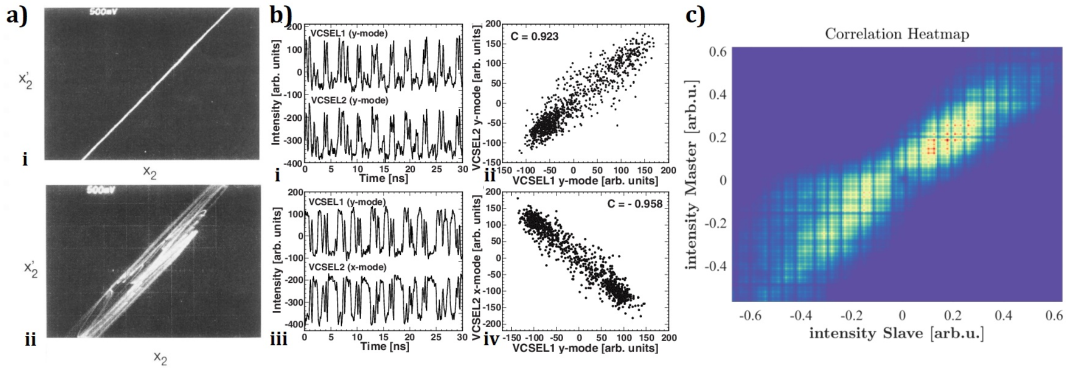

Figure 4.4: (a) Chaos synchronization between two electronic circuits. (i) Correlation diagram in the case drive and response circuits have perfectly matched parameters. (ii) Correlation diagram in the case the parameter mismatch of the two circuits is 50%: the synchronization is not perfect, but the response is still influenced by the drive. Courtesy of [139].
(b) Chaos synchronization (i, ii) and anti-synchronization (iii, iv), in coupled VCSELs. The left column represents the photon intensities for the two polarizations of the laser, whereas the right column reports the correlation diagrams. For chaos synchronization, the correlation diagram has a positive slope; on the contrary, for chaos anti-synchronization, the correlation diagram has a negative slope. Courtesy of [145].
(c) Correlation heatmap of chaos-synchronized coupled QCLs. Courtesy of [146].

4.4.3 Anti-synchronization in lasers

When injecting the chaotic fluctuations of the master laser into the slave laser, chaos anti-synchronization can also occur. This has been observed with both VCSELs [145], semiconductor lasers [147] and mid-infrared QCLs [146]. It is still not clear what effectively determines the switching between the two types of synchronization; nevertheless, it has been shown [147] how this can happen by slightly changing one of the control parameters of either the drive or the response, such as the bias current. More observations will be provided in chapter 5, where the results of our experience will be reported in details. Figure 4.5 depicts some examples of synchronization and anti-synchronization cases, respectively in VCSELs (a) and QCLs (b,c).

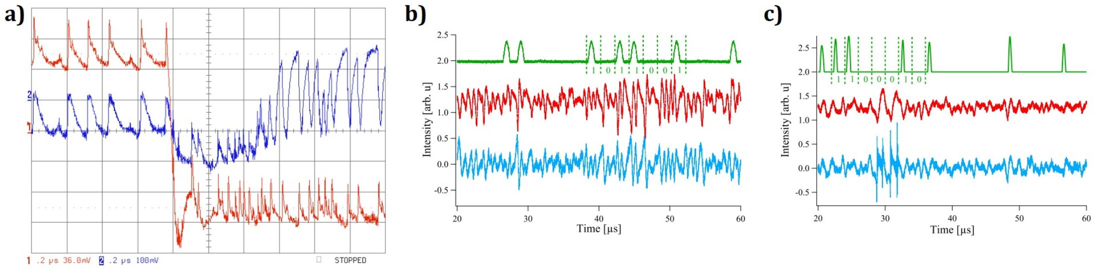

Figure 4.5: (a) Chaos synchronization and anti-synchronization in VCSELs. The red signal is the master one; the blue signal is the slave one. By slightly changing the pump current value at the drive, the system switches from synchronization to anti-synchronization. Courtesy of [147].
Time series retrieved during a private communication process between two unilaterally coupled QCLs emitting at 5.6 µm: (b) chaos synchronization case. (c) chaos anti-synchronization case. Courtesy of [146].

4.5 Chaos synchronization for private communication

4.5.1 Requirements

In order to facilitate the synchronization between two coupled lasers, some requirements must be fulfilled. As already mentioned, it is fundamental to rely on (almost) identical hardware for the drive and the response: this prerequisite may correspond to the demand for private keys sharing when a secure communication needs to be established between the two parties.
Besides, the message must have a small amplitude, in order to effectively conceal it within the chaotic waveform. In this way, the message can indeed be regarded as a small perturbation, not disturbing the larger chaotic fluctuations. This serves to ensure a stronger resistance to eavesdroppers' attacks, as well as to enhance the synchronization robustness. The higher the synchronization robustness, the more the correlation diagram looks like a straight line with a slope of 45°.
Furthermore, the message spectrum must be contained in that of the chaos: in order not to detect the message, its maximum frequency must be well hidden in the chaotic spectrum, as Figure 4.6 shows. As a consequence, the extension of the chaos spectrum determines the upper limit of the achievable bit rates.

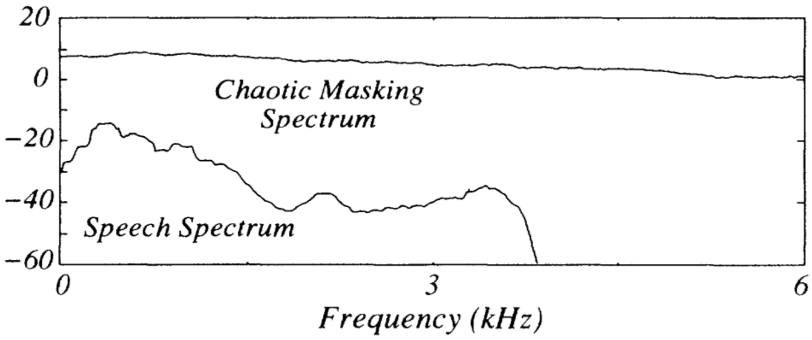

Figure 4.6: Comparison of the spectra of the chaos and of the message hidden within it, applied for secure communication. Courtesy of [148].

When the transmission signal C+M is sent to the receiver, the latter can synchronize with the transmitter chaotic waveform, generating in turn a chaotic waveform C' itself. There are no mathematical proofs that C' is identical to C. Nevertheless, this reproduction process is defined as "chaos pass filtering" effect, since the receiver is capable of separating the chaotic fluctuations from any other superimposed signal in the same frequency range of the chaotic carrier.
Experimental and numerical observations of the chaos pass filtering effect have been reported [149]. Figure 4.7 show how well the receiver reproduces the transmitter chaos. However, from Figure 4.7b and Figure 4.7c it is possible to observe that the external modulation peak is much weaker in the receiver output. Consequently, the message can be easily recovered by normalizing the transmitter and receiver signals, and subtracting them from one another.

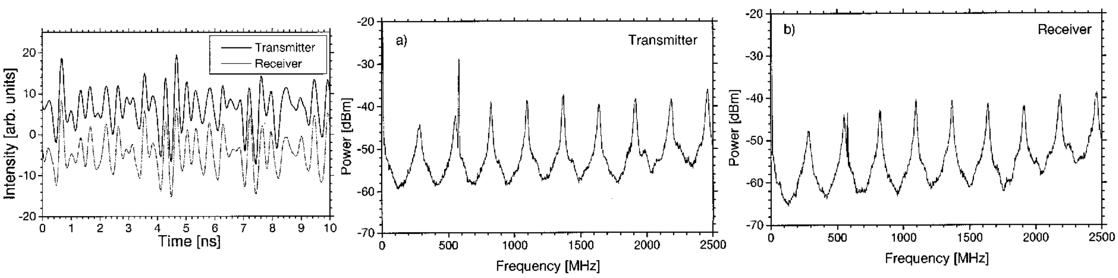

Figure 4.7: (a) Synchronized output intensity time series of transmitter (upper trace) and receiver lasers (lower trace).
RF spectra of transmitter (b) and receiver (c) lasers in the synchronization regime. The injection current of the transmitter laser has been modulated at a frequency f_{mod} = 5581.5 MHz, corresponding to the message signal. Courtesy of [149].

A simple mathematical formula expressing how to retrieve the signal after the chaos synchronization can be the following:

$$M + C - C' = M' \approx M, C - C' << 1$$

4.5.2 Characteristics of chaos communication

Hardware-base communication

Chaos communication is a hardware-based communication system since encryption is directly applied to the physical layer of the communication protocol (hardware key system).
One fundamental requirement for chaos communication is the use of nearly identical hardware (laser) to achieve synchronization of chaos. In other words, the lasers must have similar parameter settings: this specification is known as "hardware keys", since it has to be shared beforehand secretly. The receiver can reproduce a nearly identical chaotic carrier with respect to that of the transmitter by adjusting with a set of the "static" parameters values (K_S), to be shared beforehand. The adjective "static" is to be intended as unchanged system characteristics, after the hardware keys sharing between the authorized users. So, to sum up, the ultimate goal for chaos communication is to have a "one-pair device", with some hidden internal parameters that cannot be copied by any other devices. In this way, synchronization is possible between the specialized pair, but not with any other device. As an instance, the hidden parameters may be artificially embedded in the device during the fabrication process. It would be extremely secure if chaos synchronization can be achieved only between the one-pair device.

Chaos-synchronization-based

Synchronization of chaotic temporal dynamics is another fundamental feature of chaos communication, since it results essential for the message recovery at the receiver side. Therefore, the receiver is not only constituted by a passive photoreceiver; a parameters-matched, active laser device that can be synchronized is needed.

Privacy

Complex chaotic carriers offer a certain degree of intrinsic privacy in the hardware layer of communication protocol.
There is an essential trade-off between the robustness of chaos synchronization and privacy: the larger the robustness of chaos synchronization, the lower the privacy. Indeed, an eavesdropper can mimic the set of static laser parameters in an easier way if the synchronization robustness is high, by searching all the combinations of

available parameter settings.
Under the light of this analysis, many are the privacy issues to face. It is very difficult to assess the privacy or the security of chaos synchronization, since the security measures introduced to quantify the efficiency of software-based encoding are not suitable for it. In fact, the latter result in being mainly applicable to the key-distribution process, which is something that chaos communication schemes have not addressed so far. Moreover, chaotic waveforms provide an additional layer ir level of privacy beyond any conventional key distribution or encryption scheme that can be simultaneously part of the communication protocol.

Compatibility

Chaos communication is totally compatible with currently available optical devices, both in the NIR and MIR ranges. By contrast, quantum cryptography and QKD demand specialized hardware, like single-photon sources and detectors.

Analog communication

Chaos communication is an analog communication scheme, where an analog chaotic carrier is mixed with a digital signal. The analog feature of chaos inevitably implicates the degradation of the transmission signal while propagating through the channel, affecting the system performance (bit-error rate BER, signal-to-noise ratio SNR). Furthermore, the addition of channel noise on the chaotic carrier must be considered, since the synchronization robustness can be profoundly impacted by its presence.

Coherent communication

Chaos communication is a coherent communication in the sense that it requires an active laser device in the receiver to reproduce the chaotic carrier. Hence, the emission wavelength of the transmitter and the receiver must be controlled and matched, to achieve the injection locking condition, necessary to have synchronization.

4.6 Encoding and decoding techniques

The extraction of chaos is as crucial as chaos generation and synchronization, since it enables the utilization of chaos for communication applications. Different schemes have been proposed along the years, but they can be mainly categorized into three techniques: chaos masking (CMa), chaos modulation (CMo) and chaos shift keying (CSK).

4.6.1 Chaos masking

Chaos masking is the most straightforward masking scheme, since an information-bearing message (M) is simply added or multiplied to a chaotic carrier (C) "outside" the transmitter (Figure 4.8). A certain degree of security can be achieved if some properties of the chaotic carrier are correctly exploited: namely, its large spectrum and its noise-like appearance in the time domain. This procedure works well if the amplitude of M is small compared to that of C: synchronization robustness can be assured if the chaotic signal is subject to small perturbations. Generally, the message amplitude must be smaller than 1% of the average of the chaotic power. Finally, the message is deciphered by subtracting the response output C' to the transmission signal C+M. This occurs once the injection locking condition is satisfied, allowing for the two lasers to synchronize, according to the chaos-pass filtering effect.

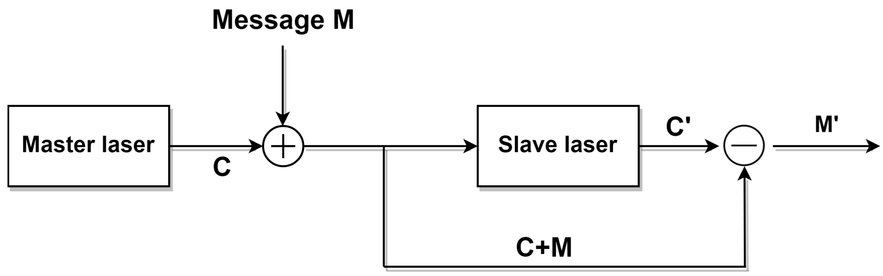

Figure 4.8: Block diagram of chaos masking: C, chaos; C', synchronized chaos; M, original message; M', decoded message [136].

4.6.2 Chaos modulation

This encoding scheme implies an internal encoding of the message, which is nonlinearly mixed with the chaotic carrier (Figure 4.9). Chaos modulation is characterized by a symmetric structure, where both the transmitter and the receiver are in a feedback configuration: chaos is generated from the feedback signal of C+M in both the transmitter and the receiver. This ensures perfect synchronization and high-quality decoding performance, independent on the amplitude of the message. Nevertheless, it is suggested to keep the message amplitude low enough, in order to prevent much change in the dynamics of the original chaotic system. In fact, it would be easier for an eavesdropper to retrieve the encoded message if the changes in the chaotic dynamics are more visible.

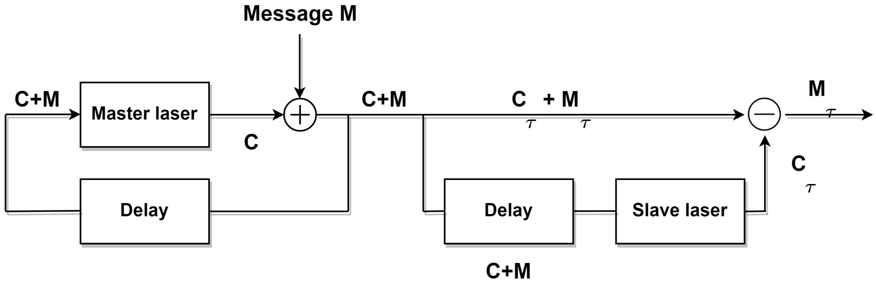

Figure 4.9: Block diagram of chaos modulation: C, chaos; τ, feedback delay time; C_τ, synchronized chaos with time delay; M, original message; M_τ, decoded message with time delay [136].

4.6.3 Chaos shift keying

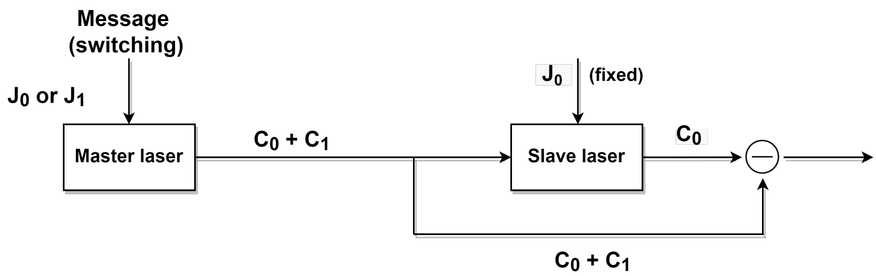

Figure 4.10: Block diagram of chaos shift keying: C_0, chaos generated at J_0; C_1, chaos generated at J_1; J_0, injection current corresponding to bit 0; J_1, injection current corresponding to bit 1 [136].

Chaos shift keying implies the modulation of one of the laser parameters (say J) through the message signal M. Since the message is a digital signal consisting of only 0 and 1 bits, the modulated laser parameter can assume two values only as well (say J_0 and J_1).
The receiver is instead made up of two lasers, whose selected parameter assumes a fixed value (respectively J_0 and J_1). The synchronization happens when the matching condition of the lasers' modulation parameter takes place: the message is revealed by observing the alternate synchronization of the two receivers.
A special case of CSK is the on-off shift keying, where the receiver is constituted by a single chaotic generator: the receiver's modulation parameter is matched to one of the possible values it can assume at the transmitter side. In this case, depending on the value of the binary message, the receiver does or does not synchronize with the emitter. The message recovery is accomplished by evaluating the synchronization

error, equal to the difference between the transmitted signal and the one at the output of the receiver. [150] gives an experimental demonstration of on-off shift keying encoding technique, where optical feedback phase is selected as modulation parameter: Figure 4.11 shows that the synchronization error is almost zero when the two lasers are phase-matched. The binary message is then recovered by applying a low-pass filter to the synchronization error signal, removing the high-frequency chaotic components.

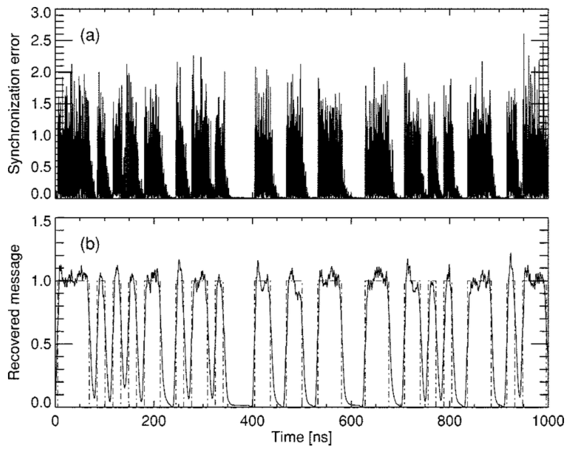

Figure 4.11: On-Off phase shift keying encryption scheme. (a) Synchronization error; (b) Recovered digital message at 64 Mbps after a filtering process. Courtesy of [150].

The bit rate of the message is here limited by the synchronization transient.

4.6.4 Comparison of CMa, CMo and CKS

[151] provides the comparison of the performance of the three encoding and decoding methods previously described, in the presence of channel noise and internal laser noise. The semiconductor laser here utilized is in the optoelectronic-feedback configuration. The same configuration can be used for the three encoding and decoding schemes, except for the place where the message is encoded. Figure 4.12 highlights chaos modulation is the best encryption scheme, since a BER lower than 10^{-5} can be obtained for CMo (ACM in Figure 4.12) when the SNR is lower than 38 dB. In the meanwhile, the BER is higher than 10^{-1} for CMa (CMS in Figure 4.12) and CSK. This is possible because CMo is the only one allowing high-quality synchronization in the process of message encoding by maintaining the mathematical identity between the transmitter and the receiver. On the contrary, CSK and CMa cause significant synchronization deviation in the systems because

they break the identity between the transmitter and the receiver in the process of message encoding.

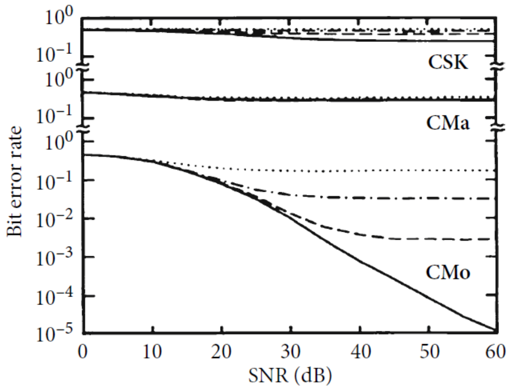

Figure 4.12: BER versus SNR for three different encryption schemes in the optical-injection cryptosystem. Solid line: obtained in the absence of laser noise. Dashed line: obtained for a noise level of $\Delta\nu = 100$ kHz for the emitter and receiver lasers. Dot-dashed: obtained for $\Delta\nu = 1$ MHz. Dotted line: obtained for $\Delta\nu =$ 10MHz. Courtesy of [151].

4.7 History of chaos communication in optical systems

After the first demonstration of chaotic communication in electronic circuits [148] in 1993, the idea was extended to optical systems the year after [152], through synchronization of solid-state lasers and recovery of the hidden message through subtraction at the receiver party. The data rate was limited to few kbps, but this paved the way for higher data rate transmission analysis. Firstly, in 1996 two numerical models with realistic operational characteristics simulated a secure transmission with near-infrared semiconductor lasers at a data rate of 5 Mbps [153] and 300 Mbps [154]. Because of the emission wavelength range, the transmission occurs through a fiber, envisioning for long-distance secure communication. And in fact, Mirasso and co-workers implemented a 50-km fiber transmission with amplification to compensate the losses in the fiber. This numerical analysis proved the strong potentiality of synchronized semiconductor lasers for long-range high-speed encrypted data transmissions.

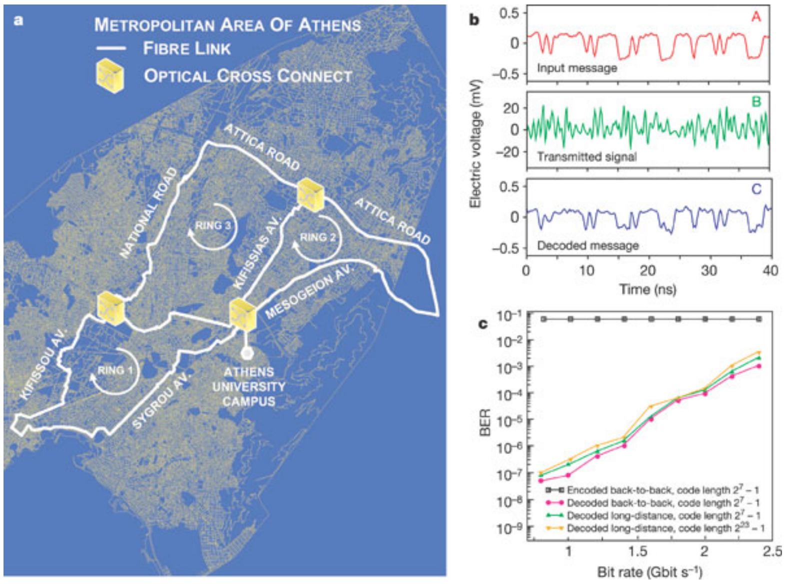

Figure 4.13: (a) Implementation of chaos-encoded communications in the optical communication network of Athens, Greece. (b) Time traces of a 1.0 Gbit/s applied message (trace A; BER$<10^{-12}$), carrier with the encoded message (trace B; BER$\approx 6\times10^{-2}$) and recovered message after 120-km transmission (trace C; BER$\approx 10^{-7}$). (c) The BER performance of the encoded signal (squares), back-to-back decoded message (circles) and decoded message after transmission for two different code lengths (triangles). Courtesy of [155].

One of the biggest results in terms of data rate and distances was achieved by Argyris and co-workers in 2005 [155]: exploiting a real-world optical network infrastructure of single-mode fibers belonging to the metropolitan area network of Athens, a secure transmission at 2.4 Gbps with a BER of 10^{-3} was achieved over a 120 km fiber. A BER of 10^{-7} was also obtained during the same experiment, but with a data rate of 1 Gbps. With this experiment, they demonstrated that the performance exponentially deteriorates with the increase of the bit-rate; this can be accounted to an imperfect synchronization, caused by the systems' parameters mismatch.

Finally, in 2005, a transmission experiment of a composite TV signal was carried out, utilizing a 1.2 km fiber span [156].The laser pair consists of unilaterally coupled standard DFB telecommunication lasers, selected between first neighbors on the same wafer for parameter matching. The carrier frequency of the signal is 2.4 GHz, and a trade-off between sufficient image masking by chaos and acceptable image quality after chaos cancellation must be taken into account; therefore, there is a 4-dB difference between the signal of the enciphered message and that of the chaotic carrier.

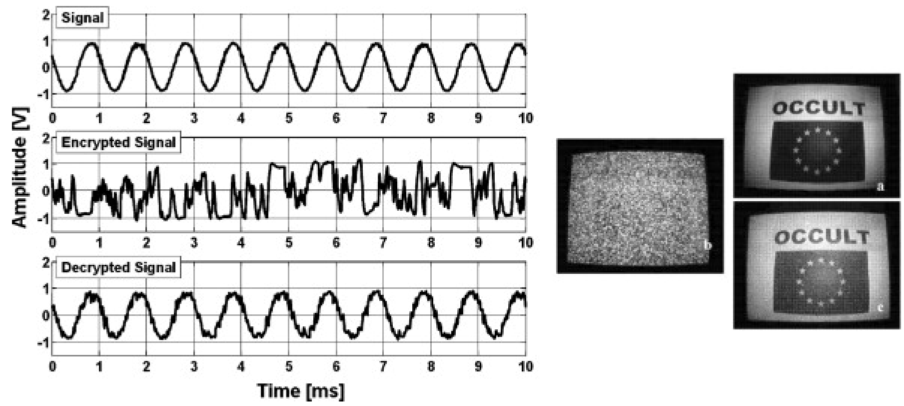

Figure 4.14: (Left column) A tone at 3 kHz at the input (top), masked by chaos (middle), and reconstructed (bottom); (Right column) A TV image at 5 MHz video bandwidth, chaos coded (left) and at the input (top right) and output (bottom right). Courtesy of [156].

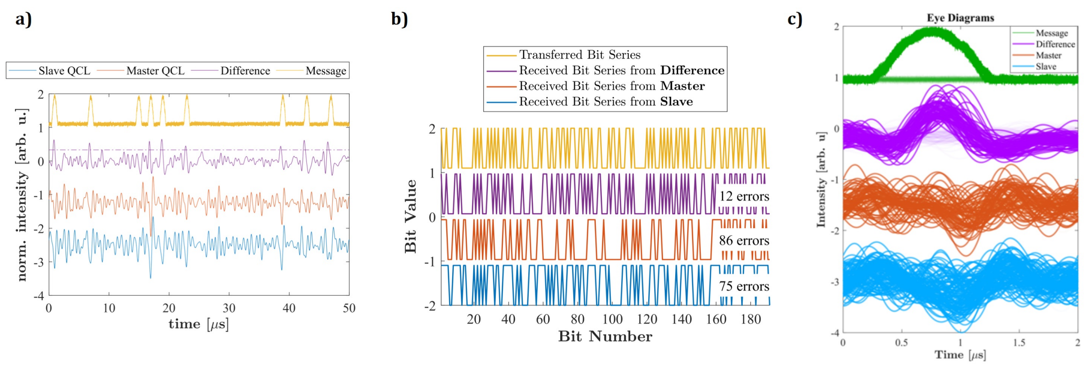

Figure 4.15: Chaos-based private communication between two coupled QCLs. Color legend: Initial message (yellow), difference (purple), master signal (red) and slave signal (blue). (a) Time traces, (b) Bit series. Except for the initial message, the number of errors is written on the right side of the bit series, with the corresponding color. The translation of the difference bit signal is also displayed by comparison with the initial message. (c) Experimental eye diagrams for the four time traces. Bits ciphered as 0 are drawn with light color, while bits deciphered as 1 are drawn with a brighter color. They are particularly distinguishable in the difference eye diagram, where "1" and "0" are well separated. Courtesy of [146].

As concerns the mid-infrared range, the first proof-of-concept of chaos communication has been recently demonstrated by Olivier Spitz and co-workers [146] with unilaterally coupled QCLs emitting at 5.6 µm. Some remarks can be highlighted observing Figure 4.15: from Figure 4.15a, it is possible to see how the response laser follows the drive thanks to synchronization. The difference signal highlights that synchronization is not perfect because of the lasers' parameters mismatch; nevertheless, the higher peaks of the difference signal are found in correspondence of the peaks of the initial message, corresponding to the transmission of bit 1. The private MIR transmission achieves a BER of 6%, which corresponds to 12 errors out of 191 bits (Figure 4.15b). From Figure 4.15c, through the eye diagrams' observation, it is possible to see that it is impossible to recover the message only from the signal of the master QCL, but it becomes possible for most of the bits from the difference signal. Unfortunately, the data rate in this study has been limited to 0.5 Mbps because of the coding. So, this limitation is not due to a limited chaos bandwidth.

Chapter 5

Chaos-based secure communication with QCLs

5.1 Introduction

The previous chapters were intended to provide an exhaustive theoretical background about the fundamental concepts at the base of our experience, that is the chaos-based private communication with mid-infrared DFB QCLs.
This chapter is finally devoted to a preliminary description of our experimental setup, with a subsequent focus on the procedure of synchronization. If this last step is successful, private communication is attempted; the parameters of choice for the evaluation of its quality are the BER and the openness of the eye in the eye diagram. As discussed afterwards, the system performance is assessed through typical means, employed in any form of communication; this has a direct impact on the main features of the entire apparatus, which reveals to be cost-effective and easy-to-implement.
At the end, the results of the full procedure are presented, together with a detailed analysis, highlighting the overtaken criticalities and the challenges still open for future works.

5.2 Experimental setup

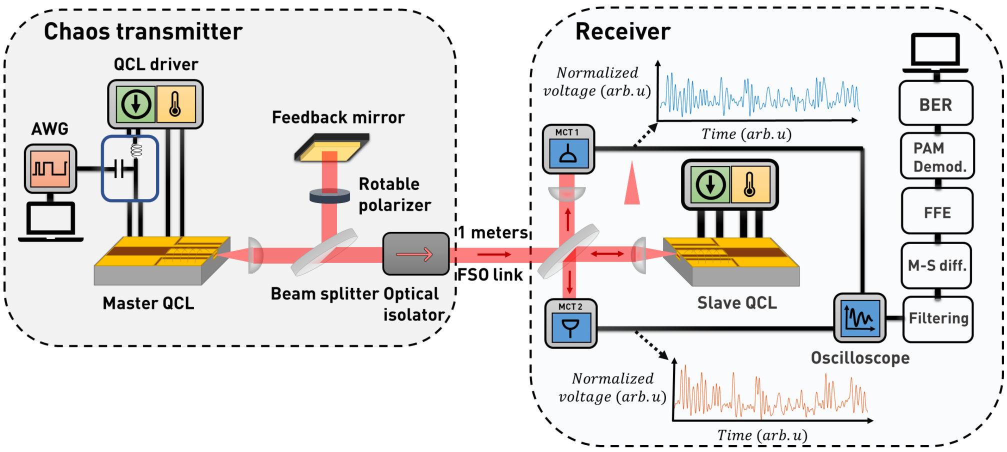

Figure 5.1: Setup for chaotic secure communication with two room-temperature 9.33-µm DFB QCLs. The apparatus is split in two parts: the transmitter is dedicated to chaos generation and masking, whereas the receiver is devoted to synchronization and message recovery.

Figure 5.1 shows the experimental setup used in our experiment. It consists of a DFB master QCL (ML), driven chaotic by external optical feedback (EOF). This feedback is characterized by a gold tilted mirror (Thorlabs, PF10-03-M02) inserted after a mid-infrared holographic wire-grid polarizer (Thorlabs, WP25H-Z), allowing us to precisely tune the feedback strength. In fact, the generated optical chaos tightly depends on it. The master light beam is sent towards the DFB slave QCL (SL), which is not in an external-cavity configuration. Consequently, non-linear dynamics can be observed in the slave output only through the injection process. Finally, the signals from both the master QCL and slave QCL are retrieved with separate Mercury-Cadmium-Telluride (MCT) detectors (Vigo Photonics AIP-10k-1G), whereas the timetraces are acquired with a fast oscilloscope (Tektronix MSO44) and then analyzed offline with a custom Matlab program. The oscilloscope bandwidth is 500 MHz, and the sampling rate is fixed at 250 MSample/s.
In order to ensure unidirectional coupling, an optical isolator (Innovation Photonics) is placed between the transmitter and the receiver, distant around 1 meter from each other. In this way, any back-reflected beam from the slave laser into the master laser is blocked; this requirement results fundamental not to have mutually coupled lasers, condition for which the master laser's nonlinear dynamics can be profoundly affected by the slave, as experimentally demonstrated for semiconductor lasers [157].

All the equipment must be MIR compatible, making the overall free-space attempted private communication further challenging.
Both QCLs are housed in Newport LDM-4872 mounts. Both QCLs are pumped by continuous-wave current sources: for the master, a low-noise source is employed (Wavelength Electronics, QCL1500LAB); for the slave, there is no need of a strict compliance regarding noise, so a different choice is made (Newport, LDX-3232). Indeed, optical injection is especially applied to reproduce the master's behavior on the slave. Consequently, if the ML output does not present good properties in terms of linewidth, bandwidth and noise, these would be very likely observed on the slave laser. Particularly noise could be disadvantageous for communication applications. Hence, the need to limit the noise at the transmitter side.
The lasers' housing is designed to be evacuated with a vacuum pump to prevent frost from forming on the laser, and to provide stable temperature control at very low temperatures. The lasers' operation temperature is thus tuned through separate temperature controllers (Newport, LDT-5412), but it is stabilized thanks to a Peltier cooler.
As already mentioned, QCLs are quasi-class A lasers; this means they are intrinsically stable. So, the generation of chaotic nonlinear dynamics has been proven to be hard, without the use of external optical feedback or/and electric modulation. Moreover, low temperatures help in the observation of more complex chaotic dynamics. To produce a more robust chaotic output, the master mount is additionally purged with dry air, in order to increase the master temperature operating range. This prevents condensation and frost at lower temperatures. The dry air purge occurs by displacing the air in the housing with dry air and then sealing it. Nevertheless, cryogenic temperatures are never reached.
Quantitatively, the master temperature is kept around 273-276 K (0-3°C), whereas the slave operates at around 288 K (15° C). The slave temperature is not arbitrarily chosen, since the environmental dew point is continuously monitored to prevent condensation. Maintaining temperatures above 273 K allows for experiments within ambient temperature range conditions. This is advantageous because it is cost-reducing, but also demonstrates chaos applications are possible in non-critical operating conditions.
Finally, the message is provided by an arbitrary waveform generator (AWG, Keysight Technologies, 32522A) and supplied to the laser through a bias-tee (Pasternack, PE1606A), allowing for modulating the device around the set bias current. Again, also the bias-tee choice must take into account its frequency operating range, since it is necessary to ensure it does not cut high-frequency signals.

5.2.1 9-µm DFB QCLs

In the following, additional information about the QCLs under study are provided. Both the DFB QCLs emit single-mode radiation around 9.33 µm, and exhibit a wavelength shift when varying the temperature or current of operation. Figure 5.2 and Figure 5.3 represent the optical spectrum in wavenumber of respectively the master and the slave. By observing the purple and green trace, a rough estimation of the wavelength shift as a function of current can be given: 129 $\mathrm{pm\,A^{-1}}$ for the master, and 171 $\mathrm{pm\,A^{-1}}$ for the slave.
The magenta spectrum discloses two interesting features for both QCLs when the current is around 450 mA: the lasers become FP, as can be seen by the broadening of the spectrum and the appearance of multi-modes, around the emission wavelength. The intensity of these does not decrease moving away from it, but takes on an irregular pattern, which is not the same for the two lasers. Besides that, it is possible to notice the appearance of an additional single-mode around 9.04 µm and 8.88 µm for the slave and master, respectively. However, their intensity is reduced compared to that of the main modes when the lasers operate in single-mode conditions. They

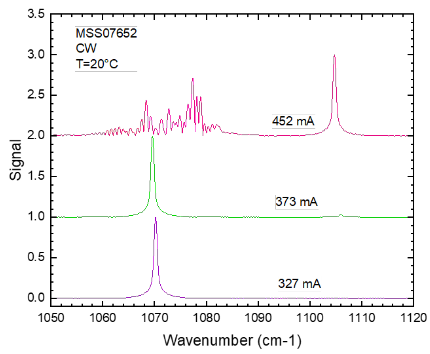

Figure 5.2: Optical spectrum of the free-running master laser when biased at different current's values at 293 K, above threshold: (purple) 327 mA, (green) 373 mA, (magenta) 452 mA (provided by MirSense).

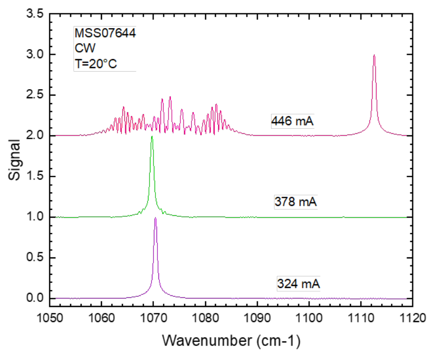

Figure 5.3: Optical spectrum of the free-running slave laser when biased at different current's values at 293 K, above threshold: (purple) 324 mA, (green) 378 mA, (magenta) 446 mA (provided by MirSense).

come from the same batch, and both their intensive (cavity length, facet coating, etc.) and extensive parameters (carrier lifetime, gain, etc.) are matched to the best extent. Consequently, also their microscopic parameters such as carrier lifetime, gain and photon lifetime are almost identical. These parameters are important to ensure optimal synchronization, constituting the private "static keys" of secure communication. Moreover, to make this procedure successful, currents below 380 mA are handled, where monomode operation is guaranteed.

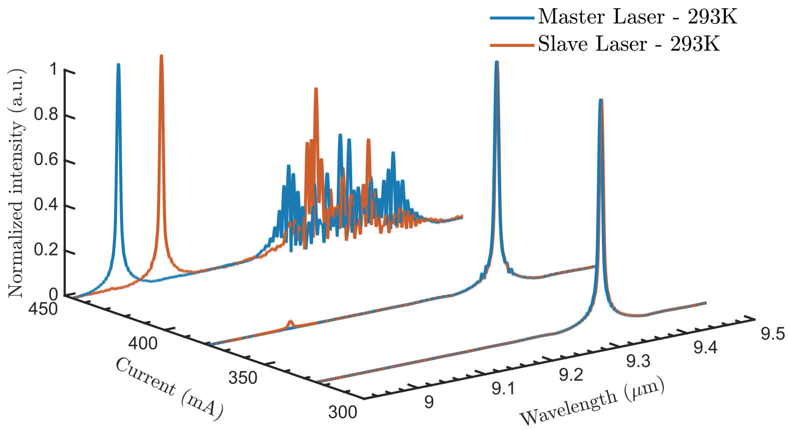

Figure 5.4: Optical spectra of the free-running master and slave lasers at 293 K, for the currents provided in Figure 5.2 and Figure 5.3. For the sake of simplicity, the spectra are superposed on a 3D graph to facilitate the comparison.

Nevertheless, it is not entirely true that the lasers parameters are totally equal: to have wavelength matching, at the same temperature, the currents are not precisely identical, as emerges from Figure 5.2 and Figure 5.3. However, for these currents, when monomode operation is ensured, the optical spectra are almost perfectly overlapped, as clearly seen in Figure 5.4.
A deviation in their behaviors is detectable in Figure 5.5, where the LIV curve is depicted. The master laser is more powerful than the slave, and its lasing threshold is lightly higher than the slave's one (300 mA vs 292 mA). This is a further demonstration of how impacting are parameters variations during the fabrication process: no matter how hard we try to produce two devices as identical to each other as possible; inaccuracies of different nature lead, if only slightly, to structural and behavioral differences for both optical and electrical properties.
It is also fundamental to say that our QCLs are not meant to be used for communication purposes; MirSense is in fact a startup whose products are mainly aimed at the spectroscopy and sensing market. Therefore, the superlattice structure is first and foremost optimized to have an emission wavelength that is as coincident as possible with the absorption wavelengths of all those molecules to be detected. Furthermore, the heterostructure itself influences the output power, as well as the

threshold current: the greater the number of quantum wells that make up the single period of the structure, the greater the power and threshold current will be. Generally, the number of quantum wells is around 10-35, depending on the application.
Another key role is played by the width of the active region. For example, to have high-speed modulations, a broad modulation bandwidth is required. For this, the number of quantum wells, as well as the width of the active region, must be reduced. In fact, the smaller the cavity, the higher the speed, since the equivalent capacitance of the structure is decreased. Obviously, having a smaller capacitance to charge and discharge allows higher modulation frequencies to be achieved. Thus, these are only considerations from an electrical point of view.
As for our lasers, the package developed by MirSense involves 15 external wires. In the case of high-speed applications, the number of wires is one. Not only that: our lasers were not manufactured to be modulated, but to have a high enough output power for spectroscopic applications. Nevertheless, still the measured output power is somewhat limited, as highlighted by Figure 5.5.

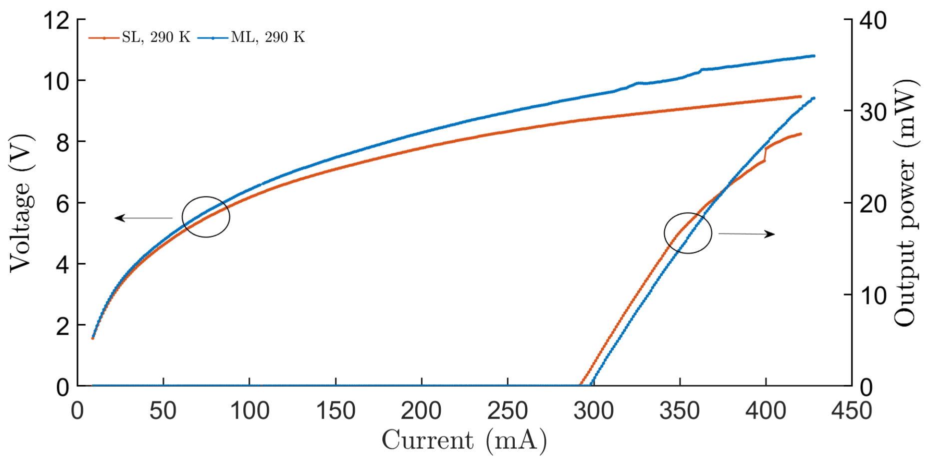

Figure 5.5: Measured Light-Current-Voltage (LIV) of the master (blue) and the slave (orange) at 290 K (17°C°). The x-axis reports the bias current values; the left y-axis represents the voltage as a function of the bias current, whereas the right y-axis the output power. The experimental data agree with those supplied by MirSense.

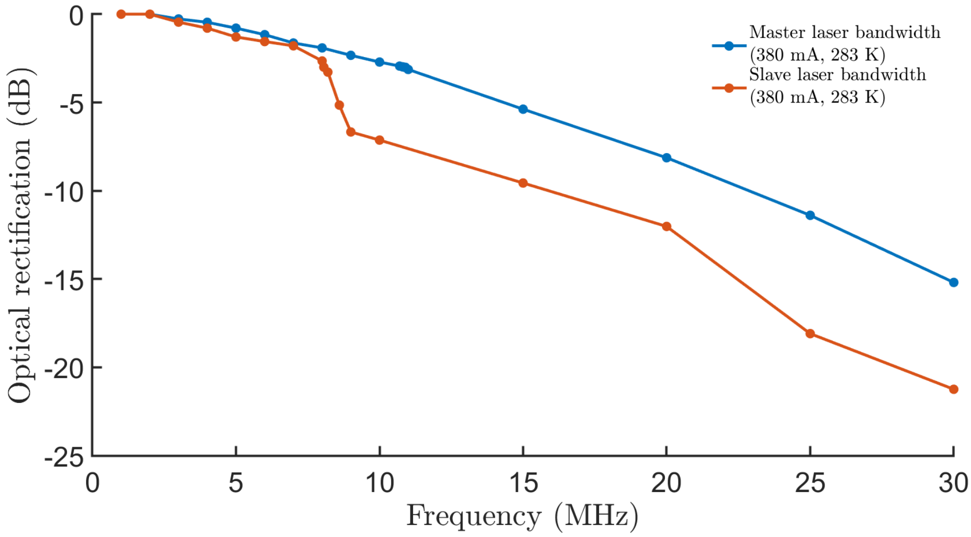

Figure 5.6: Experimental direct modulation bandwidth of master (blue) and slave (orange) lasers, at 283 K (10°C).

In order to have clear in mind what the limit is for the direct modulation of our QCLs, the modulation bandwidth is experimentally measured at a temperature of 283 K (10°C) (Figure 5.6): for the master, this is around 12 MHz, while for the slave just over 8 MHz. In addition, the 3-dB bandwidth shape of the slave is sharper than that of the master, revealing a cut-off frequency that most likely results from an RC impedance present in the experiment setup. This constitutes a low-pass filter, limiting the modulation of the slave further more than the master's one. This also has consequences for the private communication to be established between the two devices: since the slave is more band-limited, the data-rate of the message hidden within the master cannot exceed 8 Mbps. If it did not, higher frequencies would be cut off by the low-pass filter, resulting in a higher BER, i.e., worse performance. However, the modulation bandwidth really depends on the device's structure: hundreds of GHz for the modulation bandwidth have been theoretically predicted through mathematical models [158]; yet, practical bandwidths may be much less than 100 GHz. As a matter of fact, free-space optics data transmission with bit-rate in excess of 10 Gbps has been recently demonstrated by employing a CW room-temperature 9-µm QCL, together with high- frequency amplitude modulator and quantum cascade detector [159]. Indeed, other challenges derive from the availability of measurement instruments suitable for the infrared-range, but also broad enough in terms of bandwidth. In fact, it is not possible to observe the QCLs effective properties if we still rely on inadequate equipment. Fortunately, the market is now enriching because of the increasingly-urgent demand, but still the costs are not comparable with those of NIR devices. This is glaring since the issues to face for the production of such instruments are much more complex. Finally, as regards our experiment, even if our lasers would have been high-speed devices, still we would have been limited by the maximum rate achievable by the arbitrary waveform generator, fixed at 30 MHz. Other restraints are those determined by the oscilloscope, whose bandwidth is 125 MHz per channel, and by the photodetector, whose cut-off frequency is 700 MHz.

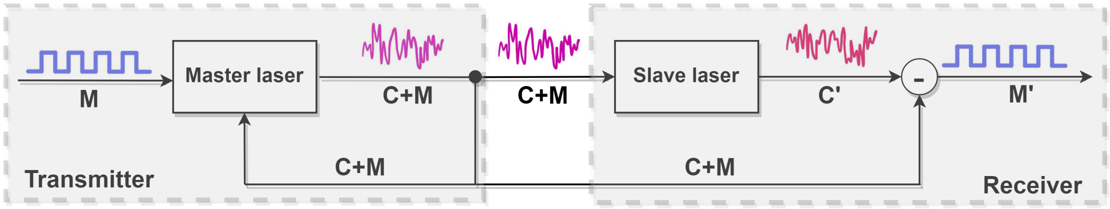

Figure 5.7: Message enciphering technique of our experimental set-up: the external feedback makes it close to CMo; the message injection before light generation and the message recovery operation, instead, to CKS.

Another topic to deal with concerns the message encryption. In chapter 4 three main encryption techniques have been analyzed: chaos-masking (CMa), chaos-modulation (CMo) and chaos-shift keying (CSK). Since we perform the communication with two QCLs, the message has to be included directly in the bias current. Therefore, it is not so straightforward to classify our message encryption technique within one of the aforementioned possibilities. Our experiment is not CMa because this corresponds to the case where the optical chaos is created and then, outside the feedback loop, the message is added. This is doable with fiber configurations where it is easy to combine two signals. It is neither CMo: it is true that the message is part of the signal that conforms the chaos wave. But for CMo, the message is added after the optical signal is generated by the laser, so this is different. In the same time, our configuration cannot be classified within CSK techniques. Indeed, CSK is characterized by two different states (synchronized and non-synchronized) and this actually corresponds to bit-0 and bit-1, respectively. When the bit is 0, the signal of the slave is a copy of the master's chaos, so this is "synchronized". When the bit is 1, the signal of the slave is actually no longer a copy of the master's chaos but a combination of master's chaos + bit-1 and this is considered "non-synchronized". The message recovery is accomplished by evaluating the synchronization error, given by the difference between the transmitted signal and the one at the receiver output. Moreover, CSK corresponds to the case where the message is injected before light generation and this corresponds to our experimental configuration.

However, CSK implies a change in the chaotic fluctuations according to the value that the modulation parameter acquires. In our experience, the chaotic waveform does not change its properties when sending a bit-0 instead of a bit-1. So, we can state our configuration is placed in between CMo and CSK (Figure 5.7). Though, CMo is generally considered as the best option for secure communication, but no proofs were provided to demonstrate this is still valid for QCLs. Still, true CMo could improve the result in our case and the reason is that the bias current of the laser is not changed during the process; on the contrary, in the existent configuration, current is changed by the modulation, which means that wavelength also changes and this can impact the quality of synchronization. But if we want to implement CMO, we will need an external modulator, like the one described in [159], and a loop with an optical isolator to reinject the light into the QCL. So this will make the setup more complex and we need to pair the QCLs with the right modulator. Indeed, mid-infrared modulators are not commercially available yet.
In the meantime, the bias current modulation through the message may reinforce chaotic oscillations, constituting an additional degree of freedom for the lasers' nonlinear dynamics. So, on the one hand we may have a detrimental effect concerning the quality of transmission; on the other hand, we may enhance security, by concealing the message in a more efficient way, thanks to more complex chaotic outcomes.
A key role is also played by the relative amplitude of the message with respect to that of the chaotic waveform. In our experience, the message consists of a non-return-to-zero (NRZ) PRBS-7: it is a pseudo-random binary sequence, which is generated through a deterministic algorithm, yet difficult to predict. The size of the sequence is $N = 2^7 - 1 = 127$: the 127 bits repeat in time, with the data-rate set through the AWG.
The chaos pass filtering effect [149] permits the synchronization of chaos only if the message is sufficiently small compared to the largest chaotic fluctuations. Having observed a peak-to-peak chaotic fluctuation of about 200 mV, the message amplitude has been varied from 1 mV to 15 mV in order to find the best trade-off in terms of security and BER. In fact, the higher the message amplitude, the easier is to retrieve the message through post-processing techniques. So, the smaller the BER will be. On the contrary, security may not endure the message amplitude increase, being it favored by the opposite condition. However, the presence of noise and its influence have not been investigated yet. Surely, for an effective communication, the signal level needs to be clearly distinguished from the noise floor. However, no studies have been conducted on how influential noise can be in QCLs nonlinear dynamics.

Chaos generation is not an easy task to accomplish with QCLs. External optical feedback and optical feedback re-injection are therefore exploited for this purpose.

The general trend is that it is easier to observe more robust and reproducible nonlinear dynamics when the external cavity length is reduced; in the meantime, a smaller external cavity length leads to less complex chaos, since less external cavity modes are excited; consequently, there is also less chance to have coupling between internal cavity modes and external ones. Hence, less complex nonlinearities may arise. So, a trade-off needs to be performed; from the observations made during the several measurements, the good compromise seemed to be that leading to an external cavity length of $L_{ext} = 12 \ inches = 30.48$ cm. Moreover, the beam-splitter used has not the same percentage in transmission and reflection: respectively, we have around 65% in reflection, and 35% in transmission. In this way, the reflected output beam is stronger than the transmitted one, in order to increase the strength of the re-injected feedback beam.
In addition, low temperatures favor the chaos stability, together with a very slow and very accurate feedback strength modification, as we do with the polarizer.
Also the bias strength influences the chaotic stability: the higher the bias current, the more robust the chaos is. With chaos "robustness" we refer to the fact that once chaos is generated, the output keeps its chaotic patterns along time. Thanks to the spectrum observation, it has been indeed noticed how easily more complex chaotic patterns may very likely turn to periodic or quasi-periodic oscillations where different frequency components appear. However, because of the oscilloscope's bandwidth constraint, frequencies higher than 125 MHz cannot be observed. The attainableness of going beyond in frequency could have unveiled striking features, related to the external-cavity frequency. In our case, its theoretical value is around 490 MHz, but there is no chance to experimentally retrieve its actual value. In fact, a discrepancy between experiments and theory has been reported in QCLs ([37], [160]), showing a measured value lower than the theoretical one. The same studies have demonstrated period-doubling phenomena, where the external-cavity frequency was modulated by other periodic signals. It was also surprising how the external cavity frequency was still present in LFF patterns. So, this is an evident proof of how destabilization in QCLs arises from the external-cavity frequency.
All these observations are qualitative ones, since data recordings would not be reliable, because of the unpredictability and sensitive dependence to initial condition of chaos itself.

Figure 5.8 represents the sensitivity of the chaotic fluctuations to the tilting of the feedback mirror. Even if the changes are minimum, the chaos bandwidth can be more or less flat. In this latter case, strong frequency components around 5 MHz appear. Their origin is still unknown, yet under study. What we may suppose is that it may derive from the coupling of external and internal cavity modes. As later discussed, the bandwidth's shape is very influential on the system performance. Furthermore, it is evident from the experimental timetraces that the flatter the bandwidth, the more complex the chaos: a more evident pattern is recognizable as

long as a strong frequency component dominates the chaotic response.
Moreover, the 15-MHz chaos bandwidth allows to appreciate the message presence around 1 MHz (having set a 1 Mbps data-rate for the enciphered PRBS-7). The more visible the message it is, the less secure the communication is. On the other hand, by observing the 50-MHz chaos bandwidth, some frequency components pop up around 19 MHz and 39 MHz, whatever is the tilted-mirror configuration. This is not a case; again, the precise origin is still uncertain, but the coupling between the different modes can be accounted as an explanation.

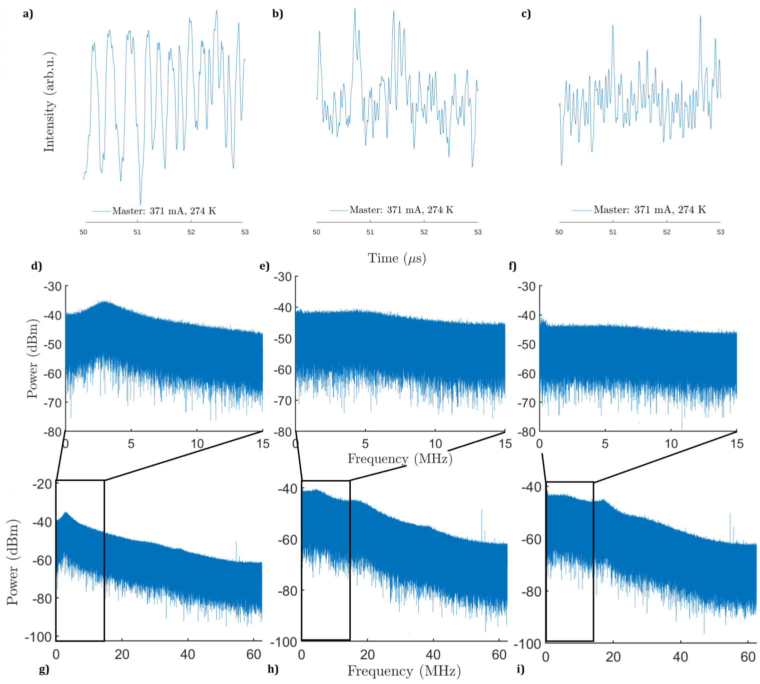

Figure 5.8: Master laser chaos timetraces (a,b,c) and electrical chaos bandwidth (15 MHz, d,e,f, 60 MHz, g,h,i) for different configurations of the feedback mirror. The ML is biased at 371 mA, at 274 K.

.

Data-rate limitations do not only derive from electrical modulation, since also the chaos bandwidth must be analyzed. The message needs to be well concealed within the chaos; in terms of bandwidth, this means the chaotic bandwidth must be much wider than the message one. Figure 5.9 represents the power spectrum of the chaos generated at 9 µm (blue trace) and 5.6 µm, from Spitz previous work [121]. A bandwidth broadening is clearly visible at 9 µm, allowing for an increase of the data rate of the concealed message. In fact, the chaos examined around 5.6 µm did not allow to go beyond 0.5 Mbps. Indeed, the blue trace presents a cut-off

frequency around 20 MHz; on the other hand, the green trace has a peak around 1 MHz, and a cut-off frequency around 5 MHz.
Still, QCLs produces a chaos bandwidth that is three orders of magnitude smaller than that of conventional semiconductor lasers [161] (MHz instead of GHz), because of the absence of relaxation oscillations.
In other words, by optimizing the hetero-structure, one can increase the electrical modulation bandwidth; yet, this has nothing to do with chaos bandwidth, which may become the main impediment to high-speed secure transmission. This may result less appealing in terms of a practical application; however, it is important to recall that the long-infrared operating range is mainly attractive for military applications, where the primary scope is privacy rather than speed.

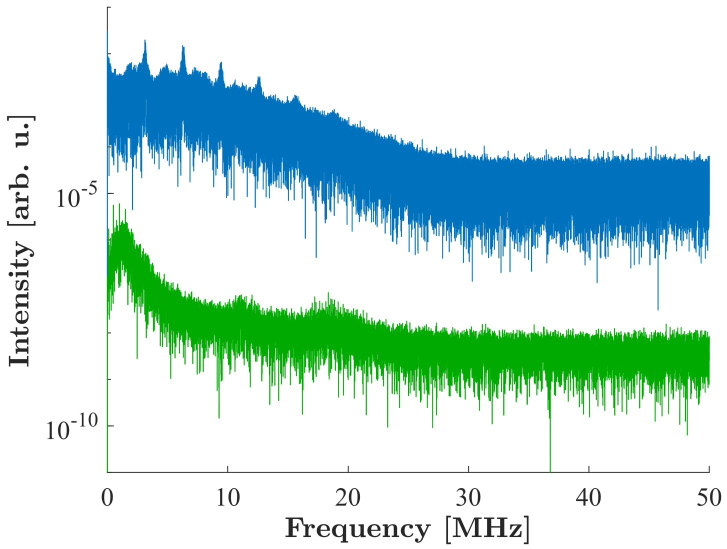

Figure 5.9: Comparison of chaos bandwidths at 9 µm (blue trace) and 5.6 µm (green trace, vertically translated for the sake of clarity)

.

Certainly, greater efforts can be done for a bandwidth enhancement: as an instance, both optical feedback and optical injection can be concurrently exploited; especially in the case of QCLs, this may disclose as particularly advantageous not only for a broadband chaos, but for the chaos onset itself. In fact, QCLs are renowned to be quasi-class A lasers, even if they are of the semiconductor type.
Finally, deeper investigations must be conducted to ascertain which parameters have major influence on the QCLs nonlinear dynamics. Therefore, only a key to the observed phenomena is provided here, but confirmation from theoretical and experimental perspectives is still awaited. In fact, additional studies may reveal

a possible dependence of the QCLs' chaos bandwidth on particular parameters. As an instance, the remarked difference between the QCLs under study could be attributed to a different structure of the compared devices.

5.3 Injection locking

To achieve chaos synchronization between the master and the slave, it is necessary to satisfy the injection locking condition [144], which consists in the synchronization of the lasers' carrier frequencies, thanks to the frequency-pulling effect. This process is strictly dependent on the bias current's values, as well as on the temperature of the lasers, both causing a shift in wavelength of the lasers' emission spectrum. In fact, Figure 5.2 and Figure 5.3 evidently show the emission wavelength's dependency on the bias current. For both the ML and SL, it is noticeable that the higher the bias current, the more the emission wavelength is shifted towards the long-infrared range.
In order to lock the SL to the ML, the ML is modulated through a sinusoidal waveform around the set bias current. The latter is properly chosen to be below 380 mA, expected limit for the ML's monomode operation. Indeed, it is still possible to synchronize the two lasers even if the master laser enters the FP regime. Nevertheless, a multi-mode excitation leads the output power of the transmitting laser to be distributed among the excited modes, which we assume to be detrimental for a good synchronization between the devices.
As concerns the sine modulation, its amplitude is fixed according to the bias current value, in order not to go below 0 mA, dangerous for the correct operation of the ML. The frequency, instead, is arbitrarily chosen to let us clearly distinguish on the oscilloscope when the injection locking is obtained.
Figure 5.10 exactly represents this situation: the orange peaks are those visualized at the receiver side when the carrier frequencies are synchronized. We can notice these peaks fall only in correspondence of certain voltage values of the ML sine modulation, corresponding to a specific value of bias current as well. In particular, the peaks are maximized for a well-defined value of SL bias current; nevertheless, as depicted in Figure 5.11a, it belongs to a range of currents allowing for a less-perfect locking of the carriers. Within this interval, less intense peaks are visible. Of course, the synchronization improves as the emission wavelengths are better overlapped.
Injection locking does not require the lasers to have the same currents and temperatures. In the example here reported, the SL bias current is slightly above threshold: a high bias current does not necessarily improve the quality of synchronization.
When the optical injection takes place and chaos synchronization is achieved, the optical spectrum of the slave reproduces the one of the master, showing the master's chaotic patterns as well. Before the optical injection process, the slave QCL is not

chaotic because it is not in an external cavity configuration. Because of the chaos pass filtering effect, the slave synchronizes only with the master chaos.

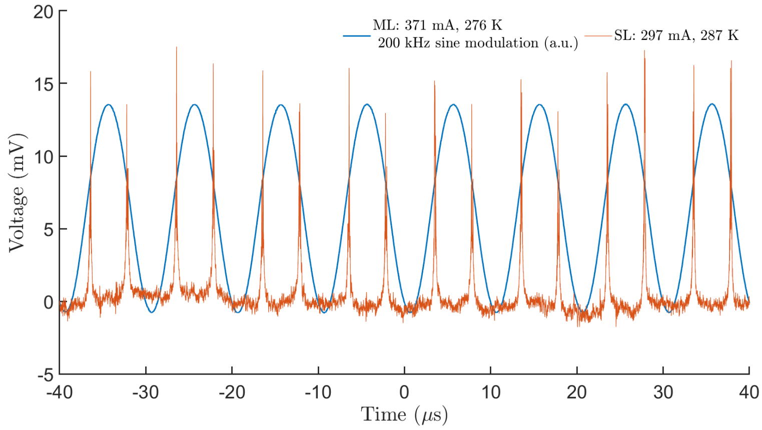

Figure 5.10: ML (in blue) and SL (orange) timetraces during injection locking. The ML is biased at 371 mA, at 276 K. The SL is biased at 297 mA, at 287 K. The orange peaks indicate the synchronization of the QCLs' carrier frequencies.

By sweeping the SL bias current, it is possible to find different current ranges where the injection locking is possible (Figure 5.11a). However, we performed this process up to around 410 mA for the slave bias, since as long as the current is further increased, the synchronization becomes more difficult to achieve, obtaining a cross-correlation coefficient not higher than 60%. Therefore, in the range 290 mA-410 mA, three main intervals are noted for meeting the injection locking condition. Figure 5.11a illustrates the cross-correlation coefficient evolution as a function of the slave bias current. Some interesting features can be pointed out:

- The presence of the three intervals means the injection locking can occur with the SL's side-modes too: studies conducted on 5.6-µm QCLs [162] demonstrated how the slave laser turns to be multi-mode when the synchronization is effective, whereas it operates monomode under free-running operation (Figure 5.11b). This is due to the fact that the slave is expected to reproduce both the electrical and optical spectra of the master; because of EOF, the master is driven chaotic, showing multi-modes; when injection locking takes place, the slave turns multi-mode by emulating the master features.
  Specifically, when increasing the injection strength, a second mode is appearing, with a subsequently following third mode. The amplitude of the side-modes increases with the injection strength, while the main mode remains unchanged. This is not surprising, since the broadening of the optical spectrum has been widely observed in semiconductor lasers generating deterministic chaos [118].

Though, there is not the possibility to affirm which is the bias range ensuring injection locking with the main mode; in addition, further studies should be conducted to prove this dependence has an impact on the quality of synchronization.

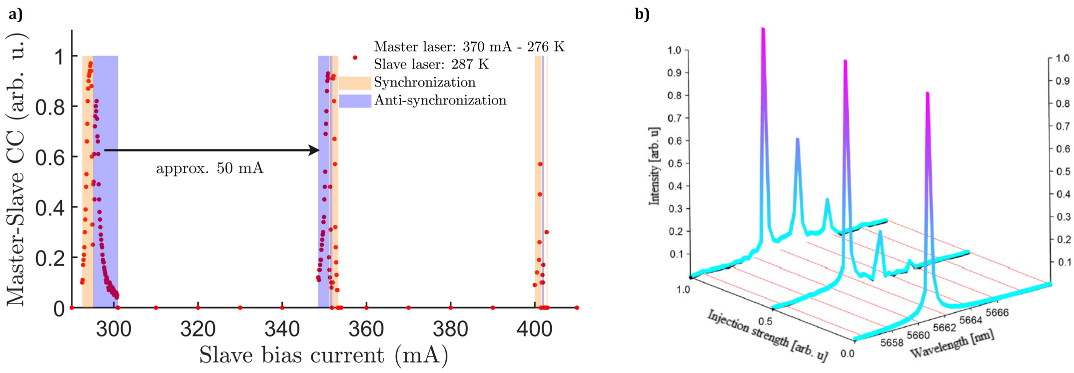

Figure 5.11: (a) Experimental data (red dots) representing master-slave cross-correlation (CC) as a function of the slave bias current. The synchronization intervals are marked in orange; the anti-synchronization ones in blue. The master operating point is 370 mA, at 276 K. The slave one is 287 K, with a bias sweeping from 290 mA to 410 mA. (b) Slave laser's optical spectrum evolution during the coupling process, obtained through a Fourier transform infrared spectrometer (FTIR). The SL is biased at 512.4 mA, for increasing levels of injection from the master laser. Courtesy of [162].

- The injection locking ranges become narrower as long as the slave bias is increased. A possible explanation may rely on the coupling with the side-modes of the slave. These modes are inevitably less intense than the main one (Figure 5.11b), significantly affecting the synchronization quality. This justification implicitly assumes that the first injection locking range, right above the lasing threshold, corresponds to the coupling between the main modes of both the ML and SL, whereas the others occur with the slave suppressed side-modes. This needs to be verified, though.

- The distance between the injection locking ranges is approximately constant, around 50 mA; this is directly linked to the emission wavelength. That is why for 5.6-µm QCLs the esteemed distance was smaller, around 30 mA [162]: the smaller the wavelength, the closer the side-modes, the higher the number of injection locking ranges it is possible to find. However, this does not impact on the system's performance in terms of synchronization, since we expect the best results when the main modes of both the master and the slave lasers are coupled.

- The first and the second ranges exhibit higher values of cross-correlation, consequently unveiling a better synchronization. As concerns the less-efficient coupling of the third range, a possible explanation may rely on the coupling of the master optical frequency with one of the aforementioned side-modes, resulting in a limited synchronization.

- Each injection locking range shows an interval of current values where the lasers are synchronized, and another interval where the lasers are anti-synchronized: this highlights how a slight modification of the slave bias can favor synchronization with respect to anti-synchronization and vice-versa. Generally, during this transition, there is a drop of the cross-correlation coefficient, which is usually higher for anti-synchronization. Furthermore, apart from the third injection locking range, the anti-synchronization holds for more slave bias values than synchronization.
  Finally, when a new injection locking range is met, the synchronization type is the same as at the end of the previous injection locking range.

Of course, what is reported here is a single example, but this behavior has been observed overall during all the measurements. Anyway, the assumptions here introduced need to be verified by further theoretical and experimental studies, possibly linking the electrical and optical properties of the devices with the physical structure.

5.4 Chaos synchronization

It is worth noticing that anti-synchronization rather than synchronization occurs by modifying the slave laser bias of some fractions of mA (Figure 5.11a). Still, it is not clear which parameters play a major role in determining if the two lasers are synchronized or anti-synchronized. Nevertheless, in our experience, we obtained a better transmission quality when anti-synchronization took place; hence, we will focus on the analysis of this specific case. This finding is also in line with Spitz's observations at 5.6 µm [121].
Once the two QCLs are synchronized, the quality of transmission is evaluated with correlation diagrams and eye diagrams. In the following, we report the achieved results for different data rates: 1 Mbps, 5 Mbps and 8 Mbps. In this section, the target is the characterization of the (anti-)synchronization quality; the effective evaluation determining the achievability of secure communication is instead the core of next section. Though, this section and the following refer to the same timetraces, for the same values of data-rate.

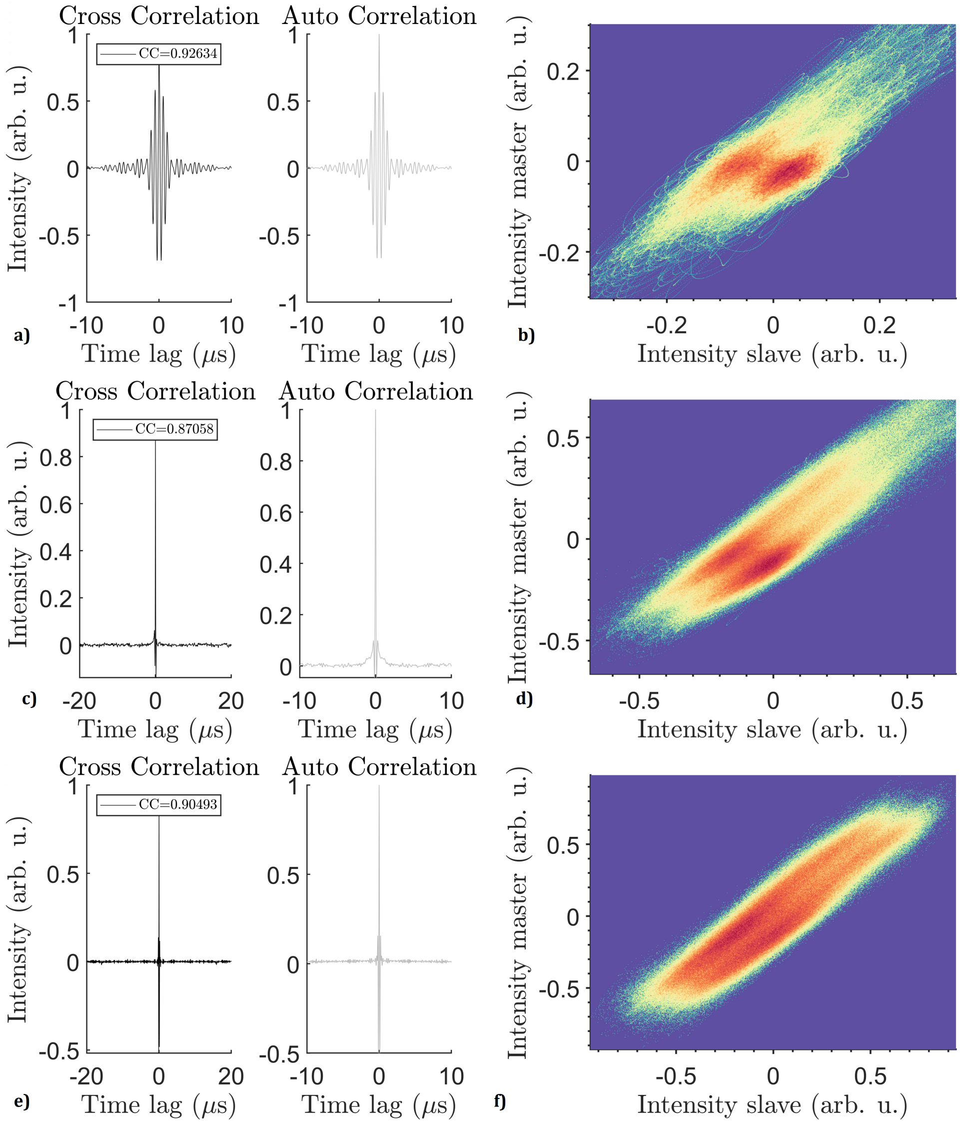

Figure 5.12: (a, c, e) 1D cross-correlation and auto-correlation diagrams for the filtered intensity of the slave and the master QCLs. The filtered intensity of the slave laser was flipped in order to have a theoretical maximum value of 1 for the cross-correlation diagram. (b, d, f) 2D Correlation diagram for the intensity of the ML (y axis) and SL (x axis). The signal of the slave is flipped to have a positive correlation, being the lasers anti-synchronized. Message data-rate: (a, b) 1 Mbps, (c, d) 5 Mbps, (e, f) 8 Mbps.

In signal processing, the cross-correlation function objectively compares different time series and allows to see how two signals match and where the best match occurs. The 1D cross-correlation diagram is obtained through an iterative process, consisting in the calculation of a correlation coefficient as a function of the lag between the timetraces of the master and the slave. The lag with the highest correlation coefficient is where the two series match the best. The higher the cross-correlation coefficient, the better the quality of synchronization. In 1D cross-correlation diagrams, the correlation intensity between the two timetraces is represented as a function of the time. In Figure 5.12c and Figure 5.12e, the correlation peak occurs for a single time lag, corresponding to the time of flight between the master and the slave: even if the message sequence to be transmitted is periodically repeated, there is no dependence on any previous chaotic outcome, and this is expected for private operation. In Figure 5.12a, pronounced side-lobes are present. The peak value of the CC coefficient is higher than in the previous examples (92% vs 87% and 90% respectively), but the periodical repetition of the message somehow influences the chaos generated by the master, constituting a threat to the security of transmission.

The auto-correlation is very similar to the cross-correlation, but the signal is correlated with itself, to detect repeated patterns. In this graph, the presence of side-lobes can reveal a certain periodicity in the generated timetrace. Instead, a good chaotic waveform is that whose auto-correlation presents a main lobe as narrow as possible, and suppressed side-lobes. The auto-correlation peak appears reasonably for a zero time lag.

In the 2D-correlation diagram, indeed, the intensity of the master is represented on the y-axis, that of the slave on the x-axis. A good synchronization allows us to visualize a straight line with 45° positive slope. Actually, since anti-synchronization is experienced, a negative correlation is measured. However, the signal of the slave is flipped to have a positive slope.

In the following, we report the master's and slave's chaotic timetraces and bandwidths, when synchronization is achieved. The examples in Figure 5.13 and Figure 5.14 are the same of Figure 5.8. Being the operating point the same in the three examples, it is clear how the cross-correlation value is highly influenced by the shape of the chaotic bandwidth. The cross-correlation is observed to be higher when strong frequency peaks pop up, as that around 5 MHz. As long as its intensity becomes less pronounced, the maximum CC coefficient drops, as emerges from Figure 5.14b, Figure 5.14e and Figure 5.14c, Figure 5.14f. Specifically, when the bandwidth is completely flat (Figure 5.14c, Figure 5.14), the cross-correlation dramatically deteriorates.

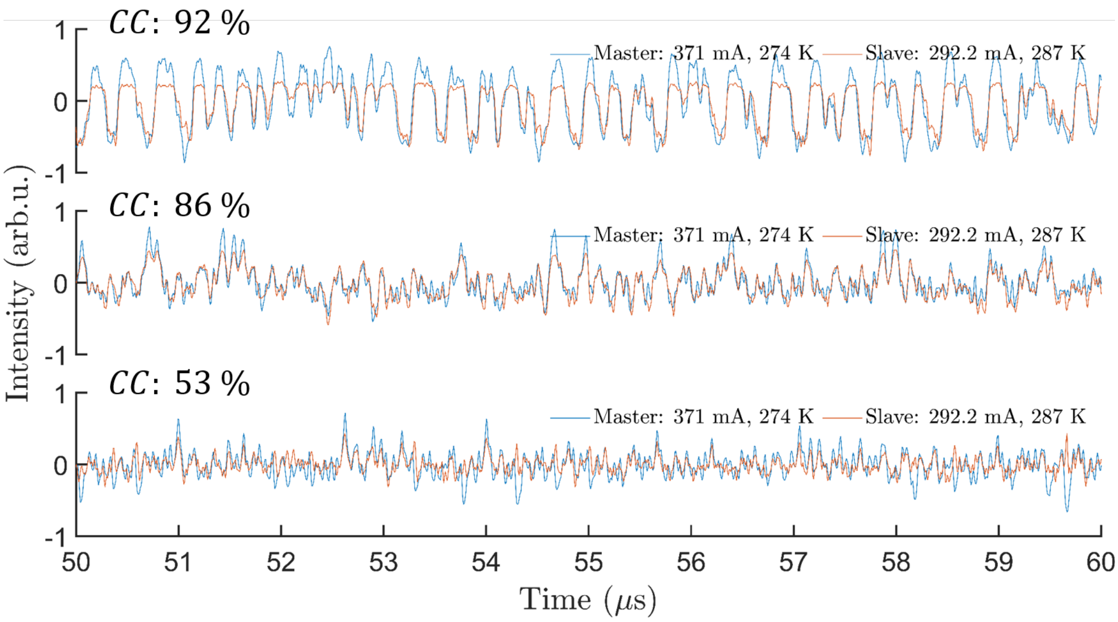

Figure 5.13: Experimental chaos timetraces of master (blue) and slave (orange) lasers, for a measured CC value of respectively 92%, 86%, 53%. The operating point is 371 mA, 274 K for the master; 292.2 mA, 287 K for the slave. The concealed message is PRBS-7, with 1 Mbps data-rate.

Some considerations may take into account the higher power peaks that are reached when strong frequency components are detected; some others may focus on the presence of the frequency component itself in the spectra: it may be easier for the slave to lock and synchronize with the master under these conditions; this is not surprising: the presence of some frequency components implicitly involves a kind of periodicity in the chaotic fluctuations. Yet, synchronization was firstly observed between coupled periodic oscillators [138]; only later, the possibility of chaos synchronization became plausible.
For a similar reason, we can explain the presence of the message on the slave side too. In fact, for the chaos pass filtering effect, we expect the slave to reproduce only the chaotic fluctuations of the master. This is still true, but it is valid if the message is well concealed in the chaos, both in terms of amplitude and bandwidth. As especially Figure 5.14d-Figure 5.14f depict, the master's chaos is not fully covering the PRBS-7 at low-frequencies; this means the message is not negligible and consequently be considered as only a small perturbations to the chaotic fluctuations. In the meantime, this does not imply the perfect reproduction of the message at the slave's output; in fact, it is later demonstrated that the system performances still meet the communication standards.

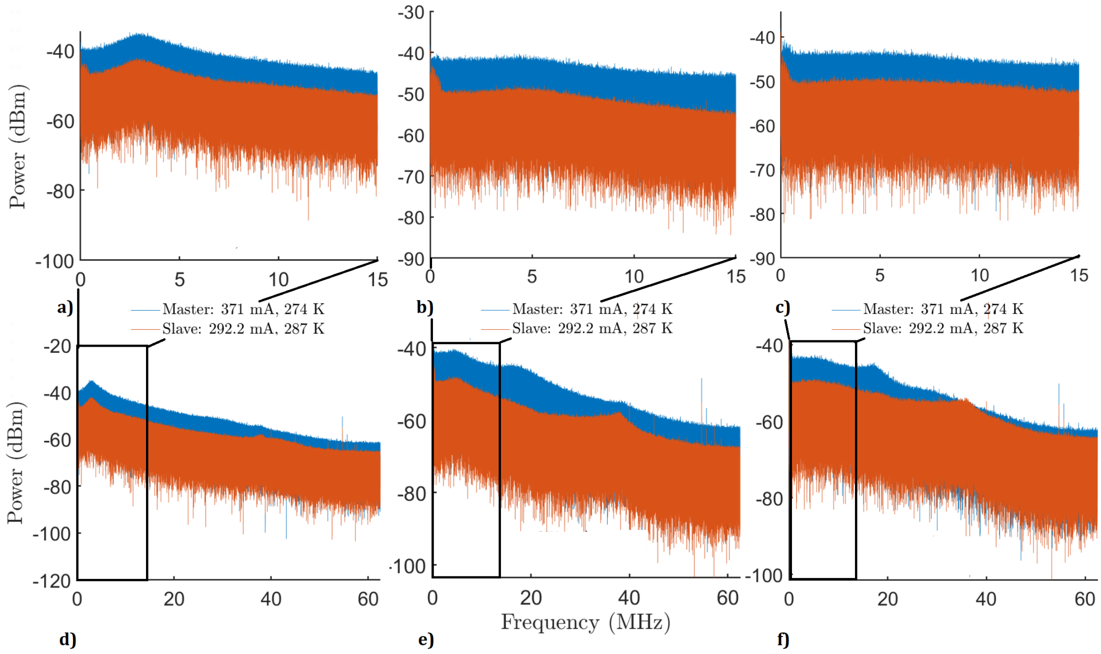

Figure 5.14: Experimental chaos bandwidths of master (blue) and slave (orange) of (top panel) 15 MHz and (bottom panel) 50 MHz, respectively. The operating point is 371 mA, 274 K for the master; 292.2 mA, 287 K for the slave. The concealed message is PRBS-7, with 1 Mbps data-rate.

Conclusively, it is appreciable from Figure 5.13 how the stronger peaks on the master are smoothed on the slave side. This is foreseeable, since any kind of transmission comes with additional noise, impacting on the overall system. Hence, this justifies the smaller power intensity of the slave, together with the fact that the slave laser is itself less powerful than the master, as Figure 5.5 outlines.

5.5 Secure communication

As emerges also from Figure 5.15, the receiver end must perform different post-processing operations for the message recovery, the signal quality improvement and performances evaluation.

5.5.1 Filtering

The recovery process begins with the filtering of the master (containing the message) and of the slave signals. The filtering process is assessed by a custom Matlab program: it implements a finite-impulse response (FIR) passband filter, in order to be able to get rid of both the noise at high frequency and low frequency. To do so, we take into account that the MCT are not able to detect the frequency components below 0.25 MHz. The passband and stopband high frequencies are properly modified according to the data-rate of the enciphered message. Cutting-off frequency components below the data-rate value would eliminate important information for the reconstruction phase. Meantime, 3-dB bandwidths much broader than the data-rate would include high-frequency noise components, disturbing again the reconstruction process. Table 5.1 summons the characteristics of our filter.

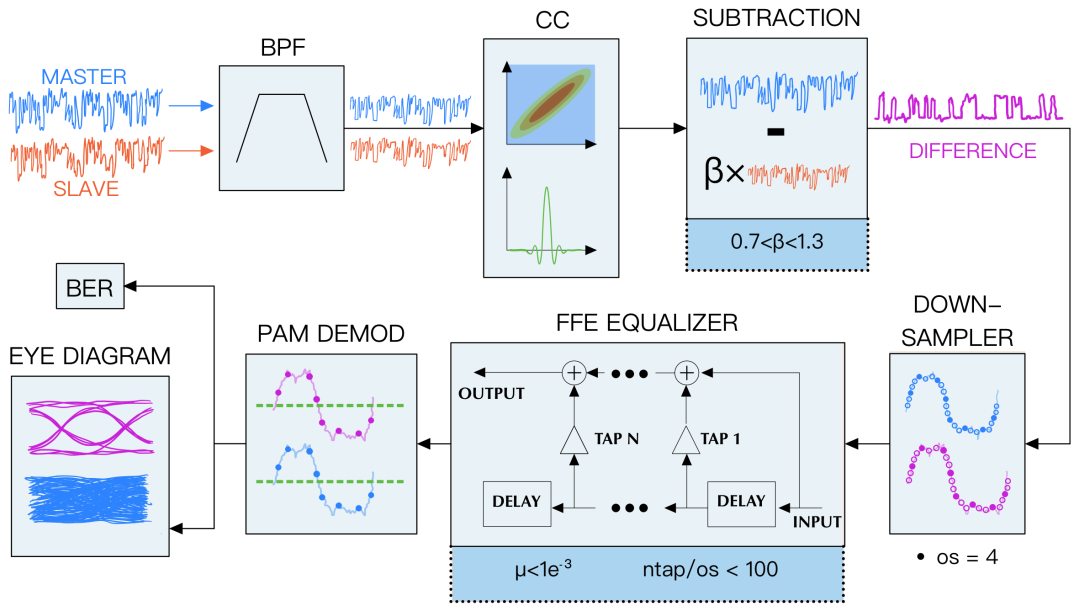

Figure 5.15: Block diagram of post-processing operations at the receiver end for the message recovery and system performance evaluation. BPF: band-pass filter; CC: cross-correlation; FFE: feed-forward equalizer; PAM: pulse-amplitude modulator. β: multiplication factor; os: overshoot factor; μ: FFE converge factor; ntap: number of taps in FFE.

5.5.2 Subtraction

After filtering, the reconstruction of the message M(t) is realized by computationally evaluating the difference intensity of the chaos transmitter $I_{ct} = |E_{master} + M(t)|^2$ and the intensity of the chaos-synchronized slave $I_{cs} = |E_{slave}|^2 \approx |E_{master}|^2$, resulting in $I_{ct} - I_{cs} = 2\Re(E_{master} \cdot M(t)) + |M(t)|^2$.
The custom Matlab program involves the use of a multiplication factor, namely β, whose value belongs to the range [0.7, 1.3], with a 0.015 step. It has been chosen according to the observations of master and slave chaotic timetraces; in fact,

it is a coefficient used for obtaining waveforms with almost the same amplitude, before executing the subtraction. It is not possible to fix β a priori, because each measurement differs from the others, for the intrinsic concept of chaos. The several difference timetraces are then stored because they reveal useful in the next steps, for the evaluation of the system performance. Indeed, when computing the BER, this operation will be performed for all the β values, in order to find the best result, and, consequently, the best multiplication factor.

Parameter	**Value**
Passband low frequency	0.250 MHz
Passband high frequency	Data-rate
Passband ripple	0.1 dB
Stopband attenuation	60 dB
Stopband low frequency	0.137 MHz
Stopband high frequency	Data-rate + 0.113 MHz

Table 5.1: Characteristics of the passband filter applied to the master and slave signals before subtraction.

5.5.3 Downsampling

The number of points per bit is given by the ratio of the sampling-rate over the message data-rate. The sampling rate is fixed at 250 MSamples/s, whereas the data-rate depends on our choice. If the data-rate is 1 Mbps, the number of points per bit will be 250.
In order to speed up the processing, it is necessary to decrease such a high value by downsampling. The overshoot factor is set to 4, since it is regarded as the best compromise between speed and resolution. It could have been possible to further speed up this operation by taking a single point per bit; nevertheless, this would deteriorate the results. Hence, even if we downsample, the overshoot factor has this name since we are still oversampling each bit, in order to enhance the intersymbol interference (ISI) caused by noise.

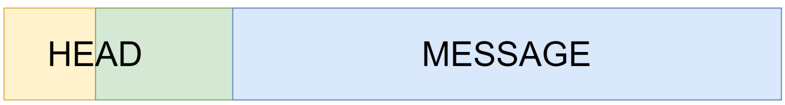

Figure 5.16: Sketch of a transmitted packet in digital communication.

5.5.4 Equalization

After the message reconstruction and downsampling, before the performance evaluation is carried out, a feed-forward equalization (FFE) is performed to improve the signal quality. Equalization is indeed a set of techniques for compensating the degrading effects of transmission paths. It is renown that the channel introduces intersymbol interference, as well as some random noise (from thermal effects) and maybe some crosstalk or electromagnetic interference. The equalizer can thus correct much of the degradation caused by the channel, but it cannot correct the noise. This improves not only the BER, but also the openness of the eye diagram. In terms of implementation, FFE looks for all intents and purposes like a digital FIR filter, as emerges from Figure 5.15. Three main blocks can be recognized in an FFE equalizer: the delay block is needed to obtain time-delayed versions of the input data signal. The higher their number, the more precise, yet the slower the equalization. The taps are represented by coefficients, apposite designed for the considered application, in order to build the best system possible. In fact, when communication is established between two parties, the packet which is sent is not only constituted by the message, but a head is also present (Figure 5.16).

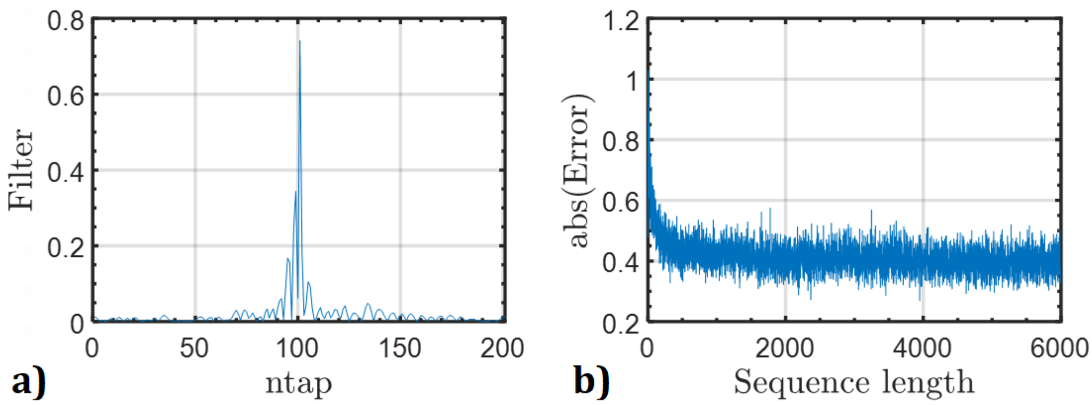

Figure 5.17: (a) Taps impact on the FFE performance. (b) Error converge with ntap=100.

In turn, the head is subdivided into two main parts: some initial bits, sent by the transmitter to communicate to the receiver that the transmission is beginning (in yellow); a sequence of bits, previously shared by the two parties (in green). The receiver compares the one sent by the transmitter to that available on its side, in order to design the equalizer, reducing the number of errors caused by transmission, enhancing the system performance. Hence, the need of finding the best solution space with varying number of FFE taps and converter resolutions. Figure 5.17a considers a maximum number of 200 taps; the 100th is the reference: taps from

0th to 99th represent the points after the reference; those from 101th to 200th the points before. The different taps have not the same weight, impacting the value of the taps coefficients: the most influential are those in proximity of the reference, within an interval of around 16 taps on the left and on the right.
In our case, each bit is oversampled (os=4), meaning consecutive taps relate to different points of the same bit. So, if we want to consider the 100 bits close to the reference, ntap must be equal to 400: 400 is the number of taps, 4 is the number of points per bit; therefore, 400/4=100 bits.
By choosing a number of taps (ntap) of 100, the esteemed error convergence is represented in Figure 5.17b, choosing an error convergence factor $\mu < 10^{-3}$. The smaller μ, the higher the precision, the slower the equalization. Likely, the higher the number of taps, the faster the converge to the required error.

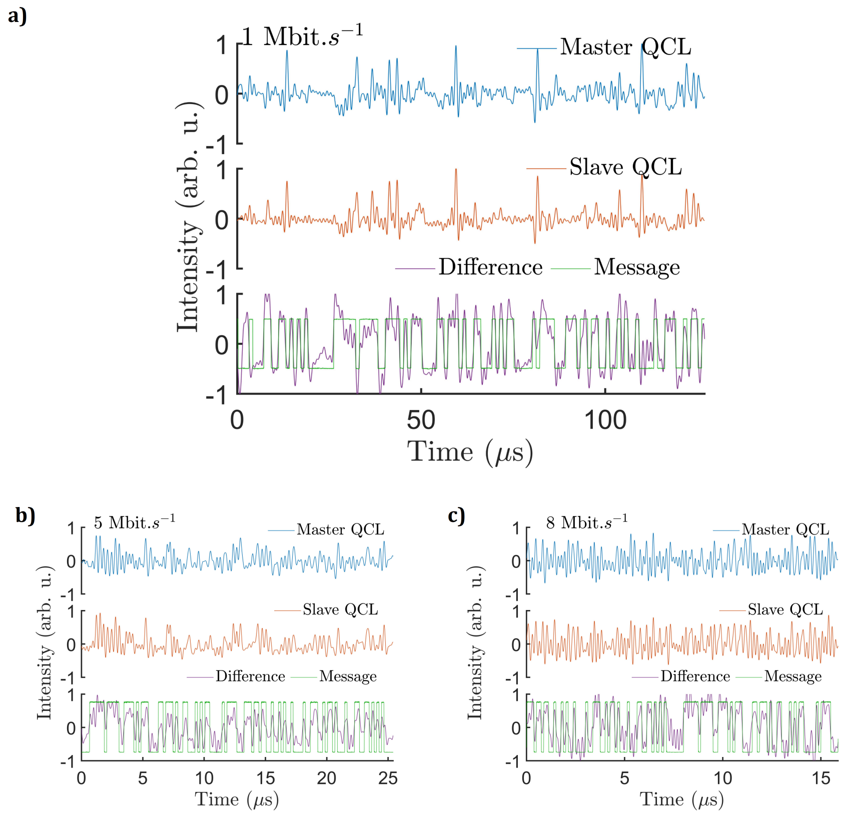

Figure 5.18: Experimental timetraces for (a) 1 Mbps, (b) 5 Mbps and (c) 8 Mbps data-rate transmission: (blue) master, (orange) slave, (green) original message, (purple) difference.

5.5.5 Demodulation

Equalization is then followed by pulse-amplitude (PAM) demodulation: the message information is encoded in the amplitude of the retrieved message. Hence, demodulation is performed by threshold detection. Channel impairments during transmission, filtering optimization and equalization efficiency have an impact on the estimation of the correct bit.

5.5.6 Performances evaluation

After the demodulation, it is possible to evaluate the system performances by means of the BER and the eye diagram. In this section, the results attained for the different data-rates are provided. The bit error rate (BER) is the number of bit errors over the number of bits sent. The BER is commonly expressed as ten to a negative power. Over a communication channel, the received bits may be altered due to noise, interference or distortions. It is important to keep this value as low as possible, in order to have an effective communication. Different transmission links and communication types demand for more or less stringent BER requirements. The communication standard sets the BER threshold to 4% for those applications whose latency specification is not that severe. This would mean the implementation of more complex forward-error-correcting (FEC) algorithms, calling for larger overheads, and consequently latency. This perfectly fits our application. The advantages of mid-infrared free-space optics have been abundantly discussed in chapter 1; however, beam scintillation, spreading, wandering and turbulence may still cause laser beam degradation during propagation. Studies have demonstrated how the BER can be influenced considerably by the atmospheric impact [163], together with the laser beam size and the wavelength. A general trend reveals that BER decreases with the increase of the transmitted signal power. Meanwhile, BER performance will improve if a narrow beam width is used: in fact, the received signal power is increased when a narrow beam width is used [164]. Furthermore, the average BER will increase with the transmitted distance enlarging; this happens mainly for two reasons: first of all, bigger distances turns into higher noise levels, interferences and so signal degradation. Likewise, longer distances induce a major beam modification because of the aforementioned atmospheric phenomena. A possible way for performance enhancement would be the use of adaptive optics [165]. However, in the mid-infrared domain, the availability of this equipment is only now starting to be less critical than it was in the past. New technologies and research advancements have indeed coped with the several issues determined by the infrared, enabling the fabrication of high-quality devices.

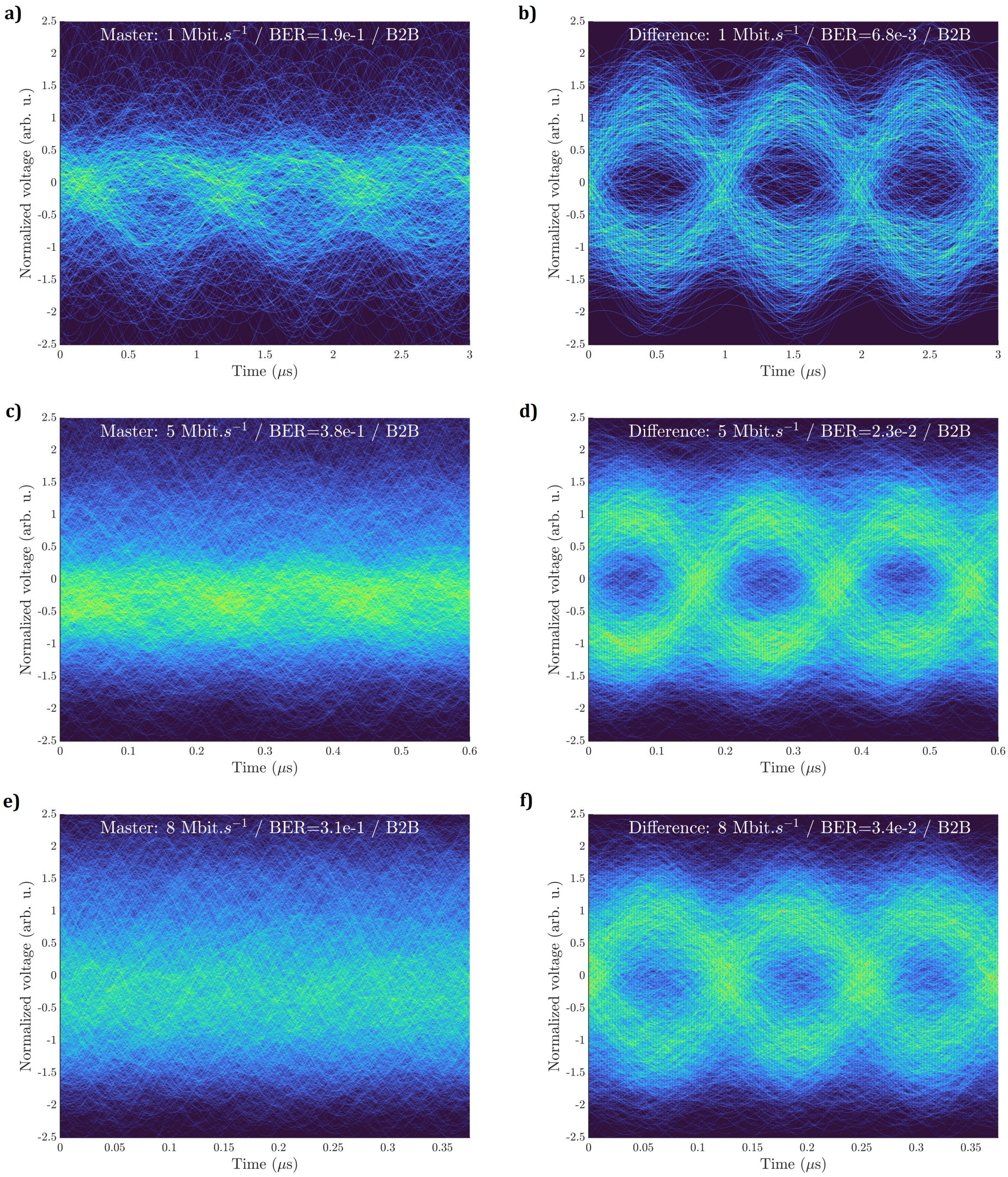

Figure 5.19: Experimental (a, c, e) master eye diagram and difference eye diagram (b, d, f) for (a, b) 1 Mbps, (c, d) 5 Mbps and (e, f) 8 Mbps data-rate transmission.

In our experience, low signal power and beam divergence constitute two of the main obstacles for accomplishing our goal. As previously noted, the supplied QCLs have not high output power levels; in addition, because of the beam-splitter presence, the intensity of the transmitted beam is further reduced. Another problem

concerns the imperfect collimation of the beam, due to the use of MIR discrete components, the complex installed setup and the intrinsic properties of free-space optics.
The eye diagram is used in conjunction with the BER to verify the quality of signal transmission. It takes its name from the fact that it has the appearance of a human eye. It is the superposition of all the bits on the same time interval, equal to the inverse of the data rate. The eye diagram is employed to reveal whether there are faults that garble the transmission, causing, for example, the reception of a zero when a one has been sent. This is possible by evaluating the eye openness. Generally, the forenamed atmospheric phenomena and transmission issues are involved in determining the eye openness; as an instance, a higher bit-rate always translates to a vertically smaller eye opening. By observing Figure 5.19, some general remarks can be pointed out. The communication standard accepts master BERs of 25 % as the lower limit commonly accepted for a non-decipherable transmission [166]. In fact, the master signal is that an eavesdropper would get, provided it disposes of the best-matching filter. This is very unlikely, since the eavesdropper does not share the private keys with the transmitter and the receiver. These keys are the physical parameters of the devices, matched to the best extent because taken from the same wafer just after their fabrication. Therefore, an eavesdropper can easily retrieve a message with a high probability if it possesses a device responding to these demands. Table 5.2 assembles the principal results. A

Data-rate	**CC**	**Master BER**	**Difference BER**
1 Mbps	92 %	19 %	0.7 %
5 Mbps	87 %	38 %	2.3 %
8 Mbps	90 %	31 %	3.4 %

Table 5.2: Summarizing table reporting the main experimental results

master BER of 19% is at the limit of the commonly accepted lower threshold for the previous considerations. This value can be explained by looking at the shape of the related 1D-correlation diagrams (Figure 5.12a). With respect to the other examples, the master timetrace for 1 Mbps shows a certain dependence on the previous chaotic outcome, because of the presence of the pronounced side lobes. This is not related to the data-rate used, but mainly to the chaotic waveform that the master was producing during the measurements. The message was not perfectly hidden within the chaos, either for its amplitude or for the small complexity of the chaos. Moreover, the message sequence was periodically repeated, being a PRBS-7. It becomes then easier to retrieve the message, even for an eavesdropper. This also translates into a wider openness of the master eye diagram. A smaller master

BER does not only entail downsides. The difference eye diagram is completely open, and in fact we measure a difference BER of 0.7%. This is comparable to those standards requiring a BER of 0.4% to use a FEC decoder with a maximum overhead of 7%. This opens the possibility to apply chaos-based communication also in those fields where latency requirements must be necessarily satisfied.

These considerations do not hold true for 5 Mbps and 8 Mbps examples, resulting in BERs still suitable for an error-free transmission because smaller than 4%, yet not under the unity. A possible explanation is linked to the increasing data-rate, causing the message to be more easily detectable. Besides, as already implied, the master BER is more interconnected to the complexity of the chaotic output and the quality of the message enciphering. In fact, for 5 Mbps and 8 Mbps, the master eye diagram is completely closed. This was predictable by observing the 1D cross-correlation diagram, characterized by a single intense peak in correspondence of the time lag between the master and the slave. Consequently, also the related BER is much higher than 25 %, granting for privacy. It is also worth noticing that there is not a defined dependence of the BER (i.e. system performance) on the cross-correlation coefficient. Our observations allow us to sustain that a cross-correlation coefficient higher than 85% implies a good quality of synchronization. Nevertheless, this is not sufficient for achieving a secure communication satisfying the performance demands. In fact, cross-correlation coefficients of 94% have been also measured; still, the BER revealed too high for the communication application. As a matter of fact, the reported results confirm that it is not true that the higher the cross-correlation coefficient, the smaller the BER. As an instance, the BER for 8 Mbps transmission is 3.4% with a cross-correlation coefficient of 90%. Besides, with a 5 Mbps transmitted message, the cross-correlation coefficient is 87%, but the BER is lower, around 2.3%. However, we may reasonably suppose that higher data-rates require higher values for the cross-correlation coefficient in order to achieve satisfactory values for the BER. It is in fact certified that higher bit-rates could result detrimental for the system performances.

Concurrently, the message amplitude played an essential role when increasing the data-rate for achieving the desired BER limit. A clear relationship between these two parameters is not available, but it is evident that an increase in the message amplitude causes a decrease of the BER since the message is less hidden within the chaotic patterns. On the one hand, this facilitate decryption; on the other hand, this negatively impacts on security. Certainly, further investigations may enlighten new features and parameters relationships, suggesting for additional improvements.

5.6 Herriott cell

After the promising results with lasers at a distance of one meter from each other, we went further by complicating the setup through the addition of a multipass cell of the Herriott-type. Multipass cells are used primarily for weak-trace-gas absorption spectroscopy applications such as environmental monitoring, combustion processes, medical diagnostics, and fundamental atomic and molecular physics. Compared to other long-optical-path absorption cells, such as the White cell, the Herriott cell is more stable to small perturbations. The major advantages of the Herriott cell are that it provides a relatively long absorption path in a compact design and that it is much simpler than high-finesse optical cavities (which would typically require spatial mode matching, precise optical alignment, or resonant excitation). Specifically, we made use of a Herriott cell (Thorlabs, HC30L), for achieving a distance of 31.2 meters, posing no small challenge in the search for synchronization between the two devices. Moreover, the utilized cell features concave mirrors with protected gold coatings designed for enhanced performance in the MIR.

Figure 5.20: Herriott cell HC30L by Thorlabs

.

The insertion of the cell was not enough to perform the communication, though. First of all, its presence requires the need to increase the power of the transmitted beam, since the distance to travel is longer, so higher losses and noise levels are experienced. In the meantime, however, we were already working at the current limit for ensuring the monomode operation of the master laser. Thus, the only available solution was to exploit the beam splitter to reflect the 35%, and transmit the 65% (contrarily to what we were doing without the Herriott cell). Of course, this led to further problems in generating chaos, having decreased the amount of feedback re-injected in the internal cavity, further reduced by the substitution of a gold mirror with a silver one (Thorlabs, PF10-03-P01). Indeed, a higher stability in the output waveform and spectrum was observed. Thus, to cope with it, we decreased the length of the external cavity to 8 inches, corresponding to 20.32 cm.

In addition, we lowered the master temperature, setting it at 273 K (0°C), rather than 276 K (3° C).

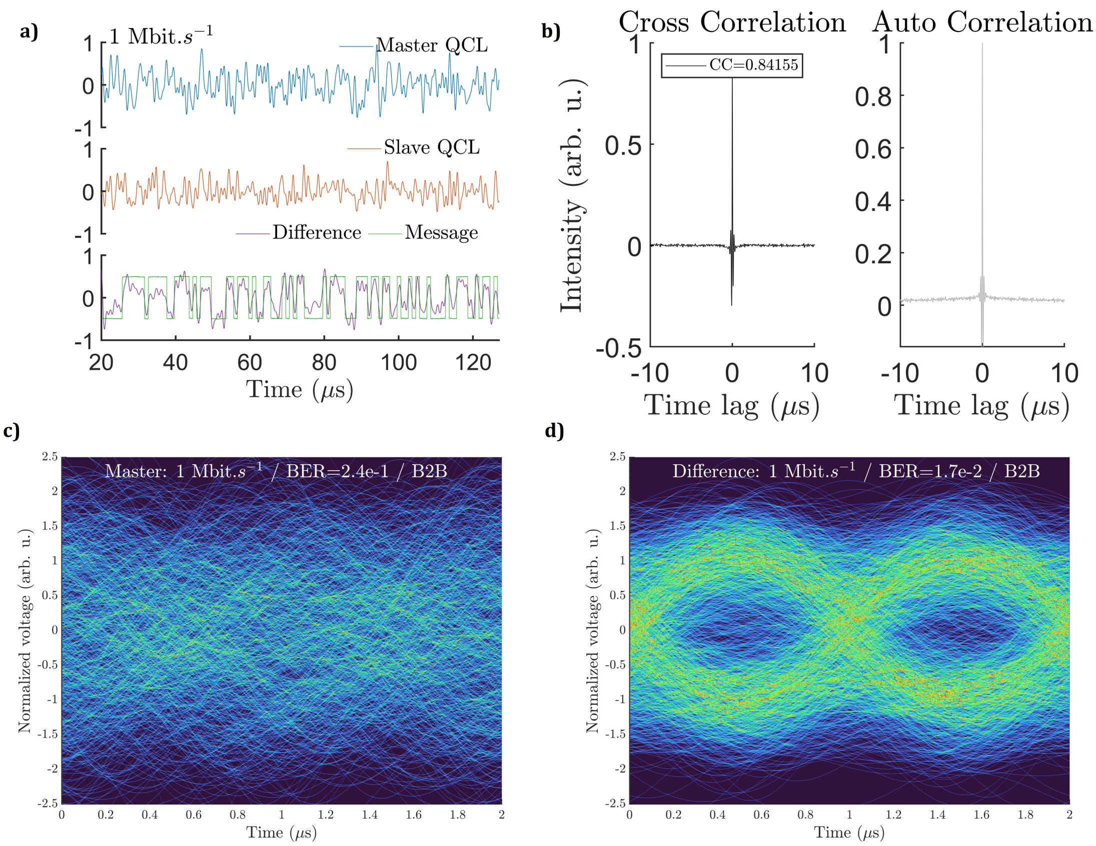

Figure 5.21: Experimental results for 1 Mbps data-rate transmission; with Herriott cell: (a) Experimental timetraces: (blue) master, (orange) slave, (green) original message, (purple) difference. (b) 1D correlation diagrams for the filtered intensity of the slave and the master QCLs. The filtered intensity of the slave laser was flipped in order to have a theoretical maximum value of 1 for the cross-correlation diagram, being the lasers anti-synchronized. (c,d) Experimental master eye diagram and difference eye diagram.

.

Different attempts were made, some without the isolator, assuming that the 31.2-meter distance was enough not to have mutual coupling between the two lasers. These considerations proved totally wrong, demonstrating how essential the isolator is for unidirectional coupling.
Finally, to improve the beam divergence and shape, we needed to add a telescope and two additional mirrors, moving from a 6-mirror configuration of the previous

set-up to a 8-mirror one. The telescope consists in two equal MIR lenses correcting for the beam divergence and collimation. It was placed after the Herriott cell, where the travelled distance makes this characteristics more critical. As concerns the 8-mirror configuration, 4 mirrors were utilized before the cell to enhance the beam alignment through the isolator; the remaining ones were placed after the telescope, to inject the transmitted beam as better as possible in the slave's active area.
In the following, we report the achieved results for 1 Mbps, exploiting the usual figures of merit and communication standards. This experimental data demonstrate

Data-rate	CC	Master BER	Difference BER
1 Mbps	84 %	24 %	1.7 %

Table 5.3: Summarizing table reporting the experimental results with Herriott cell

it is possible to accomplish a private communication even if the distance increases, without any detrimental effect neither on the cross-correlation coefficient, nor on the master and difference BERs. However, the transmission at 5 Mbps and 8 Mbps turned out to be more complex, not in terms of cross-correlation, but in terms of BER. Indeed, values around 83%-90% resulted not enough for obtaining a difference BER $< 4\%$ (even if very close to it, around 6% with 5 Mbps of data-rate). Nevertheless, some adjustments can be performed on the experimental setup to meet satisfying results.
Anyway, this is a further step towards a practical real-field experiment, that would represent a turning point in the private communication based on the chaos generated by QCLs.

5.7 Conclusions

We demonstrated a proof-of-concept of free-space chaos-based secure transmission with quantum cascade lasers emitting in the long-wave infrared thermal atmospheric window. The success of the transmission relied on chaos anti-synchronization, measuring a maximum cross-correlation coefficient as high as 92% for the reported measurements. Values up to 97% were reached; yet, the almost perfect anti-synchronization still proved insufficient for accomplishing an efficacious secure transmission. The insertion of the Herriott cell did not result detrimental for a good synchronization, yet more challenging in terms of experimental setup and system performance. In fact, a secure error-free transmission has been demonstrated at 1 Mbps, but major effort is needed to prove it for 5 Mbps and 8 Mbps.

Because of electrical modulation constraints, the message enciphering was limited in terms of maximum achievable data rate, up to 8 Mbps. In this case, a BER of 3.4% has been achieved. Improvements must be realized to comply with more strict communication standards, considering a transmission as error-free if the BER is lower than 4.7×10^{-3} with forward error correction (FEC) with 7% overhead. Future works may consider the implementation of such an algorithm to enhance the system performance. The latter may be also augmented by modifying the message enciphering technique, studying how the encoding technique impacts on the quality of transmission. In the case true CMo would effectively enhance the BER, a trade-off between it and the current enciphering technique must be done, since CMo experimental implementation is much more complex.
The data-rate can be improved expanding both the electrical modulation bandwidth and the chaos bandwidth; the former depends on the heterostructure, so a preliminary good choice in terms of design parameters is of paramount importance for reaching the GHz range. The latter can be broadened exploiting external optical feedback in conjunction with optical injection: this combo proved useful for other semiconductor lasers. However, a deeper analysis on QCLs' nonlinear dynamics may propose new ideas. Finally, the demonstration of private transmission with the insertion of the Herriott cell proved successful, enforcing the attainableness of a real-field experiment.

Chapter 6

Conclusions and perspectives

This dissertation reports the first proof-of-concept of free-space chaos-based secure communication in the long-wave-infrared range, through the use of quantum cascade lasers with emission wavelength in the second atmospheric thermal window (9.33 µm). There are several theoretical considerations underlying this work. First, free-space optics is a line-of-sight technology with multiple applications: security, military, but especially telecommunications. As for the latter application, it has several advantages over the now established fiber optics. Among the main ones, certainly we can include not needing to have a pre-existing infrastructure, which allows for cost reduction; but also the lack of a defined standardization, so it can offer higher bandwidths. The main disadvantages of this form of communication, however, are very influential on system performance. For long-distance terrestrial applications, the principal limiting factors are beam dispersion, atmospheric absorption, rain, fog, snow, interference from background light sources (including the sun), shadowing, pointing stability in wind, and pollution. This is true if one considers wavelengths in the NIR range, which now belong to the telecommunication standards. If, however, we move to longer wavelengths, in the mid- and far-infrared, it becomes possible to abate these detrimental factors.
It is precisely in this context that the quantum cascade lasers we use come into play. Based on a superlattice heterostructure, these devices allow the emission of wavelengths in the mid- and long-infrared (2.6-20 µm) and terahertz range (60-150 µm, or 2-5 THz). This is possible because they are unipolar sources, in which photon emission results from intersubband transitions, within the same conduction band. Consequently, the emission wavelength is determined by the choice of the heterostructure parameters. This versatility allows QCLs to be used in so many applications: surgery, countermeasure systems, frequency combs generation,

high-precision spectroscopy, military and telecommunication applications. Our experience straddles precisely between the last two fields, these wavelengths being particularly appealing for the secure transmission of information. Recent studies have shown how these mid-infrared sources could be a great potential in the mid-IR and LIR FSO systems for the future 6G era [167]. However, compared with other FSO systems, particularly the ones operating in the 1.55 µm telecom band, the technology readiness level of the QCL-based approach is still far behind.
Our application, however, is in an even different context, as it is dictated by the need to implement a secure form of communication in the mid- and far-infrared by exploiting the principles of chaos theory [80]. Discovered by the meteorologist Lorenz in the 1960s, deterministic chaos has since been observed in a myriad of nonlinear dynamical systems, including lasers. Deterministic chaos is synonymous with unpredictability and sensitive dependence to initial conditions; at the same time, however, it differs from stochastic processes, such as noise. Over the years, therefore, mathematical techniques have been developed to discern between chaos and noise, and to characterize the very complexity of the generated chaos. These tools can also be applied for characterizing the chaos produced by QCLs, which are different semiconductor lasers from conventional ones. Because of the absence of relaxation oscillations, these lasers are intrinsically more stable. This means that in order to obtain chaotic waveforms that are sustained and complex, it is necessary to rely on external perturbations, that are more consistent in strength or number. Among these, surely the best option turned out to be the external optical feedback, as has already been demonstrated for other types of lasers. Not only that: in our case, it was noted how the direct modulation of the bias current by the enciphered message allowed for a more robust chaos; the latter, in fact can be seen as an additional degree of freedom, which contributes to make the nonlinear dynamics of these lasers systems more complex. This is true despite the fact that the amplitude of the message is small enough for the chaos to safely conceal the message to be transmitted.
During the course of the experiment, several difficulties were faced; first, it had already been observed that it is easier to observe chaotic patterns at cryogenic temperatures. At the same time, though, this requires the use of bulky equipment, and especially of environmental conditions not at all compatible with normal ambient temperatures. For this reason, through the use of Peltier cooler and dry air purge, an attempt was made to lower the temperature of the master, without going below 273 K (0°C). This made it possible to create favorable conditions for the generation of chaotic patterns, and the subsequent synchronization of the receiver laser with the transmitter laser. Indeed, this is a basic requirement for attempting secure chaos-based communication.
As in other semiconductor lasers, instances of synchronization and anti-synchronization have been reported; in particular, switching from one type

of synchronization to another occurs by small changes in slave bias current (on the order of fractions of mA). In our case, as in previous studies involving QCL emitting at 5.6 µm [162], anti-synchronization provided better results, both in terms of cross-correlation and auto-correlation, and in terms of reliable communication. For the choice of the data-rate of the message to be sent, however, limitations due to electrical modulation, constituting the main obstacle, were taken into account. These are again due to the choices of physical parameters when designing the superlattice heterostructure. This has prompted us to investigate the different technological possibilities that have been advanced over the years for the production of QCLs, especially as a function of improving their performance, going to work on one or another figure of merit, depending on the application. Relative to chaos generation, still many studies need to be conducted in order to find more definite mathematical and physical relationships with the laser parameters. Certainly a key role is played by the α-factor: theoretically, due to the absence of relaxation oscillations, its value should be 0. In practice, several measurements led to the same result, which is around 1.2. Certainly this value is smaller than that measured for other semiconductor lasers; but the fact that it is non-zero allows us to appreciate chaotic patterns.
Several routes to chaos can be identified, from period-doubling with final coherence collapse as feedback strength increases, to intermittent routes to chaos, leading to the display of LFFs. In each case, as the temperature and bias current of the master change, the alternation of order and chaos can be seen in the output power. The synchronization process, on the other hand, is accomplished by satisfying several requirements; first, master and slave are almost identical, having been taken from the same batch. This allows a matching of electrical and optical parametrics, an essential requirement corresponding to the sharing of so-called private keys between transmitter and receiver in quantum cryptography. Besides that, the optical injection of the master beam into the slave laser cavity leads the slave laser itself to reproduce the behavior of the master. In fact, it reproduces the optical spectrum of the master (because of synchronization); however, the optical spectrum of the master is changed from single narrow linewidth (which means good coherence) to a broader, sometimes multimode, linewidth (and this corresponds to the coherence collapse process) because of the EOF. It must be remembered, however, that the transmitted signal is given by chaos and the hidden message within it; the slave, instead, manages to synchronize with only the chaotic pattern, since the hidden message within it is so small that the variations caused by it are irrelevant in the synchronization process.
Once suitable cross-correlation values (85%-97%) are reached to prove secure communication, the performance of the system is estimated, through the BER and the openness of the eye in the eye diagram. Messages with different data-rate were sent to study the dependence of system performance on transmission rate. The

most promising results were achieved at 1 Mbps, where a difference BER of 0.7% was measured; meantime, the master BER of the same communication attempt was 19%, slightly below the acceptable lower limit of 25% for accomplishing a non-decipherable transmission. In the other cases, i.e., for 5 Mbps and 8 Mbps, the difference BER is higher: 2% and 3.4%, respectively. Certainly the increase in data-rate and the limit imposed on the electrical modulation of the slave at 8 MHz have contributed to worsening the performance of the system. In any case, the difference BER never overcomes the lower limit needed to define the transmission as error-free. It is also impressive how the cross-correlation, as well as the BER and system performance are not worsened when a multipass cell is inserted between the two parties.

Another key aspect concerns not having a definite link between cross-correlation coefficient and BER, as the experimental data clearly report.

Surely this first demonstration of chaos synchronization for secure communication may enable practical applications in the field of secure communication, especially as an alternative to quantum key distribution (QKD), implemented mainly in the visible range, in free-space optical systems. The current challenge is to realize QKD-based ground-to-satellite communication, overcoming the background noise that is detrimental during daytime. Propagation conditions are more favorable during nighttime, but this strongly restrains the availability of the transmission link. This is another reason why other wavelength domains are currently investigated. For instance, NIR light has drawn attention because it is immune to parasitic visible-light perturbation and because optical sources are widely available in this wavelength domain known for telecom applications. Though very appealing because it relies on physically uncrackable photon entanglement, QKD for large-scale communication systems is still hindered by the performances of low-speed, low-yield, expensive transmission apparatus. Furthermore, due to the lack of single-photon detectors, QKD technology is not yet available at mid-infrared wavelength, that is one of the most relevant transmission domains.

Several challenges, however, still need to be addressed; first of all, not taking into account the limitation due to the instruments at our disposal, still the measured chaos bandwidth for these and other QCLs is severely limited. Certainly, we still need to investigate about the parameters influencing that. To be able to increase it, though, one can think of using EOF in conjunction with optical injection, thus going to exploit the chaos of a third laser, whose output beam would be injected inside the master cavity, together with the feedback beam.

Another alternative would correspond to the use of different sources, namely ICLs; these lasers allow emission up to a maximum of 7 µm, so they combine the advantages of the mid-infrared range with those of interband transitions. Indeed, a chaos bandwidth on the order of GHz has been measured, as with other semiconductor lasers; this could have advantages, especially for high-speed applications.

There are other possibilities for an enhancement of the chaos bandwidth and secure information transmission characteristics: the combination of QCL beams integrated in Talbot cavities, including beveled amplifying sections [168], could improve the power and the transmission range [169], [170]. The intended application is a point-to-point link, with an extremely low probability of interception or detection, masked or even undetectable. The Talbot cavity QCL network will enable secure/encrypted physical communications through the combination of several chaotic waveforms with higher power and chaos bandwidth [171]. This inherent aspect of the communication system provides much better protection against laser radiation attacks and electro-optical/IR countermeasure.
Considering the results obtained and analyzing the collected data, some questions still remain open. Definitely, in the immediate future we will focus on a deeper investigation on the parameters of major influence for the generation of QCLs nonlinear dynamics. Likewise, we will deepen the QCLs' chaos features and complexity: Lyapunov exponents, correlation dimension and generation of chaos with additive noise. Indeed, there is no knowledge of the actual weight that noise has in the nonlinear dynamics of QCLs. This series of studies could shed light on new characteristics of lasers under study, paving the way for new discoveries that could lead to more extensive use of these devices, especially in telecommunications. Indeed, it is well known that the market is mainly focusing on the production and sale of QCLs for sensing and spectroscopy, and less for telecommunication applications. The goal will therefore be to enhance these resources by highlighting their strengths, such as low cost and easy implementation, both for high-speed applications and chaos-based secure communication.

Bibliography

[1] ISO Central Secretary. *Optics and photonics — Spectral bands*. en. Standard ISO29110-1:2016. Geneva, CH: International Organization for Standardization, 2007 (cit. on p. 5).

[2] RF Wireless World. *FSO vs Fiber Optic - Difference between FSO and Fiber Optic*. URL: `https://www.rfwireless-world.com/Terminology/Difference-between-FSO-and-Fiber-Optic.html` (visited on 07/19/2022) (cit. on p. 12).

[3] Hemani Kaushal, VK Jain, and Subrat Kar. *Free space optical communication*. Springer, 2017 (cit. on pp. 12, 16).

[4] R Martini and EA Whittaker. «Quantum cascade lasers-based free space optical communications». In: *Optical and FIber Communications Reports* 2 (2005), pp. 1–14 (cit. on pp. 13, 14).

[5] Paul Corrigan, Rainer Martini, Edward A Whittaker, and Clyde Bethea. «Quantum cascade lasers and the Kruse model in free space optical communication». In: *Optics Express* 17.6 (2009), pp. 4355–4359 (cit. on pp. 14, 15).

[6] Chloe Sauvage. «Impact de l'environnement atmosphérique sur les liaisons optiques sans fil pour la ville du futur». PhD thesis. Institut Polytechnique de Paris, 2020 (cit. on p. 14).

[7] R.W. Fenn et al. «Optical and infrared properties of the atmosphere». In: *Chapter 18 of NOAA Handbook*. 1985 (cit. on pp. 14, 15).

[8] Jony J Liu, Barry L Stann, Karl K Klett, Pak S Cho, and Paul M Pellegrino. «Mid and long-wave infrared free-space optical communication». In: *Laser communication and propagation through the atmosphere and oceans VIII*. Vol. 11133. International Society for Optics and Photonics. 2019, p. 1113302 (cit. on pp. 15, 16).

[9] Alexandre Delga and Luc Leviandier. «Free-space optical communications with quantum cascade lasers». In: *Quantum sensing and nano electronics and photonics XVI*. Vol. 10926. International Society for Optics and Photonics. 2019, p. 1092617 (cit. on p. 15).

[10] A Puiu et al. «Lidar/DIAL detection of acetone at 3.3 µm by a tunable OPO laser system». In: *Laser Phys.* 24.085606 (2014) (cit. on p. 16).

[11] Y. P. Tseng, P. Bouzy, C. Pedersen, N. Stone, and P. Tidemand-Lichtenberg. «Upconversion raster scanning microscope for long-wavelength infrared imaging of breast cancer microcalcifications». In: *Biomed. Opt. Express* 9.10 (2018), pp. 4979–4987 (cit. on p. 17).

[12] R.J. Grasso. «Defence and security applications of quantum cascade lasers». In: *Optical sensing, imaging, and photon counting: nanostructured devices and applications 2016* 9933 (2016) (cit. on pp. 17, 18).

[13] RP Photonics. *Mid-infrared Laser Sources*. URL: `https://www.rp-photonics.com/mid_infrared_laser_sources.html` (visited on 07/20/2022) (cit. on p. 18).

[14] NASA. *NASA Reveals Webb Telescope's First Images of Unseen Universe*. URL: `https://www.nasa.gov/press-release/nasa-reveals-webb-telescope-s-first-images-of-unseen-universe` (visited on 07/21/2022) (cit. on p. 18).

[15] C.W. Rudy. *Mid-IR lasers: power and pulse capability ramp up for mid-IR lasers*. 2014. (Visited on 07/21/2022) (cit. on p. 19).

[16] R.Q. Yang. «Infrared laser based on interband transitions in quantum wells». In: *Superlattices and Microstructures* 17.17 (1995), pp. 77–83 (cit. on p. 20).

[17] C.H. Lin et al. «Type-II interband quantum cascade laser at 3.8 µm». In: *Electronics Letters* 33.7 (1997), pp. 598–599 (cit. on p. 20).

[18] A. Spott et al. «Interband cascade laser on silicon». In: *Optica* 5.8 (2008), pp. 996–1005 (cit. on p. 20).

[19] A. Spott et al. «Quantum cascade lasers on Silicon». In: *Optica* 3.5 (2016), pp. 545–551 (cit. on pp. 20, 41, 43, 44).

[20] N. Picqué and T.W. Hänsch. «Mid-IR spectroscopic sensing». In: *Optics and Photonics News* (2019) (cit. on p. 20).

[21] J. Schneide et al. «Characterization of a Ho3+-doped fluoride fiber laser with a 3.9-µm emission wavelength». In: *Appl. Opt.* 36.33 (1997) (cit. on p. 21).

[22] S.D. Jackson. «Single-transverse-mode 2.5-W holmium-doped fluoride fiber laser operating at 2.86 µm». In: *Opt. Lett.* 29.4 (2004), p. 334 (cit. on p. 21).

[23] J. Li et al. «High-power diode-pumped fiber laser operating at 3 µm». In: *Opt. Lett.* 36.18 (2018), p. 761 (cit. on p. 21).

[24] V. Fortin et al. «10-W-level monolithic dysprosium-doped fiber laser at 3.24 µm». In: *Opt. Lett.* 44.3 (2019), p. 491 (cit. on p. 21).

[25] F. Maes et al. «Room-temperature fiber laser at 3.92 µm». In: *Optica* 5.7 (2018), p. 761 (cit. on p. 21).

[26] Jerome Faist, Federico Capasso, Deborah L Sivco, Carlo Sirtori, Albert L Hutchinson, and Alfred Y Cho. «Quantum cascade laser». In: *Science* 264.5158 (1994), pp. 553–556 (cit. on pp. 22, 41).

[27] Jerome Faist et al. «High-power continuous-wave quantum cascade lasers». In: *IEEE Journal of Quantum Electronics* 34.2 (1998), pp. 336–343 (cit. on p. 24).

[28] C. Mann et al. «Continuous-wave operation of 5 µm quantum cascade lasers with high-reflection coated facets». In: *Electronics Letters* 39.22 (2003) (cit. on p. 24).

[29] T. Gensty and W. Elsäßer. «Semiclassical model for relative intensity noise of intersubband quantum cascade lasers». In: *Optics Communications* 256 (2005), pp. 171–183 (cit. on p. 26).

[30] J. Faist. *Quantum Cascade Lasers*. Oxford University Press, 2013 (cit. on p. 26).

[31] B.S. Williams. «Terahertz quantum cascade lasers». PhD thesis. Massachusetts Institute of Technology, 2003 (cit. on p. 28).

[32] Y. Yao et al. «Mid-infrared quantum cascade lasers». In: *Nature Photonics* 6 (2012), pp. 432–439 (cit. on p. 28).

[33] F. Toor et al. «Effect of waveguide sidewall roughness on the threshold current density and slope efficiency of quantum cascade lasers». In: *Applied Physics Letters* 93.3 (2008), p. 031104 (cit. on p. 29).

[34] C.H. Henry. «Theory of the linewidth of semiconductor lasers». In: *IEEE Journal of Quantum Electronics* 18.259 (1982) (cit. on p. 30).

[35] Jens Staden, Tobias Gensty, Wolfgang Elsässer, Guido Giuliani, and Christian Mann. «Measurements of the alpha factor of a distributed-feedback quantum cascade laser by an optical feedback self-mixing technique». In: *Optics letters* 31 (Oct. 2006), pp. 2574–6 (cit. on p. 30).

[36] Louise Jumpertz, Florian Michel, Robert Pawlus, Wolfgang Elsässer, Mathieu Carras, Kevin Schires, and Frédéric Grillot. «Linewidth broadening factor and gain compression in quantum cascade lasers». In: Feb. 2016, 97550F (cit. on p. 30).

[37] Olivier Spitz and Frédéric Grillot. «A review of recent results of mid-infrared quantum cascade photonic devices operating under external optical control». In: *J. Phys. Photonics* 4 (2022), p. 022001 (cit. on pp. 31, 97).

[38] R. Paiella. *Intersubband Transitions in Quantum Structures*. McGraw-hill, 2006 (cit. on pp. 31, 32, 38, 40).

[39] L.A. Coldren and S.W. Corzine. *Diode Lasers and Photonic Integrated Circuits*. Wiley New York, 1995 (cit. on p. 32).

[40] A. Yariv. *Quantum Electronics, 3rd ed.* Wiley New York, 1989 (cit. on p. 33).

[41] N. Mustafa et al. «Terahertz bandwidth prediction for amplitude modulation response of unipolar intersubband semiconductor lasers». In: *IEEE Photonics Technology Letters* 11.5 (1999), pp. 527–529 (cit. on p. 33).

[42] F. Rana and Ram; R.J. In: *Physics Reviews* B65 (2002) (cit. on p. 33).

[43] E. Luzhansky. «Quantum cascade lasers modulation and applications». PhD thesis. University of Maryland, 2015 (cit. on pp. 33, 47).

[44] Farhan Rana and Rajeev J. Ram. «Current noise and photon noise in quantum cascade lasers». In: *Phys. Rev. B* 65 (12 Mar. 2002), p. 125313 (cit. on p. 33).

[45] Yoann Petitjean, Fabien Destic, Jean-Claude Mollier, and Carlo Sirtori. «Dynamic Modeling of Terahertz Quantum Cascade Lasers». In: *IEEE Journal of Selected Topics in Quantum Electronics* 17.1 (2011), pp. 22–29 (cit. on p. 33).

[46] M.J. Süess et al. «Advanced Fabrication of Single-Mode and Multi-Wavelength MIR-QCLs». In: *Photonics* 3.26 (2016), pp. 336–343 (cit. on p. 34).

[47] A. Lyakh et al. «3 W continuous-wave room temperature single-facet emission from quantum cascade lasers based on nonresonant extraction design approach». In: *Appl. Phys. Lett.* 95 (2009), p. 141113 (cit. on p. 35).

[48] Yohei Matsuoka, Mykhaylo Semtsiv, and W. Masselink. *Quantum cascade lasers*. 2020 (cit. on pp. 35, 36).

[49] Gmachl; C., F. Capasso, D.L. Sivco, and A. Y. Cho. «Recent progress in quantum cascade lasers and applications». In: *Report on Progress in Physics* 64 (2001), pp. 1533–1601 (cit. on pp. 37, 38, 41, 46).

[50] J. Faist et al. «Distributed feedback quantum cascade lasers». In: *Applied Physics Letters* 70 (1997), pp. 2670–2672 (cit. on p. 37).

[51] C. Gmatchl et al. «Complex-coupled quantum cascade distributed-feedback laser». In: *IEEE Photon. Tech. Lett.* 9 (1997), pp. 1090–1092 (cit. on p. 37).

[52] Y. Yao, A.J. Hoffman, and C.F Gmachl. «Mid-infrared quantum cascade lasers». In: *Nature Photonics* 6 (2012) (cit. on pp. 37, 38, 41).

[53] S. Blaser et al. «Room-temperature, continuous-wave, single-mode quantum cascade laser at $\lambda \approx 5.4$µm». In: *Applied Physics Letters* 86 (2005), p. 041109 (cit. on p. 37).

[54] M. Carras and A. De Rossi. «Photonic modes of metallodielectric periodic waveguides in the midinfrared spectral range». In: *Physics Review B* 74 (2006), p. 235120 (cit. on p. 37).

[55] A. Spott, N. Volet, J.D. Peters, and J.R. Meyer. «Heterogeneous Integration for Mid-Infrared Silicon Photonics». In: *IEEE J. Select. Topics Quantum Electronics* (2017) (cit. on pp. 41, 44, 45).

[56] A.N. Baranov and R. Teisser. «Quantum cascade lasers in the InAs/ALSb material system». In: *IEEE Journal of Selected Topics in Quantum Electronics* 21.6 (2015) (cit. on pp. 42, 43).

[57] C Sirtori, P Kruck, S Barbieri, Ph Collot, J. Nagle, Mattias Beck, Jérôme Faist, and Ursula Oesterle. «GaAs/AlxGa1-xAs quantum cascade lasers». In: *Applied Physics Letters* 73 (Dec. 1998), pp. 3486–3488 (cit. on p. 42).

[58] Rüdeger Köhler, Alessandro Tredicucci, Fabio Beltram, Harvey E. Beere, Edmund H. Linfield, A. Giles Davies, David A. Ritchie, Rita C. Iotti, and Fausto Rossi. «Terahertz semiconductor-heterostructure lasers». In: *Conference on Lasers and Electro-Optics*. Optica Publishing Group, 2002, CPDC12 (cit. on p. 42).

[59] C. Walther, G. Scalari, J. Faist, H. Beere, and D. Ritchie. «Low frequency terahertz quantum cascade laser operating from 1.6 to 1.8THz». In: *Applied Physics Letters* 89.23 (2006) (cit. on p. 42).

[60] O. Cathabard, R. Teissier, J. Devenson, J. Moreno, and A. Baranov. «Quantum cascade lasers emitting near 2.6 µm». In: *Applied Physics Letters* 96 (2010) (cit. on p. 42).

[61] C. Becker et al. «AlAs/GaAs quantum cascade lasers based on large conduction band discontinuity». In: *Applied Physics Letters* 77 (2000), pp. 463–465 (cit. on p. 42).

[62] Carlo Sirtori, Jérôme Faist, Federico Capasso, Deborah L. Sivco, Albert L. Hutchinson, and Alfred Yi Summit Cho. «Quantum cascade laser with plasmon-enhanced waveguide operating at 8.4 μm wavelength». In: *Applied Physics Letters* 66 (1995), pp. 3242–3244 (cit. on p. 43).

[63] C Sirtori, P Kruck, S Barbieri, H Page, J. Nagle, Mattias Beck, Jérôme Faist, and Ursula Oesterle. «Low-loss Al-free waveguides for unipolar semiconductor lasers». In: *Applied Physics Letters* 75 (Dec. 1999), pp. 3911–3913 (cit. on p. 43).

[64] B.J. Eggleton, B. Luther-Davies, and K. Richardson. «Chalcogenide photonics». In: *Nature Photonics* (2011) (cit. on p. 43).

[65] A.W.L. Fang, H. Park, O. Cohen, R. Jones, J. Paniccia, and J.E. Bowers. «Electrically pumped hybrid AlGaInAs-silicon evanescent laser». In: *Opt. Express* 14.20 (2006), pp. 9203–9210 (cit. on p. 43).

[66] C. Zhang, S. Zhang, J.D. Peters, and J.E. Bowers. «8x8x40 Gbps fully integrated silicon photonic network on chip». In: *Optica* 3.7 (2016), pp. 785–786 (cit. on p. 43).

[67] M. Muneeb et al. «III-V -on-silicon integrated micro-spectrometer for the 3 µm wavelength range». In: *Opt. Express* 24.9 (2016), pp. 9465–9472 (cit. on p. 43).

[68] M. Nedeljkovic et al. «Mid-Infrared Silicon-on-Insulator Fourier Transform Spectrometer Chip». In: *IEEE Photon. Technol. Lett.* 28.4 (2016), pp. 528–531 (cit. on p. 43).

[69] R. Wang, S. Sprengel, et al. «2 µm wavelength range InP-based type-II quantum well photodiodes heterogeneously integrated on silicon phonic integrated circuits». In: *Opt. Express* 23.20 (2015), pp. 26834–26841 (cit. on p. 43).

[70] N. Volet, E.J. Spott A. Stanton, M.L. Davenport, L. Chang, J.D. Peters, T.C. Briles, I. Vurgaftman, J.R. Meyer, and J.E. Bowers. «Semiconductor optical amplifiers at 2.0-µm on silicon». In: *Lasers & Photonics Reviews* 11.2 (2017), p. 1600165 (cit. on p. 44).

[71] T. Komljenovic et al. «Widely Tunable Narrow-linewidth Monolithically Integrated External-Cavity Semiconductor Lasers». In: *IEEE J. Select. Topics Quantum Electronics* 21.6 (2015), p. 1501909 (cit. on p. 44).

[72] Rainer Martini et al. «High-speed modulation and free-space optical audio/video transmission using quantum cascade lasers». In: *Electronics Letters* 37.3 (2001), pp. 191–193 (cit. on p. 45).

[73] Rainer Martini et al. «Free-space optical transmission of multimedia satellite data streams using mid-infrared quantum cascade lasers». In: *IEEE Electronics Letters* 38.4 (2002), pp. 181–183 (cit. on p. 45).

[74] S. Blaser et al. «Free-space optical data link using peltier-cooled quantum cascade lasers». In: *IEEE Electronics Letters* 37.12 (2001), pp. 778–780 (cit. on p. 46).

[75] B. Hinkov et al. «Rf-modulation of mid-infrared distributed feedback quantum cascade lasers». In: *Optics Express* 24.4 (2016), pp. 778–780 (cit. on p. 46).

[76] R. Measures. *Laser Remote Chemical Analysis*. John Wiley & Sons, NY, 1988 (cit. on p. 46).

[77] F. Capasso. «High-performance midinfrared quantum cascade lasers». In: *Opt. Eng.* 49.11 (2010), p. 111102 (cit. on p. 46).

[78] M.S. Vitiello, G. Scalari, B. Williams, and D.N. Paolo. «Quantum cascade lasers: 20 years of challenges». In: *Optics Express* 23.4 (2015), pp. 5167–5182 (cit. on p. 46).

[79] S. Piazzolla. «Atmospheric Channel». In: *Near-Earth Laser Communications*. CRC Press. 2009 (cit. on p. 47).

[80] Edward N. Lorenz. *The essence of chaos*. UCL Press, 1993 (cit. on pp. 48, 121).

[81] James Gleick. *Chaos: making a new science*. Viking Books, 1987 (cit. on pp. 48, 50).

[82] Dschwen: Wikimedia Commons. *File:Lorenz attractor.svg*. URL: `https://commons.wikimedia.org/wiki/File:Lorenz_attractor.svg` (visited on 08/20/2022) (cit. on p. 49).

[83] E.N. Lorenz. «Deterministic nonperiodic flow». In: *J Atmos Sci* 20 (1963), pp. 130–148 (cit. on p. 49).

[84] Robert May. «Simple Mathematical Models With Very Complicated Dynamics». In: *Nature* 26 (1976) (cit. on p. 51).

[85] P. Bergé, Y. Pomeau, and C. Vidal. *Order in Chaos: towards a deterministic approach to turbulence*. John Wiley & Sons, 1986 (cit. on p. 52).

[86] B. Mandelbrot. *Fractals*. Freeman, 1977 (cit. on p. 52).

[87] J.C. Sprott. «Maximally complex simple attractor». In: *Chaos* 17.121 (2007) (cit. on p. 53).

[88] A. Wolf. «Quantifying chaos with Lyapunov exponents». In: *Chaos* 16 (1986), pp. 285–317 (cit. on p. 53).

[89] A. Wolf et al. «Determining Lyapunov exponents from a time series». In: *Physics D: Nonlinear Phenomena* 16.3 (1985), pp. 285–317 (cit. on p. 53).

[90] J.C. Sprott. *Chaos and Time-Series Analysis*. Oxford University Press, 2003 (cit. on p. 53).

[91] J.L. Kaplan and J.A. Yorke. «Chaotic behavior of multidimensional difference equations». In: *Functional differential equations and approximation of fixed points*. Springer, 1979, pp. 204–227 (cit. on p. 53).

[92] P. Grassberger and I. Procaccia. «Estimation of the Kolmogorov entropy from a chaotic signal». In: *Physical Review A* 28.4 (1983), p. 2591 (cit. on p. 53).

[93] Y.B. Persin. «Characteristic Lyapunov exponents and smooth ergodic theory». In: *Uspekhi Matematicheskikh Nauk* 32.4 (1977), pp. 55–112 (cit. on p. 53).

[94] P. Ketthong and B. Srisuchinwong. «A damping-tunable SNap System: from dissipative hyperchaos to conservative chaos». In: *Entropy* 24.121 (2022) (cit. on p. 53).

[95] J.C. Sprott. *Elegant Chaos: Algebraically simple chaotic flows*. World Scientific: Singapore, 2010 (cit. on p. 54).

[96] H. Haken. «Analogy between higher instabilities in fluids and lasers». In: *Phys Lett* 53A (1975), pp. 77–78 (cit. on p. 54).

[97] L.W. Casperson. «Spontaneous coherent pulsations in laser oscillators». In: *IEEE J Quantum Electron* 14 (1978), pp. 756–761 (cit. on pp. 54, 55).

[98] C.O. Weiss et al. «Oscillation period doubling chaos in a laser». In: *Opt Commun* 44 (1982), pp. 59–61 (cit. on pp. 54, 55).

[99] C.O. Weiss et al. «Instabilities and chaos of a single mode NH_3 ring laser». In: *Opt Commun* 44 (1985), pp. 405–408 (cit. on pp. 54, 55).

[100] R. Lang and K. Kobayashi. «External optical feedback effects on semiconductor injection properties». In: *IEEE J Quantum Electron* 16 (1980), pp. 347–355 (cit. on pp. 54, 57, 63, 64).

[101] Y. Hori et al. «Chaos in directly modulated semiconductor lasers». In: *J Opt Soc Am B* 5 (1988), pp. 1128–1133 (cit. on p. 55).

[102] F.T. Arecchi, G.L. Lippi, and J.R. Tredicce. «Deterministic chaos in laser with injected signal». In: *Optic Communications* 51 (1984), pp. 308–314 (cit. on p. 55).

[103] H. Haken. *Light*. Vol. 2. North-Holland, Amsterdam, 1985 (cit. on p. 55).

[104] D. Dangoisse et al. «Chaos in a CO_2 laser with modulated parameters: experiments and numerical simulations». In: *Phys Rew A* 36.10 (1987), p. 4775 (cit. on p. 55).

[105] Roberto Paiella et al. «High-frequency modulation without the relaxation oscillation resonance in quantum cascade lasers». In: *Applied Physics Letters* 79.16 (2001), pp. 2526–2528 (cit. on pp. 55, 56).

[106] F. Grillot. «On the effects of an antireflection coating impairment on the sensitivity to optical feedback of AR/HR semiconductor DFB lasers». In: *IEEE Journal of Quantum Electronics* 45.6 (2009), pp. 720–729 (cit. on p. 57).

[107] H. Olesen, J.H. Osmundsen, and B. Tromborg. «Nonlinear dynamics and spectral behavior for an external cavity laser». In: *IEEE Journal of Quantum Electronics* 22.6 (1986), pp. 762–773 (cit. on p. 58).

[108] Frédéric Grillot, Bruno Thedrez, J. Py, O. Gauthier-Lafaye, V. Voiriot, and J.L. Lafragette. «2.5-Gb/s transmission characteristics of 1.3-μm DFB lasers with external optical feedback». In: *Photonics Technology Letters, IEEE* 14 (Feb. 2002), pp. 101–103 (cit. on p. 58).

[109] J. Mork, M. Semkow, and B. Tromborg. «Measurement and theory of mode hopping in external cavities laser». In: *Electronics Letters* 26.9 (1990), pp. 609–610 (cit. on p. 58).

[110] S.P. Hegarty et al. «Analysis of the fast recovery dynamics of a semiconductor laser with feedback in the low-frequency fluctuation regime». In: *Optics Letters* 23.15 (1998), pp. 1206–1208 (cit. on p. 59).

[111] J. Ohtsubo. *Semiconductor lasers: stability, instability and chaos.* Springer, 2013 (cit. on pp. 59, 60).

[112] R. Tkach and A. Chraplyvy. «Regimes of feedback effects in 1.5-μm distributed feedback lasers». In: *Journal of Lightwave technology* 4.11 (1986), pp. 1655–1661 (cit. on pp. 59–61, 63).

[113] T. Heil et al. «Coexistence of low-frequency fluctuations and stable emission on a single high-gain mode in semiconductor lasers with external optical feedback». In: *Physical Review A* 58.4 (1998), R2672 (cit. on pp. 60, 61).

[114] D.M. Kane and K.A. Shore. *Unlocking dynamical diversity.* John Wiley & Sons, 2005 (cit. on p. 60).

[115] F. Grillot, G. H. Duan, and B. Thedrez. «Feedback sensitivity and coherence collapse threshold of semiconductor DFB lasers with complex structures». In: *IEEE Journal of Quantum Electronics* 40.3 (2004), pp. 1–11 (cit. on p. 61).

[116] F. Grillot. «On the Effects of an Antireflection Coating Impairment on the Sensitivity to Optical Feedback of AR/HR Semiconductor DFB Lasers». In: *IEEE Journal of Quantum Electronics* 45 (2009), p. 6 (cit. on p. 61).

[117] J. Mork, J. Mark, and B. Tromborg. «Route to chaos and competition between relaxation oscillations for a semiconductor laser with optical feedback». In: *Physical Review Letters* 65.16 (1990), p. 1999 (cit. on p. 61).

[118] L. Jumpertz, M. Carras, K. Schires, and F. Grillot. «Regimes of external optical feedback in 5.6-μm distributed feedback mid-infrared quantum cascade lasers». In: *Applied Physics Letters* 105 (2014), p. 131112 (cit. on pp. 62, 63, 101).

[119] F. Mezzapesa et al. «Intrinsic stability of quantum cascade lasers against optical feedback». In: *Optics Express* 21.11 (2013), pp. 13748–13757 (cit. on p. 62).

[120] H. Kakiuchida and J. Ohtsubo. «Characteristics of a semiconductor laser with external feedback». In: *IEEE Journal of Quantum Electronics* 30 (1994), pp. 2087–2097 (cit. on p. 63).

[121] O. Spitz. «Mid-infrared quantum cascade lasers for chaos secure communication». PhD thesis. Télécom Paris, 2019 (cit. on pp. 64, 65, 67, 98, 103).

[122] J. Mork and B. Tromborg. «The mechanism of mode selection for an external cavity laser». In: *IEEE Photonics Technology Letters* 2 (1990), pp. 21–23 (cit. on p. 64).

[123] Louise Jumpertz, Kevin Schires, Mathieu Carras, Marc Sciamanna, and Frédéric Grillot. «Chaotic Light at Mid-Infrared Wavelength». In: *Light: Science & Applications* 5 (Jan. 2016) (cit. on pp. 64, 66).

[124] C. Shannon. «Communication theory of secrecy systems». In: *Bell System Technical Journal* 28.4 (1949), pp. 656–715 (cit. on p. 68).

[125] M.A. Nielsen and I.L. Chuang. *Quantum Computation and Quantum Information.* Cambridge University Press, 2000 (cit. on p. 68).

[126] A. Holevo. *Quantum Systems, Channels, Information: A Mathematical Introduction.* Vol. 16. De Gruyter, 2012 (cit. on p. 68).

[127] M. Hayashi. *Quantum Information Theory: Mathemztical Foundation.* Springer-Verlag, 2017 (cit. on p. 68).

[128] D. Bernstein. «Introduction to post-quantum cryptography». In: *Post-Quantum Cryptography.* Berlin, Heidelberg: Springer, 2009 (cit. on p. 68).

[129] N. Gisin, G. Ribordy, W. Tittel, and H. Zbinden. «Quantum cryptography». In: *Reviews of Modern Physics* 74.1 (2002), pp. 145–195 (cit. on p. 68).

[130] C.H. Bennett and G. Brassard. «Quantum cryptography: Public key distribution and coin tossing». In: *Theoretical Computer Science* 560 (2014), pp. 7–11 (cit. on p. 68).

[131] W. Wootters and W. Zurek. «A single quantum cannot be cloned». In: *Nature* 299.802 (1982) (cit. on p. 68).

[132] QuantumXChange. *A brief guide to Quantum Encryption vs Post-Quantum Cryptography.* URL: a (visited on 07/22/2022) (cit. on p. 69).

[133] S. Banarjee and J. Kurths. «Chaos and cryptography: a new dimension in secure communications». In: *The European Physical Journal* 223 (2014), pp. 1441–1445 (cit. on p. 69).

[134] J.S. Teh et al. «Implementation and practical problems of chaos-based cryptography revised». In: *Journal of Information Security and Applications* (2019) (cit. on p. 70).

[135] A. Pikovsky, M. Rosenblum, and J. Kurths. *Synchronization: A Universal Concept in Nonlinear Sciences*. Cambridge University Press, 2001 (cit. on p. 70).

[136] Atsushi Uchida. *Optical Communication with Chaotic Lasers: Applications of Nonlinear Dynamics and Synchronization*. 2012 (cit. on pp. 71, 73, 80, 81).

[137] Jiagui Wu et al. «Physically secure image transfer using synchronized chaos between silicon optomechanical cavities». In: *Conference on Lasers and Electro-Optics*. Optica Publishing Group, 2020, STh4O.7 (cit. on p. 73).

[138] H.M. Oliveira and L.V. Melo. «Huygens synchronization of two clocks». In: *Scientific Reports* 5 (2015), p. 11548 (cit. on pp. 74, 106).

[139] L.M. Pecora and T.L. Carroll. «Synchronization in Chaotic Systems». In: *Physical Review Letters* 64.8 (1990) (cit. on pp. 74, 75).

[140] H.G. Winful and L. Rahman. «Synchronized chaos and spatiotemporal chaos in arrays of coupled lasers». In: *Physical Review Letters* 65.13 (1990), p. 1575 (cit. on p. 74).

[141] R. Roy and K.S.Jr. Thornburg. «Experimental synchronization of chaotic lasers». In: *Physical Review Letters* 72.13 (1994), p. 2009 (cit. on p. 74).

[142] T. Sugawara et al. «Observation of synchronization in laser chaos». In: *Physical Review Letters* 72.22 (1994), p. 3502 (cit. on p. 74).

[143] Y. Liu et al. «Chaotic and periodic passive Q-switching in coupled CO_2 lasers with a saturable absorber». In: *Physical Review A* 50.4 (1994), p. 3464 (cit. on p. 74).

[144] H.A. Haus and A. Mecozzi. «Noise of mode-locked lasers». In: *IEEE Journal of Quantum Electronics* 29.3 (1993), pp. 993–996 (cit. on pp. 75, 100).

[145] M. Ozaki et al. «Leader-laggard relationship of chaos synchronization in mutually coupled vertical-cavity surface-emitting lasers with time delay». In: *Physical Review E* 79.2 (2009) (cit. on p. 75).

[146] Olivier Spitz, Andreas Herdt, Jiagui Wu, Grégory Maisons, Mathieu Carras, Chee-Wei Wong, Wolfgang Elsäßer, and Frédéric Grillot. «Private communication with quantum cascade laser photonic chaos». In: *Nature communications* 12.1 (2021), pp. 1–8 (cit. on pp. 75, 76, 85).

[147] I. Wedekind and U. Parlitz. «Experimental observation of synchronization and anti-synchronization of chaotic low-frequency-fluctuations in external cavity semiconductor lasers». In: *International Journal of Bifurcation and Chaos* 11.4 (2001), pp. 1141–1147 (cit. on pp. 75, 76).

[148] K.M. Cuomo and A.V. Oppenheim. «Circuit implementation of synchronized chaos with applications to communications». In: *Physical Review Letters* 71.1 (1993), p. 65 (cit. on pp. 77, 83).

[149] I. Fischer, Y. Liu, and P. Davis. «Synchronization of chaotic semiconductor laser dynamics on subnanosecond time scales and its potential for chaos communication». In: *Physical Review* 62 (2000) (cit. on pp. 77, 96).

[150] T. Heil et al. «ON/OFF shift keying for chaos-encrypted communication using external-cavity semiconductor lasers». In: *IEEE Journal of quantum electronics* 38.7 (2002), pp. 1162–1170 (cit. on p. 82).

[151] J.M. Liu, H.F. Chen, and S. Tang. «Synchronized chaotic optical communications at high bit rates». In: *IEEE Journal of Quantum Electronics* 38.9 (2002), pp. 1184–1196 (cit. on pp. 82, 83).

[152] P. Colet and R. Roy. «Digital communication with synchronized chaotic lasers». In: *Optics Letters* 19.24 (1994), pp. 2056–2058 (cit. on p. 83).

[153] V. Annovazzi-Lodi et al. «Synchronization of chaotic injected-laser systems and its application to optical cryptography». In: *IEEE Journals of Quantum Electronics* 32.6 (1996), pp. 953–959 (cit. on p. 83).

[154] C.R. Mirasso et al. «Synchronization of chaotic semiconductor lasers: Application to encoded communications». In: *IEEE Photonics Technology Letters* 8.2 (1998), pp. 299–301 (cit. on p. 83).

[155] A. Argyris et al. «Chaos-based communications at high bit rates using commercial fibre-optic links». In: *Nature* 438.7066 (2005), p. 343 (cit. on p. 84).

[156] V. Annovazzi-Lodi et al. «Optical chaos masking of video signals». In: *IEEE Photonics Technology Letters* 17.9 (2005), pp. 1995–1997 (cit. on pp. 84, 85).

[157] H. Erzgraber, B. Lenstra D. andKrauskopf, E. Wille, M. Peil, I. Fischer, and W. Elsa¨ßer. «Mutually delay-coupled semiconductor lasers: Mode bifurcation scenarios». In: *Opt Commun* 205 (2005), pp. 286–296 (cit. on p. 89).

[158] M. K. Haldar. «A simplified analysis of direct intensity modulation of quantum cascade lasers». In: *IEEE Journal of Quantum Electronics* 41.11 (2005), pp. 1349–1355 (cit. on p. 94).

[159] H. Dely et al. «10 Gbit s-1 Free Space Data Transmission at 9 µm Wavelength With Unipolar Quantum Optoelectronics». In: *Laser & Photonics Reviews* 16 (2022), p. 2100414 (cit. on pp. 94, 96).

[160] Olivier Spitz, Jiagui Wu, Mathieu Carras, Chee-Wei Wong, and Frédéric Grillot. «Low-frequency fluctuations of a mid-infrared quantum cascade laser operating at cryogenic temperatures». In: *Laser Phys. Lett.* 15.11 (2018), p. 116201 (cit. on p. 97).

[161] H. Someya et al. «Synchronization of bandwidth-enhanced chaos in semiconductor lasers with optical feedback and injection». In: *Optics Express* 17.22 (2009), p. 19536 (cit. on p. 99).

[162] Olivier Spitz, Andreas Herdt, Grégory Maisons, Mathiew Carras, Chee-Wei Wong, Wolfgang Elsäßer, and Frédéric Grillot. «Private Communication with quantum cascade laser photonic chaos». In: *Nature Communications* (2021) (cit. on pp. 101, 102, 122).

[163] M.H. Mahdieh and M. Pournoury. «Atmospheric turbulence and numerical evaluation of bit error rate (BER) in free-space communication». In: *Optics & Lasers Technology* 42 (2010), pp. 55–60 (cit. on p. 112).

[164] L.-L. Cao et al. «BER Performance of Free-space Optical Communication in Strong Turbulence with Pointing Errors». In: *International Conference on Wireless Communications and Signal Processing (WCSP)*. Vol. 42. 2012, pp. 1–5 (cit. on p. 112).

[165] R.K. Tyson, D.E. Canning, and J.S. Tharp. «Measurement of the bit-error rate of an adaptive optics, free-space laser communications system, part 1: tip-tilt configuration, diagnostics, and closed-loop results». In: *Optical Engineering* 44.9 (2005), p. 096002 (cit. on p. 112).

[166] Adonis Bogris, Apostolos Argyris, and Dimitris Syvridis. «Encryption Efficiency Analysis of Chaotic Communication Systems Based on Photonic Integrated Chaotic Circuits». In: *IEEE Journal of Quantum Electronics* 46.10 (2010), pp. 1421–1429 (cit. on p. 114).

[167] Xiaodan Pang et al. «Free-Space Communications Enabled by Quantum Cascade Lasers». In: *physica status solidi (a)* 218 (Aug. 2020). DOI: `10.1002/pssa.202000407` (cit. on p. 121).

[168] Mykhaylo Semtsiv and William Masselink. «Fundamental mode emission in tapered quantum cascade lasers for high brightness». In: Oct. 2019, p. 4. DOI: `10.1117/12.2535394` (cit. on p. 124).

[169] A. Gavrielides and T. C. Newell. «Global coupling of QCLs: inclusion of dynamics». In: *Opt. Express* 28.6 (Mar. 2020), pp. 7746–7758. DOI: 10.1364/OE.28.007746. URL: http://opg.optica.org/oe/abstract.cfm?URI=oe-28-6-7746 (cit. on p. 124).

[170] Bo Meng, Bo Qiang, Etienne Rodriguez, Xiao Nan Hu, Guozhen Liang, and Qi Jie Wang. «Coherent emission from integrated Talbot-cavity quantum cascade lasers». In: *Opt. Express* 25.4 (Feb. 2017), pp. 3077–3082. URL: http://opg.optica.org/oe/abstract.cfm?URI=oe-25-4-3077 (cit. on p. 124).

[171] Frédéric Grillot, Athanasios Gavrielides, Olivier Spitz, Tim Newell, and Mathieu Carras. «Talbot coupling of an array of quantum cascade lasers». In: (Feb. 2018) (cit. on p. 124).